

Data-based Dynamic Condition Assessment of Railway Catenaries

Wang, Hongrui

DOI

[10.4233/uuid:3c0e4277-1aff-48ad-b72b-6926d2c876c2](https://doi.org/10.4233/uuid:3c0e4277-1aff-48ad-b72b-6926d2c876c2)

Publication date

2019

Document Version

Final published version

Citation (APA)

Wang, H. (2019). *Data-based Dynamic Condition Assessment of Railway Catenaries*. [Dissertation (TU Delft), Delft University of Technology]. <https://doi.org/10.4233/uuid:3c0e4277-1aff-48ad-b72b-6926d2c876c2>

Important note

To cite this publication, please use the final published version (if applicable).
Please check the document version above.

Copyright

Other than for strictly personal use, it is not permitted to download, forward or distribute the text or part of it, without the consent of the author(s) and/or copyright holder(s), unless the work is under an open content license such as Creative Commons.

Takedown policy

Please contact us and provide details if you believe this document breaches copyrights.
We will remove access to the work immediately and investigate your claim.

Data-based Dynamic Condition Assessment of Railway Catenaries

Data-based Dynamic Condition Assessment of Railway Catenaries

Proefschrift

ter verkrijging van de graad van doctor
aan de Technische Universiteit Delft,
op gezag van de Rector Magnificus prof. ir. T.H.J.J. van der Hagen,
voorzitter van het College voor Promoties,
in het openbaar te verdedigen op woensdag 4 december 2019 om 12:30 uur

door

Hongrui WANG

Bachelor of Science in Electrical Engineering,
Southwest Jiaotong University, Chengdu, China,
geboren te Ya'an, China.

Dit proefschrift is goedgekeurd door de

Promotor: Prof. dr. ir. R.P.B.J. Dollevoet

Copromotor: Dr. ir. A.A. Núñez Vicencio

Samenstelling promotiecommissie:

Rector Magnificus,	voorzitter
Prof. dr. ir. R.P.B.J. Dollevoet,	Technische Universiteit Delft
Dr. ir. A.A. Núñez Vicencio,	Technische Universiteit Delft

Onafhankelijke leden:

Prof. dr. R.M.P. Goverde,	Technische Universiteit Delft
Prof. dr. ir. Z. Li,	Technische Universiteit Delft
Prof. dr. ir. L.A.M. van Dongen,	University of Twente
Prof. dr. E. Chatzi,	ETH Zürich
Prof. dr. A. Rønnequist,	Norwegian University of Science and Technology



Keywords: railway catenary, condition assessment, pantograph-catenary interaction, performance indicator, adaptive data processing, data-driven approach, catenary structure wavelength

Printed by: Gildeprint

Front & Back: Gildeprint

Copyright © 2019 by Hongrui Wang

All rights reserved. No part of the material protected by this copyright notice may be reproduced or utilized in any form or by any means, electronic or mechanical, including photocopying, recording or by any information storage and retrieval system, without written permission from the author.

ISBN 978-94-6323-962-2

An electronic version of this dissertation is available at

<http://repository.tudelft.nl/>.

To my beloved wife and parents
致我挚爱的妻子和父母

Contents

Summary	xi
Samenvatting	xiii
1 Introduction	1
1.1 Background	2
1.2 Challenges for the condition monitoring of railway catenary	4
1.2.1 From data to assessment	4
1.2.2 From assessing the present to the future	5
1.2.3 From manual data processing to adaptive approaches	6
1.3 Research objectives and questions	7
1.4 Dissertation contributions	8
1.4.1 Scientific contribution	8
1.4.2 Societal contribution	9
1.5 Dissertation outline	9
References	12
2 Detecting irregularities using contact force	15
2.1 Introduction	16
2.2 The concept of CSW	18
2.3 EEMD-based CSW extraction	21
2.3.1 EMD algorithm	21
2.3.2 EEMD algorithm	23
2.3.3 EEMD-based extraction approach	24
2.4 Validation and potential applications	28
2.4.1 The CSWs	28
2.4.2 The non-CSW residual	32
2.5 Conclusion	36
References	37
3 Detecting irregularities using pantograph head acceleration	41
3.1 Introduction	42
3.2 Data description and processing	45
3.2.1 Data description	45
3.2.2 Preprocessing	46
3.2.3 Wavelet packet entropy for CSWs and non-CSW signal	47
3.3 Local irregularity detection	50
3.3.1 Entropy computation with varying windows	50
3.3.2 Local irregularity identification and verification	53

3.4	Results and discussions	54
3.4.1	Results at each scale.	56
3.4.2	Overall results	60
3.5	Conclusion	63
	References.	64
4	Evolvement of contact wire irregularities	67
4.1	Introduction	68
4.2	Measurement data description	70
4.3	Data analysis methods	72
4.3.1	PSD estimation	72
4.3.2	Time-frequency analysis.	74
4.4	Data analysis of wear irregularity	75
4.5	Simulations	78
4.5.1	Simulation of pantograph-catenary interaction	78
4.5.2	Simulation of contact wire wear irregularity	81
4.6	Wear irregularity and pantograph-catenary contact force	82
4.6.1	Influence of singular local wear irregularity	82
4.6.2	Influence of complex distributed wear irregularity	86
4.6.3	From contact force to wear irregularity	89
4.7	Conclusion	90
	References.	93
5	An integral condition assessment approach	97
5.1	Introduction	98
5.2	Bayesian networks	100
5.3	A BN for catenary condition monitoring	102
5.3.1	Graph structure	102
5.3.2	Variable extraction	103
5.3.3	Parameter estimation	110
5.4	A BN-based approach	111
5.4.1	Input	112
5.4.2	Output	112
5.5	Results and performance discussions	113
5.5.1	BN estimation.	113
5.5.2	Reduction in false alarms	117
5.5.3	Comparison with alternative BN structures	120
5.5.4	Tolerance against bad data	120
5.6	Conclusion	123
	References.	125
6	Conclusions and recommendations	129
6.1	Conclusions	130
6.2	Recommendations	135
6.2.1	Future research.	135
6.2.2	Future practice	137
	References.	138

Acknowledgements 致谢	139
Curriculum Vitæ	141
List of Publications	143

Summary

Railway catenary is the main infrastructure that delivers electric power for train operation. It is a structure commonly constructed along the railway line with contact wires suspended above the track. One or multiple pantographs mounted on the roof of a moving train collect electric current from the catenary through the sliding contact with a contact wire. With the increase of train speed and traffic density in recent years, the catenary is subject to higher impacts from pantographs, leading to critical failures such as the breakage of contact wire. This results in not only an increasing cost for reactive maintenance, but also disruptions of train service that affect many passengers.

To reduce the life cycle cost and failure rate of catenary in practice, planned and predictive maintenance is desired based on the condition monitoring of catenary. However, the monitoring data are underutilized to effectively assess the catenary condition and facilitate maintenance decision-making. This dissertation contributes in improving the dynamic condition assessment of catenary using the data from condition monitoring. New performance indicators (PIs) of catenary are defined in a way that is adaptive to the variations of monitoring data measured under different circumstances, such as the changes of catenary structure, pantograph type and train speed. The relationship between the monitoring data and the contact wire irregularities is studied using historical data and simulations. Data-based approaches are developed for the quantitative assessment of dynamic catenary condition.

First, an intrinsic wavelength contained in the pantograph-catenary contact force is identified and defined as the catenary structure wavelength (CSW). It is caused by the periodic variations of contact wire stiffness attributed to the cyclic structure of catenary that must regulate the height of contact wire in every spans and inter-dropper distances. An approach that adaptively extracts the CSWs of pantograph-catenary contact force is proposed based on the empirical mode decomposition algorithm. It extracts the CSW signals corresponding to the span lengths and inter-dropper distances, respectively, summing to form a characteristic signal of CSWs. The residual signal of the contact force excluding the CSWs is regarded as the non-CSW signal. The mean and standard deviation of the CSWs signal are used as PIs to indicate the condition of the main catenary geometric parameters. A PI based on the quadratic time-frequency representation of the non-CSW signal is proposed for detecting and localizing the local irregularities of contact wire. The proposed PIs are tested by simulation and measurement data and proven effective and adaptive owing to the use of CSWs and non-CSW signal.

Second, the concept of CSW is expanded to the pantograph head acceleration from which the CSWs and non-CSW signal can also be extracted using the same approach developed for the contact force. Considering the characteristics of pantograph head acceleration, the wavelet packet entropy of the CSWs and non-

CSW signal is proposed as PIs for detecting contact wire irregularities with different lengths. The entropy of CSWs is used for detecting irregularities with a length longer than 5 m, while the entropy of non-CSW signal is for the short-length local irregularities. An approach to detect and verify contact wire irregularities using the measurement data of pantograph head vertical acceleration from frequent inspections is proposed. The approach is tested using historical inspection data from which irregularities at all lengths are detected and verified. Maintenance resources can thus be specifically allocated to verified detection results to save cost and time.

Third, through analyzing historical inspection data and data-based simulation results, it is found that while the contact wire irregularity deteriorates the pantograph-catenary interaction, the formation of irregularity is also associated with the effects of the interaction like variations of contact and friction forces. Concretely, the contact wire height irregularity with an amplitude of 8 mm can cause considerable increase in the standard deviation of pantograph-catenary contact force. In addition, the irregularity with a certain wavelength can induce the dynamic response with the same wavelength in the contact force. This in turn makes the irregularity part deteriorating faster than the other parts of catenary. At a smaller scale, when the wear irregularity of contact wire has an average wire thickness loss of about 1.5 mm, it can also increase the standard deviation of contact force by more than 5%. Due to the fixing effect at the registration arms and droppers, the wear irregularity commonly contains structural wavelengths of catenary including span lengths and interdropper distances. It is also found that the wear irregularity tends to grow and spread toward in the common or dominant running direction of trains in the specific line. Nevertheless, an existing defect may not affect every pantograph passage and every type of data measured. It is thus advised to measure multiple types of data and perform more frequent inspections to avoid undetected defects.

Last, a data-driven approach using the Bayesian network (BN) to fuse the available inspection data of catenary into an integrated PI is proposed. The BN topology is first structured based on the physical relations between five data types including the train speed, dynamic stagger and height of contact wire, pantograph head acceleration, and pantograph-catenary contact force. Then, tailored PIs are individually defined and extracted from the five types of data as the BN input. As the output of BN, an integrated PI is defined as the overall condition level of catenary considering all defects that can be reflected by the five types of data. Finally, using historical inspections data and maintenance records from a section of high-speed line, the BN parameters are estimated to establish a probabilistic relationship between the input and the output PI. By testing the BN-based approach using new inspection data from the same railway line, it is shown that the integrated PI can adequately represent the catenary condition, leading to considerable reduction in the false alarm rate of catenary defect detection compared with the current practice. The approach can also work acceptably with noisy or partly missing data.

In summary, this dissertation answers how to adequately transform the condition monitoring data of catenary into quantitative assessments of the dynamic catenary condition. The proposed approaches are intended for generic implementations in railway catenaries worldwide.

Samenvatting

Bovenleidingsystemen zijn een essentieel onderdeel van geëlektrificeerde spoorlijnen die zorgen voor het transport van het elektrische vermogen naar de treinen. Het systeem is opgebouwd uit contactdraden met draagkabels en hangdraden die aan palen bevestigd boven het spoor zijn aangebracht. De energietoevoer vindt plaats via bovenop de treinen aangebrachte pantografen met een sleepstuk dat tegen de rijdraad wordt aangedrukt. Als gevolg van een toename van de snelheid en een groeiende verkeersintensiteit worden bovenleidingen zwaarder belast hetgeen kan leiden tot ernstige defecten zoals rijdraadbreek. Dit zorgt niet alleen voor stijgende kosten voor reactief onderhoud maar leidt ook tot treinhinder met veel overlast voor de reizigers.

Verlaging van de life cycle costs en vermindering van de faalkansen van de bovenleiding vergen uitvoering van gepland en voorspelbaar onderhoud op basis van condition monitoring. Echter, de beschikbare monitoring data wordt nog niet volledig benut voor effectieve beoordelingen van de kwaliteit van de bovenleidingsystemen en besluitvorming over onderhoud. Dit proefschrift draagt bij aan de verbetering van de beoordeling van het dynamisch gedrag van bovenleidingen met condition monitoring data. In het promotieonderzoek zijn nieuwe prestatie-indicatoren opgesteld voor de beoordeling van bovenleidingen die kunnen worden aangepast op de variaties in monitoring data die onder verschillende omstandigheden wordt geregistreerd, zoals snelheid van de trein, type pantograaf en constructie van de systemen. Het verband tussen monitoring data en afwijkingen in de rijdraad is onderzocht aan de hand van historische data en simulaties. Tevens zijn op data gebaseerde methoden ontwikkeld voor de kwantitatieve bepaling van het dynamisch gedrag van bovenleidingen.

Allereerst is de intrinsieke golflengte bepaald van de dynamische kracht tussen pantograaf en rijdraad en is deze gedefinieerd als bovenleiding-systeem-golflengte of CSW (catenary structure wavelength). De CSW wordt veroorzaakt door periodieke veranderingen in de stijfheid van de rijdraad die volgt uit het patroon van de bovenleiding voor de afstelling van de rijdraadhoogte over de spanlengte van de draagkabels en de afstand tussen de hangdraden. Een methode wordt voorgesteld voor het adaptief extraheren van de CSW-signalen van de contactkrachten, gebaseerd op een empirical mode decomposition algoritme. De methode extraheert CSW-signalen die overeen komen met de spanlengte en de afstand tussen de hangdraden en die accumuleren tot een karakteristiek signaal. Het gemiddelde en de standaard deviatie van de CSW-signalen zijn prestatie-indicatoren voor afwijkingen in de geometrie van de bovenleidingstructuur. Het resterende deel van het signaal wordt beschouwd als een non-CSW-signaal. Een kwadratische tijd-frequentie weergave van dit signaal-residu wordt voorgesteld als indicator voor de detectie en lokalisering van afwijkingen in de rijdraad. De voorgestelde indicatoren worden

beproefd in simulaties en getoetst aan meetdata uit de praktijk en zijn effectief gebleken door de toepassing van CSW en non-CSW-signalen.

Vervolgens wordt de CSW-benadering toegepast op de versnellingen van het sleepstuk van de pantograaf waarvan eveneens de CSW- en de non-CSW-signalen kunnen worden bepaald. Aan de hand van een nadere beschouwing van de eigenschappen van deze versnellingen wordt voorgesteld om de wavelet packet entropy van zowel het CSW- als het non-CSW-signaal te gebruiken als prestatie-indicator voor de detectie van afwijkingen in de contactdraad met verschillende afmetingen. De wavelet packet entropy van de CSW-signalen wordt toegepast voor de detectie van afwijkingen in de rijdraad met lengtes langer dan 5 m terwijl de entropy van de non-CSW-signalen een maatstaf is voor onregelmatigheden met een kortere lengte. Eveneens wordt een methode voorgesteld voor detectie en bepaling van afwijkingen in de rijdraad op basis van versnellingsdata van het sleepstuk die voortkomen uit veelvuldige inspecties van de bovenleiding. De methode is beproefd met historische inspectie data waarmee afwijkingen in de rijdraad met verschillende lengtes zijn gedetecteerd en gecontroleerd. Door de methode is gerichte planning van onderhoud mogelijk waardoor tijd en geld kan worden bespaard.

Daarna wordt door analyse van de historie van inspectie-data en simulaties aangetoond dat, terwijl de afwijkingen in de rijdraden de interactie tussen pantograaf en bovenleiding nadelig beïnvloeden, het ontstaan van de afwijkingen ook gerelateerd is aan de effecten van de interactie, zoals een variatie in wrijvings- en contactkrachten. Concreet betekent dit dat een rijdraadhoogte-afwijking met een waarde van 8 mm kan leiden tot een aanzienlijke toename van de standaard deviatie van de contactkrachten tussen pantograaf en bovenleiding. Daarbij komt dat een afwijking met een bepaalde lengte een respons kan opwekken in de contactkracht tussen pantograaf en bovenleiding met een zelfde golflengte. Dat kan ertoe leiden dat de rijdraad op de plaats van de oneffenheid sneller verslechtert dan andere delen van de bovenleiding. Daarnaast kan worden gesteld dat een gemiddelde afname van de draaddoorsnede van 1.5 mm leidt tot een toename van de standaard deviatie van de contactkracht van meer dan 5%. Als gevolg van de bevestiging van de rijdraad aan de bovenleidingarm en de hangdraden bevatten aan slijtage gerelateerde afwijkingen CSW's die verband houden met de spanlengte en de afstand tussen de hangdraden. Tevens is vastgesteld dat slijtage-oneffenheden de nijging hebben om zich uit te breiden in de overheersende rijrichting van treinen op een traject. Desondanks kan het zijn dat een bestaand defect niet op alle pantograaf-passages en geregistreerde meetdata invloed heeft. Om te voorkomen dat defecten niet worden ontdekt wordt geadviseerd om verschillende typen data te registreren en veelvuldig inspecties uit te voeren.

Ten slotte wordt een data gestuurde aanpak voorgesteld gebaseerd op een Bayesiaans netwerk (BN) om de beschikbare inspectiegegevens van bovenleidingen te combineren in een integrale prestatie-indicator. De BN-structuur wordt opgesteld aan de hand van de fysieke relaties tussen vijf datatypen waaronder treinsnelheid, horizontale en verticale beweging van de rijdraad, sleepstukversnellingen en de contactkracht tussen rijdraad en pantograaf. Hieruit volgt een beschrijving van specifieke prestatie-indicatoren die worden gebruikt als input voor het BN. Als out-

put van het BN is gekozen voor een prestatie-indicator die de totale conditie van het bovenleidingsysteem uitdrukt, waarbij alle defecten in ogenschouw worden genomen die door de 5 geselecteerde datatypen kunnen worden gerepresenteerd. Afsluitend zijn met historische inspectiedata en onderhoudsgegevens van een onderdeel van een hogesnelheidslijn, BN-parameters bepaald voor het vaststellen van een probabilistische relatie tussen de input en output indicatoren. Uit testen van de op BN-gebaseerde methode met nieuwe meetdata van dezelfde hoge snelheidslijn is gebleken dat de integrale prestatie-indicator een bruikbare weergave oplevert van de gesteldheid van een bovenleidingsysteem, hetgeen resulteert in een verlaging van het percentage foutpositieve detecties vergeleken met de huidige aanpak bij foutlokalisatie voor bovenleidingen. De aanpak leidt ook tot acceptabele resultaten als de data vervormd is of een wanneer deel van data ontbreekt.

Samenvattend: dit proefschrift beschrijft op welke wijze condition monitoring data adequaat kunnen worden omgezet in kwantitatieve beoordelingen van de dynamische gesteldheid van bovenleidingsystemen. De voorgestelde methoden zijn bedoeld voor universeel gebruik ten behoeve van bovenleidingsystemen op mondiale schaal.

1

Introduction

This chapter introduces the background, challenges, objectives, questions, contributions and outline of the research carried out in this dissertation.

1.1. Background

Rail transport is an important means to transfer passengers and goods in many countries. The safe and stable operation of trains relies on a healthy railway infrastructure. To effectively maintain the health condition of railway infrastructure, monitoring and maintenance techniques are commonly employed in practice [1].

One of the main railway infrastructures, the catenary (overhead line) system, provides power to a majority of over 2.8×10^5 km of electrified railway worldwide. Electricity generated by a power station is transmitted to the traction substations located along a railway line. The substations transform the electric voltage to the nominal voltage of the line and distribute the voltage on the catenary. Figure 1.1 shows the basic components of catenary including the contact wire, messenger wire, dropper, mast and support structure installed on the mast. When a train is running on the rail, it can continuously collect electric current from the contact wire suspended along and above the rail. The current flows from the catenary to the train locomotive through the sliding contact between the contact wire and one or multiple pantographs mounted on the train roof.

The catenary is mainly subject to the repetitive impact of pantographs and the influence of environmental factors such as temperature, wind and icing [2, 3]. When a major failure of catenary occurs, such as the breakage of contact wire, it can completely paralyze a section of railway line. It is thus necessary to monitor and maintain the condition of catenary to ensure its functionality.

For the condition monitoring of catenary in conventional lines, the geometric parameters of contact wire are inspected by specialized measurement trains [4]. As schematically shown in Figure 1.2, the interval between parallel dashed lines indicates the variation ranges of the height, stagger and thickness of contact wire,

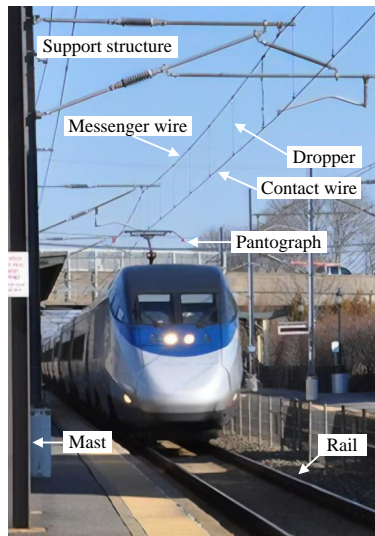


Figure 1.1: Components of railway catenary, pantograph and rail.

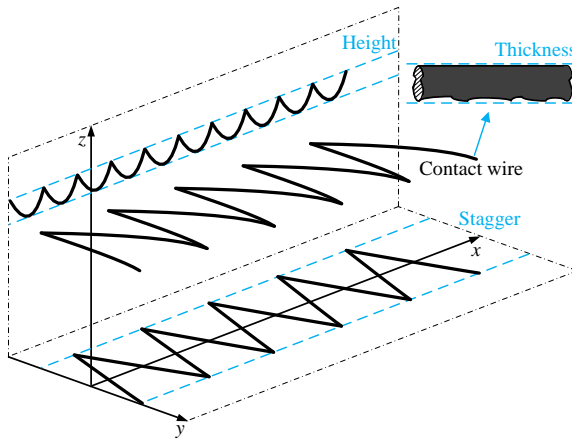


Figure 1.2: Geometric parameters of the contact wire of catenary. Axis x denotes the direction of rail.

which are the main geometric parameters inspected. The pre-operation condition of a static catenary can be assessed in this way. The inspections are often carried out periodically every year or half a year. The spatial position and wear of contact wire are assessed to determine if the wire needs to be regulated or replaced. However, with the speed upgrade of conventional lines and construction of high-speed lines in recent years, the monitoring of geometric parameters becomes insufficient, because

1. The dynamic performance of catenary cannot be directly reflected and assessed using the geometric parameters that indicate the static condition of catenary.
2. Maintenances determined and performed based on geometric parameters cannot effectively mitigate or eliminate catenary defects, as some defects are not indicated by geometric parameters.
3. In current practice, catenary inspections are mostly carried out once or twice a year. This period between inspections is too long to capture the short-term degradation and defects of catenary.

To address the aforementioned issues, monitoring and assessing the dynamic responses of catenary during operation is becoming more preferred in practice [5, 6]. In the interaction between catenary and pantograph as schematically shown in Figure 1.3, dynamic parameters including the pantograph-catenary contact force [7–9], pantograph head (collector) vertical acceleration [4], contact point displacement [10] and the dynamic height and stagger of contact wire [11], are measured to assess the dynamic performance of catenary. Besides the geometric and dynamic parameters, components of the catenary support structure, such as insulator, iso-electric line, etc. are also monitored [12–14] as they are important for ensuring the full functionality of catenary. Meanwhile, the inspection frequency for the catenary system is also required to be improved by technical standards. For example, a desired inspection period of 10 days is required by the national standard of China for

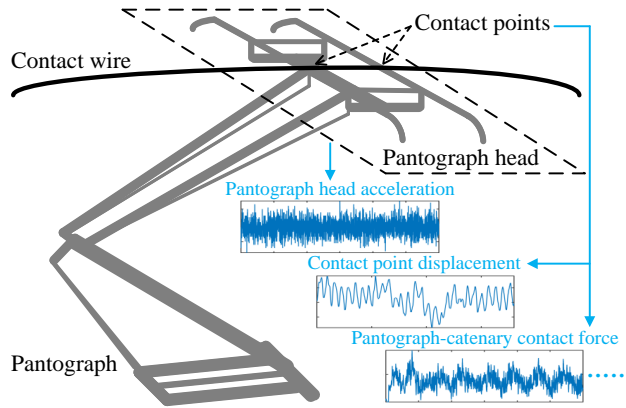


Figure 1.3: Schematic of the pantograph-catenary interaction and typical dynamic parameters.

high-speed railways [15]. As a result, the variety, velocity and volume of monitoring data for the catenary system are rapidly increasing.

With massive monitoring data collected, a crucial task now is to transform data into information that indicate and quantify the catenary condition for maintenance decision-making. This is commonly realized by defining and extracting performance indicators (PIs) from the data. Traditionally, data are directly compared with predefined thresholds and classified as normal or abnormal. This is however insufficient for maintenance decision-making as the type and severity of catenary defect still remain unclear. With the dynamic parameters measured, it becomes possible to extract PIs that are more informative, because the dynamic responses of catenary and pantograph are contained in the dynamic parameters. Therefore, the usage of available monitoring data brings huge potentials in improving the catenary condition assessment.

This dissertation studies approaches to utilize monitoring data for improving the condition assessment of catenary. More specifically, data-based catenary condition assessment through PI definitions and data processing approaches are explored. Simulations of the pantograph-catenary interaction under healthy and unhealthy conditions are carried out to provide data sources. In-situ monitoring data of catenary from both the Chinese and Dutch railway are also used for case studies.

1.2. Challenges for the condition monitoring of railway catenary

This section describes the main challenges in the research of catenary condition monitoring that will be addressed in this dissertation.

1.2.1. From data to assessment

The emerging data from monitoring the dynamic responses of pantograph-catenary interaction provide unprecedented opportunities to improve the condition assess-

ment of catenary. As a start, it is essential to acquire the expected dynamic responses to establish a baseline for condition assessment. This can be done mathematically by modeling and simulating the interaction between a specific couple of catenary and pantograph. For years, finite element method (FEM) has been widely used for pantograph-catenary simulation, resulting in a recent worldwide benchmark [16] and an update of the European standard EN 50318 [17]. The simulation results provide an approximation of reality that can be validated by hardware-in-the-loop hybrid simulations [18, 19] and in-situ measurements [20]. This provides sufficient research basis to establish PIs as baselines for condition assessment considering the differences in catenary structure, pantograph type and operation condition for various railway lines. Then, diagnostics of catenary can be developed and performed by comparing the PIs extracted from monitoring data with the baseline PIs.

Until now, the PIs and baselines using the dynamic parameters of catenary, except for predefined thresholds, are seldom considered. In the literature, data processing methods such as the statistic distribution, kurtosis and power spectrum of the dynamic parameters were employed to analyze the dynamic characteristics of catenary and pantograph [8, 21, 22]. Consequently, some PIs were developed for diagnosing the catenary condition, such as the power spectrum of pantograph-catenary contact force [7] and the root mean square of pantograph head vertical acceleration [4]. These PIs mostly target for a certain type of catenary defect. However, the catenary condition should be comprehensively assessed depending on the dynamic parameters measured at different railway networks. This requires multiple PIs to be defined and formulated on the different type of dynamic parameter, so that the diagnostics of catenary can cover most of its defects. Accordingly, baselines for catenary diagnostics can be established using PIs extracted from the available measurement data. Finally, new monitoring data can be transformed into PIs that will be compared with the baselines to assess the catenary condition.

In short, the transformation from the monitoring data of dynamic parameters to the baselines of diagnostics can enable the effective and comprehensive catenary condition assessment. While there are monitoring data available, such baselines for the dynamic parameters of catenary are lacking. Therefore, research on how to establish such baselines for catenary diagnostics is important and imminent.

1.2.2. From assessing the present to the future

While diagnosis determines the current problems of a system, prognosis foresees the development of the current problems. Accordingly, the maintenance strategy for catenary can be improved from a find-and-fix practice to predictive actions. To this end, the degradation pattern of catenary condition should be acquired. Theoretically, this pattern can be estimated by accumulating the effects of pantograph-catenary interaction and environmental disturbances through simulations. It can also be empirically quantified by associating the monitored catenary condition with the change of PIs over time. This requires a large amount of historical monitoring data and maintenance record together with accurate positioning information stored as a source of data and information. In addition, the operation condition

of the targeted catenary, such as the operation speed, traffic density, scheduled maintenance and the operational changes of them, should also be considered when quantifying the rate of degradation and assessing the condition evolution.

The prognostics for catenary condition assessment are still a relatively new research topic lacking scientific contributions. A major reason is that, as stated before, the PIs and baselines for catenary diagnostics are not sufficiently developed to provide indicators and criteria to assess the catenary condition. This makes it unreliable to pursue the prognostics of catenary, which requires an accurate assessment of the condition evolution. In recent years, the prognostics of mechanical and electronic systems, sometimes referred as the prognostics and health management [23, 24], are rapidly advancing to fulfill the emerging need for increasing the system reliability, availability and safety through a cost-effective manner. It has also become possible to predict the catenary condition with years of condition monitoring data accumulated in practice. The monitoring data, for example, the pantograph-catenary contact force changes with the degradation of catenary over time [25], providing opportunities to perceive the changes from data. The prognostics of catenary can then be performed based on the perceived changes associating with the condition degradation.

However, the relationship between the condition monitoring data and the condition degradation of catenary is yet to be established. This is the first step for ultimately assessing the catenary condition in the near future.

1.2.3. From manual data processing to adaptive approaches

When developing diagnostics or prognostics for catenary condition assessment, a realistic problem facing researchers and engineers is to deal with the differences in the catenary structure, pantograph type and the coupling pantograph-catenary interaction. The differences encountered in practice include one or the combination of the following situations:

1. The catenary structure changes along a railway line.
2. The catenary structure changes between different railway lines.
3. The pantograph type employed for data collection changes for different railway lines.
4. The length of contact wire irregularities caused by catenary defects is different depending on the type of defect.
5. The operation condition, particularly the speed of inspection trains, changes during inspections.

When considering the catenaries operated worldwide, greater differences can be found between continents and countries. These differences lead to the varying dynamic characteristics of pantograph-catenary interaction, which are inherited by the data of dynamic parameters measured from inspections. It is thus important to properly extract the varying characteristics, in terms of PIs, through data processing

techniques. In other words, potential PIs should be varying depending on the time, location and speed when the data are measured and the type of defect encountered.

In the literature, the aforementioned issue was circumvented to some extent by narrowing down the research objectives. Studies that deal with one type of catenary defect, data from a fixed section of railway line or data measured under approximately constant speed are the common simplifications [4, 7, 26, 27]. The applicability of the proposed approaches declines when dealing with data from a longer section of railway line and even a railway network, since more differences are bound to be contained in the data. Therefore, it is important to develop data processing approaches that are more generic to adapt the data, instead of manually adjusting or changing the existing approaches whenever a new circumstance appears in the data. Such adaptive approaches that automatically process data and output PIs of catenary condition have a huge potential to be implemented in asset management for saving time and cost.

So far, the adaptive realization of data processing for catenary condition assessment is still a major research issue. Although there are adaptive signal processing techniques available [28], the dynamic characteristics of pantograph-catenary interaction and the length variations of contact wire irregularity must be considered when defining and extracting PIs. However, it is challenging to identify the consistency or similarity in the catenary data to adapt the effects of differences.

1.3. Research objectives and questions

The objective of this dissertation is to develop data-based approaches for improving the dynamic condition assessment of catenary. It includes defining PIs based on measurement data of the catenary dynamic parameters, developing adaptive approaches to extract the defined PIs from data, acquiring the relationship between the dynamic parameters and the existing and degrading contact wire irregularities, and developing data-based approaches for assessing the dynamic catenary condition.

To achieve the research objectives, the following research questions will be answered:

1. What types of PIs based on the measurement data of catenary dynamic parameters are suitable for the condition assessment of catenary?
2. Which PIs are adaptive to the differences contained in the measurement data of dynamic parameters?
3. How to adaptively extract the PIs from the measurement data?
4. How is the contact wire irregularity affecting the pantograph-catenary interaction?
5. How is the contact wire irregularity evolving with the effects of pantograph-catenary interaction?
6. How to assess the catenary condition using the data-based PIs?

1.4. Dissertation contributions

This section summarizes the main contributions of this dissertation. The contributions are distinctively presented depending on the scientific or societal nature of contributions.

1.4.1. Scientific contribution

The main theoretical or methodological contributions of this dissertation are as follows:

1. *The concept of catenary structure wavelength*

The concept of catenary structure wavelength (CSW) is proposed in Chapter 2 for defining the data-based PIs of catenary. It is defined as the inherent wavelength components contained in the dynamic parameters of catenary, such as the pantograph-catenary contact force and pantograph head vertical acceleration, which are caused by the stiffness variation of contact wire due to the approximately cyclic structures of catenary.

2. *An adaptive method to extract the CSWs*

An approach that is adaptive to the variations of catenary dynamic parameters is proposed in Chapter 2 for extracting the CSWs. The approach is developed based on the empirical mode decomposition [29]. It is then employed in Chapter 2, 3 and 5 to extract the CSWs from the measurement data of pantograph-catenary contact force and pantograph head vertical acceleration.

3. *A PI from the pantograph-catenary contact force to detect contact wire irregularities*

A PI of catenary extracted from the pantograph-catenary contact force is proposed. It is defined as a quadratic time-frequency representation of the CSWs and non-CSW components of contact force using cone-shaped kernels [30].

4. *A PI from the pantograph head vertical acceleration to detect contact wire irregularities*

A PI of catenary extracted from the pantograph head vertical acceleration is proposed in Chapter 3 for when the contact force measurement is not available. Considering the characteristics of the acceleration, the PI is defined as the wavelet packet entropy [31] of the CSWs and non-CSW components of the acceleration.

5. *An automatic approach to detect contact wire irregularities considering frequent inspections*

An automatic detection approach is proposed in Chapter 3 using the PIs extracted from the pantograph head vertical acceleration. A varying window strategy is proposed for detecting the irregularities with different scales in length. A criterion to verify the potential irregularities is defined based on the repeatability of PIs from multiple and frequent inspections.

6. *The relationship between the evolvement of contact wire wear irregularity and the pantograph-catenary interaction*

In Chapter 4, using the historical inspection data of contact wire wear and simulations of pantograph-catenary interaction under the effects of wear irregularities, the mutual influences are identified between the evolvement of wear and the pantograph-catenary contact force. This provides insights for the prognostics of catenary.

7. *A data-driven approach to assess the catenary condition combining multiple inspection data types*

A data-driven approach that assesses the overall catenary condition is proposed in Chapter 5 based on the Bayesian network [32]. Multiple types of data including the dynamic height and stagger of contact wire, pantograph-catenary contact force, pantograph head vertical acceleration, and the inspection train speed are combined to formulate an integrated PI through a new Bayesian network defined for catenary condition assessment.

1.4.2. Societal contribution

The main societal contributions of this dissertation are as follows:

1. *Improving the condition monitoring and maintenance of catenary in railway industry*

The proposed data-based condition assessment approaches are tested by historical inspection data in railway industry. They are proven to be useful and effective in the cases presented. They are also designed to be adaptive for general applications by railway asset managers to improve the condition monitoring and maintenance of catenary.

2. *Reducing the number of railway disruptions caused by catenary failures*

The data-based PIs can be employed as the input for maintenance decision support. Condition-based maintenance can be triggered by applying the data-based condition assessment approaches or the degradation patterns found. This can help to mitigate or eliminate existing catenary defects that will potentially cause disruptions of train service. For both operators and passengers, the safety and punctuality of train service can thus be improved.

1.5. Dissertation outline

This dissertation consists of six chapters. A flowchart of the dissertation shown in Figure 1.4 clarifies the relationships between the chapters. Chapter 2 and 3 focus on using the main dynamic parameters of catenary for detecting contact wire irregularities. Chapter 4 investigates the evolvement of contact wire irregularity for catenary prognosis. Chapter 5 presents an integral approach for catenary condition assessment. Chapter 6 concludes the dissertation with the main contributions and recommendations for future research and practice. A brief description of the remaining chapters are as follows:

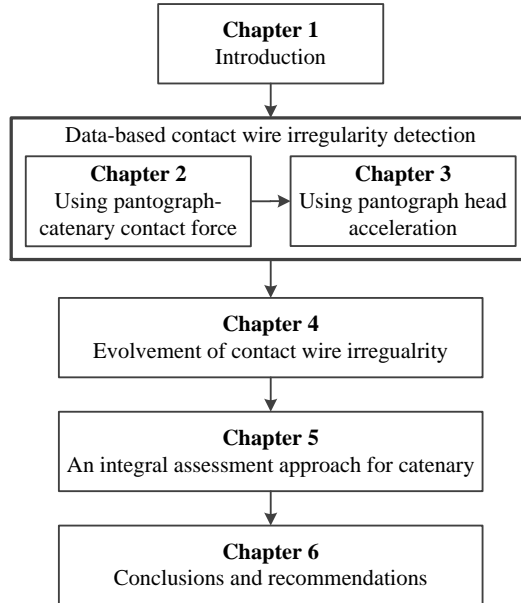


Figure 1.4: Flowchart of the dissertation structure.

Chapter 2 first introduces the concept of CSW contained in the pantograph-catenary contact force. An adaptive approach to extract the CSWs from the contact force is proposed, which takes into account the variations of catenary structure, pantograph type and train speed. The approach is tested using simulated and measured contact force data and proven to be effective for extracting the CSWs and non-CSW signal. The extracted signals can also improve the accuracy of contact wire irregularity detection combining with a new PI defined based on a time-frequency representation.

As a substitute for the contact force, the vertical acceleration of pantograph head is more cost-effective to measure in practice. To apply the vertical acceleration for catenary condition assessment in **Chapter 3**, the CSW of the acceleration is first discussed and compared with that of the contact force. Accordingly, a new PI based on the wavelet packet entropy is proposed using the extracted CSWs and non-CSW signal of pantograph head vertical acceleration. An automatic approach to detect contact wire irregularities having different lengths is proposed using the PI and considering frequent inspections. Historical inspection data are employed to demonstrate the good detection performance of the approach.

Chapter 4 investigates the evolution of the wear irregularity of contact wire using the measurement data of contact wire thickness. The relationship between the wear irregularity and the pantograph-catenary interaction is studied through simulations using the measurement data and actual structural parameters of catenary and pantograph. The evolution of wear irregularity is found to be closely associated with the span length and dropper distribution of catenary structure and

the running direction of pantograph. The findings provide indications on the assessment of wear irregularity and its evolvement.

Chapter 5 proposes an integral approach for catenary condition assessment aiming to indicate all abnormal catenary conditions. Multiple types of measurement data of catenary are employed and combined as the input data source. One of the machine learning techniques, the Bayesian network is employed to establish a probabilistic relationship between the PIs extracted from the multi-type data to formulate an integrated PI of catenary. Performance analysis using historical data shows that the integrated PI can adequately assess the catenary condition by improving in the hit rate of catenary defect detection compared with the current practice.

Finally, **Chapter 6** draws the conclusions for this dissertation and recommends future research directions and implementations for railway industry.

References

- [1] V. J. Hodge, S. O’Keefe, M. Weeks, and A. Moulds, *Wireless sensor networks for condition monitoring in the railway industry: A survey*, *IEEE Transactions on Intelligent Transportation Systems* **16**, 1088 (2015).
- [2] J. Pombo and J. Ambrósio, *Environmental and track perturbations on multiple pantograph interaction with catenaries in high-speed trains*, *Computers & Structures* **124**, 88 (2013).
- [3] Y. Song, Z. Liu, H. Wang, X. Lu, and J. Zhang, *Nonlinear analysis of wind-induced vibration of high-speed railway catenary and its influence on pantograph–catenary interaction*, *Vehicle System Dynamics* **54**, 723 (2016).
- [4] M. Carnevale and A. Collina, *Processing of collector acceleration data for condition-based monitoring of overhead lines*, *Proceedings of the Institution of Mechanical Engineers, Part F: Journal of Rail and Rapid Transit* **230**, 472 (2016).
- [5] S. Bruni, G. Bucca, M. Carnevale, A. Collina, and A. Facchinetti, *Pantograph–catenary interaction: recent achievements and future research challenges*, *International Journal of Rail Transportation* **6**, 57 (2018).
- [6] Z. Liu, Y. Song, Y. Han, H. Wang, J. Zhang, and Z. Han, *Advances of research on high-speed railway catenary*, *Journal of Modern Transportation* **26**, 1 (2018).
- [7] S. Kusumi, T. Fukutani, and K. Nezu, *Diagnosis of overhead contact line based on contact force*, *Quarterly Report of RTRI* **47**, 39 (2006).
- [8] A. Collina, F. Fossati, M. Papi, and F. Resta, *Impact of overhead line irregularity on current collection and diagnostics based on the measurement of pantograph dynamics*, *Proceedings of the Institution of Mechanical Engineers, Part F: Journal of Rail and Rapid Transit* **221**, 547 (2007).
- [9] P. Boffi, G. Cattaneo, L. Amoriello, A. Barberis, G. Bucca, M. F. Bocciolone, A. Collina, and M. Martinelli, *Optical fiber sensors to measure collector performance in the pantograph–catenary interaction*, *IEEE Sensors Journal* **9**, 635 (2009).
- [10] E. Karakose, M. T. Gencoglu, M. Karakose, I. Aydin, and E. Akin, *A new experimental approach using image processing-based tracking for an efficient fault diagnosis in pantograph–catenary systems*, *IEEE Transactions on Industrial Informatics* **13**, 635 (2017).
- [11] C. J. Cho and H. Ko, *Video-based dynamic stagger measurement of railway overhead power lines using rotation-invariant feature matching*, *IEEE Transactions on Intelligent Transportation Systems* **16**, 1294 (2015).

- [12] Z. Liu, L. Wang, C. Li, and Z. Han, *A high-precision loose strands diagnosis approach for isoelectric line in high-speed railway*, *IEEE Transactions on Industrial Informatics* **14**, 1067 (2018).
- [13] J. Chen, Z. Liu, H. Wang, A. Núñez, and Z. Han, *Automatic defect detection of fasteners on the catenary support device using deep convolutional neural network*, *IEEE Transactions on Instrumentation and Measurement* **67**, 257 (2018).
- [14] G. Kang, S. Gao, L. Yu, and D. Zhang, *Deep architecture for high-speed railway insulator surface defect detection: Denoising autoencoder with multitask learning*, *IEEE Transactions on Instrumentation and Measurement* (2018), 10.1109/TIM.2018.2868490.
- [15] *Overall technical specifications of high-speed railway power supply safety inspection and monitoring system (6c system)*, (2012).
- [16] S. Bruni, J. Ambrosio, A. Carnicero, Y. H. Cho, L. Finner, M. Ikeda, S. Y. Kwon, J.-P. Massat, S. Stichel, M. Tur, et al., *The results of the pantograph–catenary interaction benchmark*, *Vehicle System Dynamics* **53**, 412 (2015).
- [17] *Railway applications—current collection systems—validation of simulation of the dynamic interaction between pantograph and overhead contact line*, (2018).
- [18] A. Facchinetti and S. Bruni, *Hardware-in-the-loop hybrid simulation of pantograph–catenary interaction*, *Journal of Sound and Vibration* **331**, 2783 (2012).
- [19] W. Zhang, G. Mei, X. Wu, and Z. Shen, *Hybrid simulation of dynamics for the pantograph–catenary system*, *Vehicle System Dynamics* **38**, 393 (2002).
- [20] P. Nåvik, A. Rønquist, and S. Stichel, *Variation in predicting pantograph–catenary interaction contact forces, numerical simulations and field measurements*, *Vehicle System Dynamics* **55**, 1265 (2017).
- [21] T.-J. Park, C.-S. Han, and J.-H. Jang, *Dynamic sensitivity analysis for the pantograph of a high-speed rail vehicle*, *Journal of Sound and Vibration* **266**, 235 (2003).
- [22] J.-W. Kim, H.-C. Chae, B.-S. Park, S.-Y. Lee, C.-S. Han, and J.-H. Jang, *State sensitivity analysis of the pantograph system for a high-speed rail vehicle considering span length and static uplift force*, *Journal of sound and vibration* **303**, 405 (2007).
- [23] J. Lee, F. Wu, W. Zhao, M. Ghaffari, L. Liao, and D. Siegel, *Prognostics and health management design for rotary machinery systems—reviews, methodology and applications*, *Mechanical systems and signal processing* **42**, 314 (2014).

- [24] N. M. Vichare and M. G. Pecht, *Prognostics and health management of electronics*, *IEEE transactions on components and packaging technologies* **29**, 222 (2006).
- [25] A. Rønning and P. Nåvik, *Five years of contact force measurements along the dovrebanen railway line: Statistical analysis of the dynamic interaction*, in *ICRT 2017* (American Society of Civil Engineers Reston, VA, 2018) pp. 521–529.
- [26] I. Aydin, M. Karakose, and E. Akin, *Anomaly detection using a modified kernel-based tracking in the pantograph–catenary system*, *Expert Systems with Applications* **42**, 938 (2015).
- [27] H. Wang, Z. Liu, Y. Song, X. Lu, Z. Han, J. Zhang, and Y. Wang, *Detection of contact wire irregularities using a quadratic time–frequency representation of the pantograph–catenary contact force*, *IEEE Transactions on Instrumentation and Measurement* **65**, 1385 (2016).
- [28] D. G. Manolakis, V. K. Ingle, S. M. Kogon, et al., *Statistical and adaptive signal processing: spectral estimation, signal modeling, adaptive filtering, and array processing* (McGraw-Hill Boston, 2000).
- [29] N. E. Huang, Z. Shen, S. R. Long, M. C. Wu, H. H. Shih, Q. Zheng, N.-C. Yen, C. C. Tung, and H. H. Liu, *The empirical mode decomposition and the hilbert spectrum for nonlinear and non-stationary time series analysis*, *Proceedings of the Royal Society of London. Series A: Mathematical, Physical and Engineering Sciences* **454**, 903 (1998).
- [30] Y. Zhao, L. E. Atlas, and R. J. Marks, *The use of cone-shaped kernels for generalized time-frequency representations of nonstationary signals*, *IEEE Transactions on Acoustics, Speech, and Signal Processing* **38**, 1084 (1990).
- [31] D. Wang, D. Miao, and C. Xie, *Best basis-based wavelet packet entropy feature extraction and hierarchical eeg classification for epileptic detection*, *Expert Systems with Applications* **38**, 14314 (2011).
- [32] T. D. Nielsen and F. V. Jensen, *Bayesian networks and decision graphs* (Springer Science & Business Media, 2009).

2

Detecting irregularities using contact force

This chapter explores the use of pantograph-catenary contact force (PCCF) for detecting contact wire irregularities. The concept of catenary structure wavelength (CSW) is proposed as the dominant component of PCCF. It describes the signal components caused by the cyclical catenary structure in span lengths and interdropper distance. To obtain the CSWs and non-CSW residual of PCCF, an automatic extraction approach based on the ensemble empirical mode decomposition (EEMD) is proposed. In the approach, the instantaneous frequency of each intrinsic mode function generated by EEMD is employed for the extraction of CSWs. Some selected trials on the PCCF data from simulation and measurement are performed and indicate that the extraction approach is adaptive to the PCCF under various circumstances, including different operation speed, pantograph type and catenary structure. Analyses on the extracted CSWs and non-CSW residual show that, with certain tolerance against measurement noise, the approach can make contact wire irregularities easier to detect.

Apart from minor updates, this chapter has been published as: Z. Liu, H. Wang, R. Dollevoet, Y. Song, A. Núñez, and J. Zhang, "Ensemble EMD-based automatic extraction of the catenary structure wavelength from the pantograph-catenary contact force", *IEEE Transactions on Instrumentation and Measurement*, 2016, 65(10): 2272-2283.

2.1. Introduction

In recent years, the high-speed railway (HSR) industry is expanding extensively all over Europe, Asia, Oceania and North America for promising economic benefit and social development [1, 2]. The assuring safe operation of railway rolling stock at high speed is the very foundation and the major advantage of HSR. To ensure the stability of HSR along with the continuous increase of train speed, the dynamic performance of the entire HSR system should be improved simultaneously. One of the most critical dynamic performance indexes is the quality of the current collection of the high-speed locomotives, which measures the efficiency in the transmission of the power from the catenary to the locomotive. The pantograph-catenary sliding contact above the locomotive roof determines the quality of current collection to a great extent. However, considering the flexibility and nonlinearity of catenary suspension [3], the pantograph-catenary sliding contact is relatively vulnerable to the excitations caused by anomalies. Currently, with the higher operation speeds leading to higher oscillations of catenary suspension [4], the pantograph-catenary interaction requires significant attention now more than ever. It is one of the key components that limit the speed upgrade of HSR. It requires an optimal design and efficient operation and maintenance as a whole system, together pantograph and catenary.

Mechanically, as the crucial and required measurement data that reflects the pantograph-catenary sliding contact [5], the pantograph-catenary contact force (PCCF) must be maintained in an acceptable range during operation [6]; otherwise, arcs [7] or severe wear [8] will occur. The PCCF normally contains certain waveforms that characterizes the periodicity of the catenary structure despite of the pantograph type. As schematically shown in Fig. 1, the catenary suspension is mainly composed of the contact wire, messenger wire, dropper, supporter, and so on. In an anchoring section, the tension that can be exerted on the both ends of contact wire or messenger wire is finite. To maintain the contact wire in an adequate position, the catenary is constructed as the cyclical structure shown in Figure 2.1. Thus, the nominal configuration of a catenary suspension is strictly periodic if the span and interdropper distances are uniform in an anchoring section [9]. In practice, although the actual configuration of catenary suspension is inevitably distorted compared with design, the periodicity can still be generally remained.

Consequently, in previous studies concerning pantograph-catenary interaction,

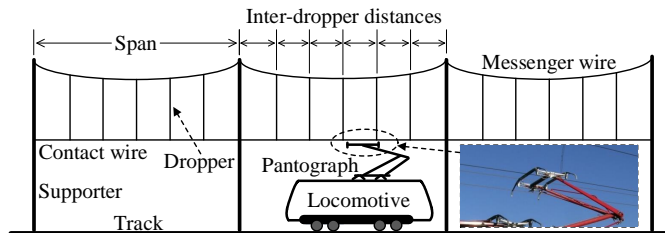


Figure 2.1: Schematic of the pantograph-catenary system.

the periodicity of catenary structure can be constantly identified in the PCCF signals from either simulation results or real-life measurements. In order to investigate the frequency-domain characteristics of PCCF, the Fourier transform and the power spectrum density are frequently adopted [10–15]. As a result, the frequency components that characterize the span and interdropper distance can be observed from the frequency domain of PCCF. Thus, in this chapter, the term Catenary Structure Wavelength (CSW) is proposed to represent all the signal components caused by the cyclical structure of the soft catenary.

To the best of our knowledge, the CSWs inevitably exist in PCCF as long as the soft catenary suspension is adopted for the purpose of power transmission in HSR. In fact, due to the variation of contact wire elasticity along the catenary, the CSWs generally occupy a large proportion of energy in PCCF, which makes other signal components that may be caused by anomalies such as contact wire irregularity [14], contact strip wear [16], environmental perturbation [17], etc. almost unobservable. Therefore, the extraction of the CSWs in PCCF can be useful in the following two aspects:

1. The obtained CSWs are the dominant signal components in PCCF, which can reveal the overall trend and fluctuation of PCCF. Also, the CSWs are highly sensitive to the positional deviations occurred in catenary structure. Thus, the CSWs can be used to evaluate the overall quality of pantograph-catenary interaction.
2. With the elimination of CSWs, the residual is the PCCF containing the signal components that are caused by all other factors except for the catenary structure. In the residual, all the anomalies that may exist in the pantograph and catenary or occur in the pantograph-catenary interaction will be contained.

Therefore, this chapter aims to develop a generic filtering approach to extract the CSWs in PCCF. Considering the variety of catenary structure, pantograph type, measuring method and measurement condition in different areas and scenarios, the extraction should be adaptive to any PCCF measurement data. The required prior information are simply the ranges of span and interdropper distance in the measured catenary structure, which can also be substituted by the commonly designed ranges of the two distances. Regarding to the extraction of specific frequency components in a multicomponent signal, the well-known Fourier transform [18] and wavelet transform [19] are potential candidates. However, the major frequency components of PCCF shift as the catenary structures are diverse for different railway lines. Even for the same railway line, the catenary structure is not absolutely uniform and consistent along the entire line. If the Fourier transform or wavelet transform were adopted in this case, the major frequency components need to be identified prior to the decomposition of PCCF, which is difficult to implement when dealing with signal segments from a large dataset and sometimes with unavailable measurement condition. Addressing this issue, with the invention of empirical mode decomposition (EMD) [20], the self-adaptive decomposition of multicomponent signal provides a more suitable way for the purpose of CSW extraction. Theoretically, EMD can decompose a PCCF signal into several intrinsic mode

Table 2.1: Parameters of the simple catenary model.

Type	Value	Type	Value		
Span	48 m	Encumbrance	1.6 m		
Installation height	5.3 m	Stagger	± 0.2 m		
Contact wire	Tension	27 kN	Total distance	14 spans	
	Line density	1.07 kg/m	Maximum pre-sag of contact wire	5‰ Span	
	Tensile rigidity	10^6 N/m	Number of droppers per span	5	
Messenger wire	Tension	21 kN	Element length	0.125 m	
	Line density	1.07 kg/m	Dropper	Line density	0.14 kg/m
	Tensile rigidity	10^6 N/m		Tensile rigidity	10^5 N/m
Inter-dropper distances in a span	5 m/9.5 m/9.5 m/9.5 m/9.5 m/5 m				

functions (IMFs), which automatically sifts out the major frequency components in the signal, regardless of the various sources of PCCF. That is to say, the generated IMF itself might be the exact CSW if the EMD is properly performed on the PCCF signal. In this case, using the enhanced EMD, i.e. the ensemble EMD (EEMD) [21], the CSW extraction is automatically realized as an extension for the convenience of anomaly detection in PCCF analysis [22]. It can filter out the CSWs in PCCF and facilitates further developments in the efficient design of maintenance strategies for the pantograph-catenary system.

The rest of this chapter is organized as follows. A theoretical description of the CSW is given in detail in Section 2.2. The automatic extraction approach for the CSWs is proposed and illustrated in Section 2.3. Section 2.4 presents some validations and possible applications with the results from the extraction approach. The conclusions are drawn and some future developments are suggested in Section 2.5.

2.2. The concept of CSW

Given a proper height of contact wire and initial force acting on the contact wire from a pantograph, the pantograph-catenary system can be functional during a long-distance and high-speed operation. The sliding contact between the contact wire and the pantograph is maintained through the PCCF. To introduce the concept of CSW to PCCF, a brief demonstration of the CSWs is given below by adopting the catenary modelling approach proposed in [3], which is previously verified according to the European Standard EN 50318 [23] and the recent pantograph-catenary simulation benchmark summarized in [24].

The ideal configuration of a simple catenary model, which adopts the actual structure parameters of the Beijing-Tianjin HSR line in China given in Table 2.1,

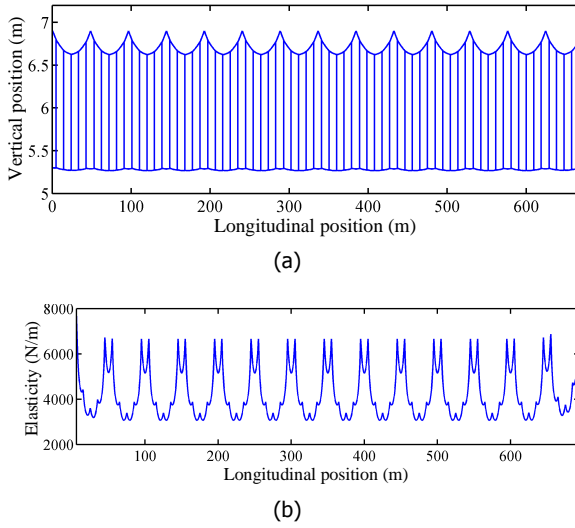


Figure 2.2: (a) Initial configuration of the simple catenary model. (b) The contact wire elasticity under 100N static force.

is shown in Figure 2.2(a). As expected, the periodicity of catenary structure can be observed. Since the pantograph-catenary sliding contact is partly depending on the geometric configuration of catenary, the PCCF should have a correlation with the static contact wire height especially under high speed [15]. From another perspective, by applying a static vertical force on each point of the contact wire, the elasticity of the contact wire can be calculated as the ratio of the force vs. the vertical displacement of the contact point. As a result, the contact wire elasticity of the catenary model is obtained and depicted in Figure 2.2(b). It can be concluded that, not only the geometry of the catenary, but also the response of the contact wire under the action of static force shows certain periodicity in spans and interdropper distances.

Combing the catenary model with the three-level lumped mass model of pantograph depicted in Figure 2.3, which contains three lumped masses m_1 , m_2 and m_3 representing the head, frame and bottom of the pantograph respectively, and three spring-damper elements between adjacent masses and m_3 and the ground, the PCCF can be computed using the frequently adopted penalty function method as follows:

$$\begin{cases} F(k) = K_c(u_p(k) - u_c(k)) & u_p(k) \geq u_c(k) \\ F(k) = 0 & u_p(k) < u_c(k) \end{cases} \quad (2.1)$$

where $F(k)$ the PCCF at the k th sampling point, $u_p(k)$ and $u_c(k)$ are the vertical position of pantograph and contact wire at the sampling point, respectively, and K_c is the contact stiffness between pantograph and catenary, which is $82\,300\text{ N m}^{-1}$ for this model. It can be seen that the PCCF is proportional to the penetration

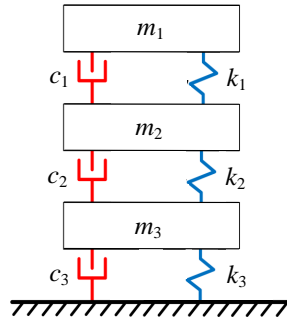


Figure 2.3: The three-level lumped mass model of pantograph.

depth that is calculated partly based on the contact wire height. During an ideal operation with no contact loss, the PCCF at each sampling point depends on the periodic variation of contact wire height, where the periodicity is introduced to the PCCF directly.

Furthermore, Table 2.2 provides the physical parameters of two types of high-speed pantograph in China. The PCCF combining the simple catenary model and the DSA380-type pantograph under the operation speed of 300km/h is computed and depicted in Figure 2.4(a). The sampling interval of PCCF is equal to the element length of contact wire so that no interpolation is performed during the computation. Due to the boundary effect at both ends of the catenary model, the PCCF is unstable in the first and last several spans. Thus, the PCCF in the middle 5 spans indicated by the red lines in Figure 2.4(a) is selected for further analysis. From the power spectrum density of selected PCCF signal depicted in Figure 2.4(b), the frequency components, i.e. the wavelength components that are reflected by the significant peak energies are obtained. Comparing with the structure parameters of catenary, it is straightforward to identify the wavelength components 48.76 m, 9.66 m and 5.36 m as the representation of the span and interdropper distances, which is a common phenomenon in frequency-domain PCCF analysis. In particu-

Table 2.2: The model parameters of pantographs.

Parameter	Pantograph type	
	DSA380	SSS400+
m_1 (kg)	7.12	6.05
m_2 (kg)	6.0	6.4
m_3 (kg)	5.8	14
k_1 (N/m)	9430	5813
k_2 (N/m)	14100	13600
k_3 (N/m)	0.1	0
c_1 (Ns/m)	0	0
c_2 (Ns/m)	0	0
c_3 (Ns/m)	70	64.9

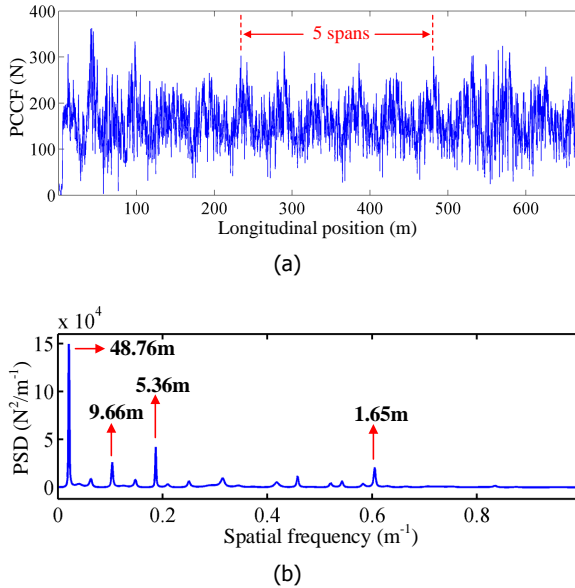


Figure 2.4: (a) The computed PCCF signal and (b) its power spectrum density (PSD).

lar, the wavelength components are almost identical with those in [22] where a different modeling approach is realized based on the same structure parameters of catenary and pantograph. Here, the term CSW is used to characterize the wavelengths caused by spans and interdropper distances. Like shown in Figure 2.4(b), the CSWs are generally the dominant components in a normal or healthy PCCF signal, which endows the CSWs and the non-CSW PCCF with different but significant physical meanings. Hence, based on the concept of CSW, this study focuses on the extraction of CSWs for facilitating the evaluation of current collection quality and the detection of anomalies.

2.3. EEMD-based CSW extraction

2.3.1. EMD algorithm

EMD is a data-driven algorithm that adaptively decomposes a signal into several modes based on neither sinusoidal functions nor mother wavelet functions but the IMFs of the signal itself. Despite of the lack of theoretical support [25], EMD has been widely used in many applications where signal decomposition is needed [26–29]. In some previous studies [30, 31], it is specifically adopted to eliminate the useless or noisy components of a signal. However, the extraction approach in this paper considers both the CSWs and the non-CSW PCCF useful components.

In brief, EMD decomposes a given signal $x(t)$ into a number N of IMFs $d_j(t)$, $j = 1, 2, \dots, N$ and a residual $r(t)$. The sum of all IMFs and the residual matches the

original signal perfectly as follows:

$$x(t) = \sum_{i=1}^N d_j(t) + r(t) \quad (2.2)$$

where each IMF $d_j(t)$ is obtained through an iterative sifting process. For the first IMF $d_1(t)$, starting with a corresponding estimated IMF $d_1^{(i)}(t)$ where the iteration number $i = 1$ and the estimated IMF $d_1^{(1)}(t) = x(t)$, the sifting iteration is described in five steps as follows:

Step 1: Find all the maxima and minima of the signal $d_1^{(i)}(t)$.

Step 2: Connect all the adjacent maxima and minima respectively using spline interpolation to form an upper and a lower envelope $e_u(t)$ and $e_l(t)$ of signal $d_1^{(i)}(t)$.

Step 3: Compute the mean of upper and lower envelopes $e_m(t) = [e_u(t) + e_l(t)] / 2$.

Step 4: Update the estimated IMF $d_1^{(i+1)}(t) = d_1^{(i)}(t) - e_m(t)$ and the number of iterations $i = i + 1$.

Step 5: Repeat Step 1 to Step 4 until a stopping criterion has been satisfied so that the first IMF $d_1(t) = d_1^{(i)}(t)$.

For other IMFs $d_j(t)$, $j > 1$, the corresponding estimated IMF $d_j^{(i)}(t)$ for their first sifting in Step 1 should be

$$d_j^{(1)}(t) = x(t) - \sum_{k=1}^{j-1} d_k(t). \quad (2.3)$$

The conventional stopping criterion in Step 5 for each IMF at its i th iteration can be computed by the standard deviation computed as

$$SD(i) = \sum_{t=0}^T \frac{|d_j^{(i)}(t) - d_j^{(i-1)}(t)|^2}{|d_j^{(i-1)}(t)|^2} < \varepsilon \quad (2.4)$$

where ε is a positive number typically ranges from 0.2 to 0.3 [20] and T is the time duration of signal $x(t)$. The last output of the algorithm is actually the final residual $r(t)$ that represents the mean trend of signal $x(t)$.

From the algorithm above, it can be speculated that the number of IMFs N is automatically determined by the signal itself and the value ε in stopping criterion. As a result of the empirical algorithm, the IMFs have proved to be approximately zero-mean and both amplitude and frequency modulated. Moreover, due to smoothing effect of iterative sifting, the IMFs possess lower and lower frequencies as they are produced one after another. Thus, it is possible for EMD to directly extract the major frequency components in a multicomponent signal, e. g. the PCCF.

2.3.2. EEMD algorithm

As groundbreaking as it is, the conventional EMD still has some shortcomings. In particular, the mode mixing problem caused by signal intermittency leads to frequency aliasing in the IMFs, which mixes disparate signal oscillations into IMFs and impairs the physical meaning of each IMF. However, the physical meaning of PCCF must be preserved in order to obtain authentic CSWs. To resolve this problem, EEMD is proposed based on the dyadic property of EMD when dealing with white noise [21]. It utilizes additional white noise to ensure the full physical meaning of IMFs as described in the following four steps:

Step 1: Add a random white noise series with a constant standard deviation σ to the signal $x(t)$ to form a new signal.

Step 2: Perform the EMD on the new signal to get a set of IMFs.

Step 3: Repeat Step 1 and Step 2 for a number M of times.

Step 4: Compute the final IMFs by averaging all the M sets of IMFs correspondingly.

The added white noises preserve the disparate signal oscillations during every EMD and automatically cancel each other through the averaging in Step 4, so that the final IMFs are not contaminated by the white noises. Note that the final number of IMFs might be different from EMD result due to the added white noise, which is close to $\log_2(P)$ with P the number of total sample points. Comparing with the EMD, two new parameters are introduced to the EEMD algorithm, namely the standard deviation of the added white noise σ and the number of ensemble members M . Both parameters should be carefully chosen as they are relevant to the quality of the final IMFs. Specifically, σ normally ranges from 0.1 to 0.5 times the standard deviation of a given signal $x(t)$, and M can be from 10 to 100 depending on the tradeoff between the effect of white noise cancelation and the requirement of computational efficiency.

With the extracted IMFs from EMD or EEMD, the Hilbert-Huang Transform (HHT) is developed based on the concept of instantaneous frequency, which can provide the Hilbert spectrum of original signal in an energy- time-frequency distribution (TFD) [20]. Concretely, the analytic form of each IMF can be obtained using the Hilbert transform as follows:

$$z_j(t) = d_j(t) + iH[d_j(t)] = a_j(t)e^{i\theta_j(t)} \quad (2.5)$$

where $H[d_j(t)]$ denotes the Hilbert transform of the j th IMF $d_j(t)$ and

$$\begin{cases} a_j(t) = \sqrt{d_j^2(t) + H[d_j(t)]^2} \\ \theta_j(t) = \arctan\left(\frac{H[d_j(t)]}{d_j(t)}\right) \end{cases} \quad (2.6)$$

The instantaneous frequency is defined as

$$\omega_j(t) = \frac{d\theta_j(t)}{dt} \quad (2.7)$$

Then, the Hilbert spectrum of the signal $x(t)$ can be computed by

$$S(\omega, t) = \text{Re} \left[\sum_{j=1}^N a_j(t) e^{i \int \omega_j(t) dt} \right] \quad (2.8)$$

where Re denotes the real part of a complex signal. The Hilbert spectrum reveals the physical meaning of non-stationary data by computing the energy of the instantaneous frequency at each time instant, which shows favorable physical relevancy and high time-frequency resolution in many cases [32]. Thus, it is utilized to quantify and observe the physical meanings of IMFs of PCCF in the following section.

2.3.3. EEMD-based extraction approach

Using the PCCF signal adopted for power spectrum density analysis in Figure 2.4(a) as an example, both EMD and EEMD are directly performed and the generated IMFs are depicted in Figure 2.5(a) and 2.5(b), respectively. Despite that EEMD generates one more IMF than EMD, it can be observed that the first to the seventh IMFs from the two approaches share the similar time-domain waveforms and declines in frequency ranges in the same manner. Among the IMFs, the fifth and seventh IMFs are notable for potential physical meanings that correspondingly indicate the CSWs. Specifically, both seventh IMFs show obvious periodicity in span cycles but local difference in amplitude as circled by dashed lines in the figure. The seventh IMF from EEMD possesses more complete and continuous waveform than the one from EMD. Likewise, the fifth IMF from EMD shows certain sign of intermittency as circled by the dashed lines, which can be regarded as the mode mixing phenomenon. Nevertheless, the corresponding IMF from EEMD effectively alleviates the phenomenon as expected.

Meanwhile, another common problem that occurs during the decompositions is the boundary effect. In the two sets of IMFs depicted in Figure 2.5(a) and 2.5(b), the fourth to the seventh IMFs show signs of boundary effects at both ends of the waveforms, which means that partial signals at the ends are somewhat distorted comparing with those in the middle. To solve the problem, the simulation data outside of the 5-span duration is used as the boundary extension for the PCCF signal. In this case, the actual PCCF signal for EEMD is extended by the 200 adjacent sample points, namely about half a span at both ends of the 5-span signal. Comparisons between the corresponding IMFs that are obtained with and without boundary extension are depicted in Figure 2.6. It can be seen that for the fourth, fifth and seventh IMFs, the general signal oscillation remain the same after boundary extension, whereas some amplitudes, especially at the ends are mildly modified by the extensions.

In the case of real-life measurements, because the PCCF signal adopted for decomposition is normally a segment of a long-duration PCCF measurement data, the boundary extension can still be achieved by using the contiguous sample points besides the segment. An illustration of the boundary extension on a PCCF measurement data is shown in Figure 2.7. The duration of PCCF signal segment should be larger than 3 spans to reflect its periodicity in spans and less than 10 spans (or a

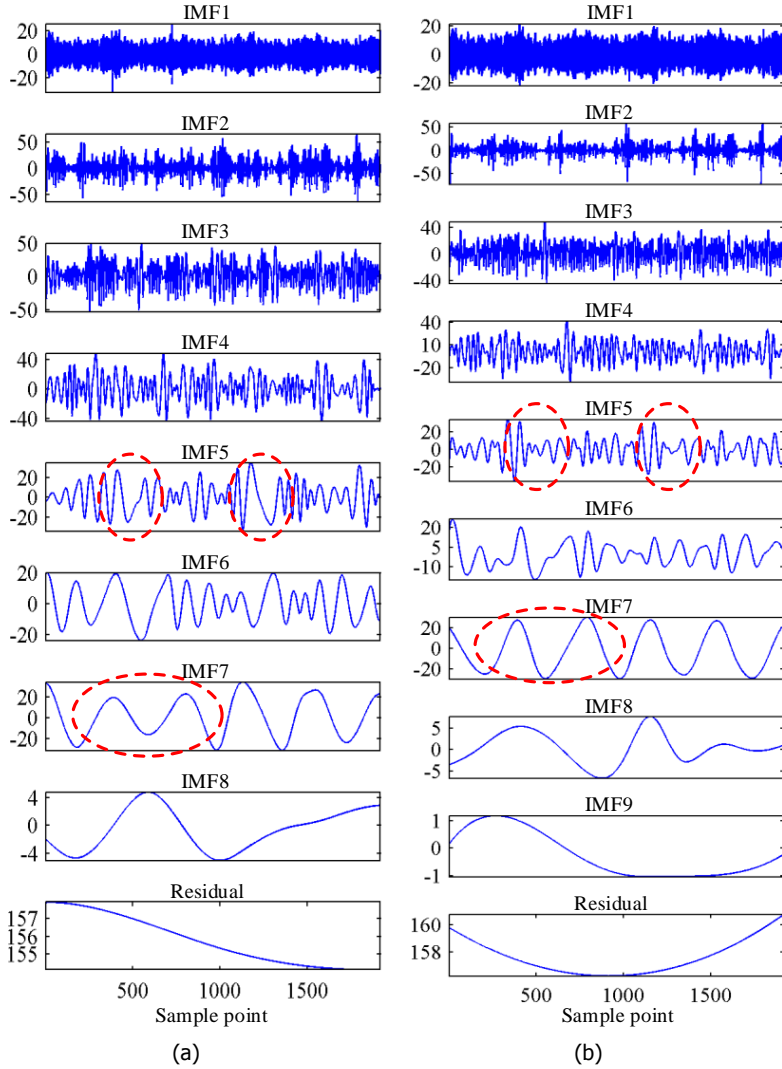


Figure 2.5: IMFs generated by (a) EMD and (b) EEMD with $\sigma=0.2$ and $M=100$.

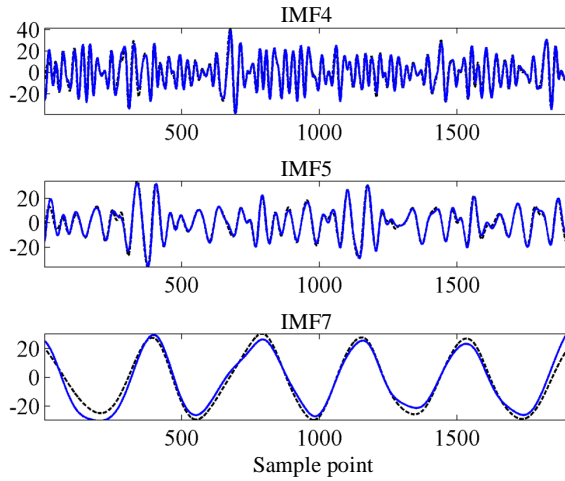


Figure 2.6: IMFs generated by EEMD with (solid lines) and without (dashed lines) boundary extension.

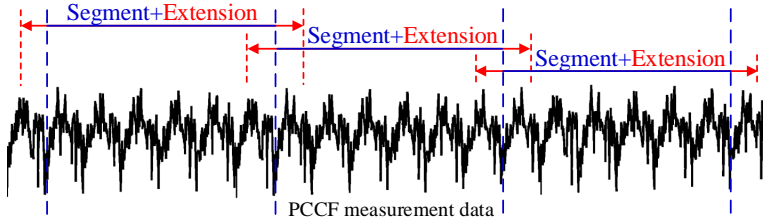


Figure 2.7: Boundary extensions on the segments of a long-duration measurement data.

larger number of spans depending on the sampling interval) for high computational efficiency. Meanwhile, the length of boundary extension should be at least half a span to preserve the integrity of the span wavelength at the boundary of a signal segment.

After the decomposition, the CSWs need to be recognized from all IMFs to accomplish the extraction. The HHT provides the frequency-domain information of all IMFs, which can identify the different frequency range of each IMF. Thus, the CSWs with specific frequency characteristic can be recognized correspondingly. From the above, it is presented that there are two CSWs, namely the span and interdropper distance wavelengths, in the decomposed PCCF signal. After applying HHT on all IMFs, the Hilbert spectrum of the fifth and seventh IMFs are selected and depicted in Figure 2.8(a). Confirming the physical meanings of the two CSWs, the corresponding wavelengths are clearly shown in the figure. In detail, the span wavelength component at around 0.02 m^{-1} is constant and continuous along the longitudinal direction, which occupies the dominant energy in PCCF. The other wavelength component oscillates between the dashed lines corresponding to 5 m and 9.5 m wavelengths with a certain pattern, which matches to the distribution of the interdropper distance in each span given in Table 2.1. For comparison, the ideal TFD of the actual

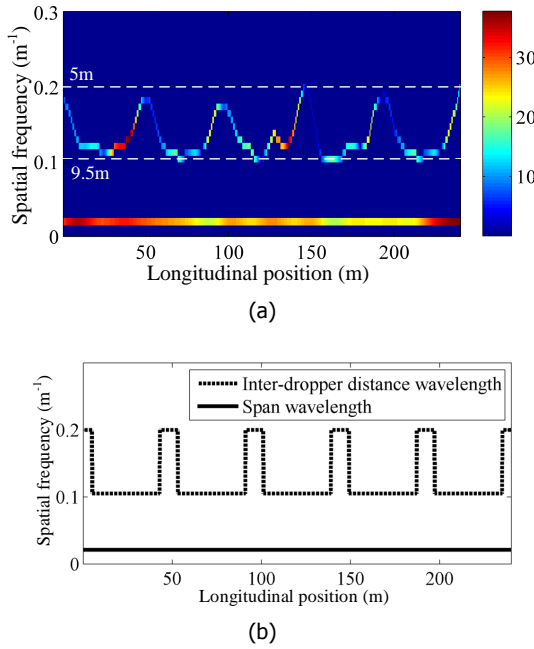


Figure 2.8: (a) Hilbert spectrum of the fifth and seventh IMFs comparing with (b) the TFD of physical structure wavelengths of corresponding catenary.

catenary structure is computed based on corresponding longitudinal position and depicted in Figure 2.8(b). Although the PCCF is the dynamic reflection of catenary structure, its TFD is unlikely to be strictly identical to the TFD of static structure and may deviate due to the dynamic interaction. Thus, it can be speculated that, within a reasonable range, both CSWs are properly reflected by the spectrum and confirming to the actual structure parameters of catenary.

As a result, the sum of the fifth and seventh IMFs representing the CSWs and the rest of IMFs representing the non-CSW residual are depicted in Figure 2.9. While the non-CSW residual shows no indication of significant regularity, it should be noted that the waveform of CSWs is highly similar to the variation of the contact wire elasticity given in Figure 2.2(b), which validates the extraction result.

To realize the extraction process automatically, the frequency range of each IMF can be obtained by (2.7) and adopted for frequency recognition. More specifically, the structure parameters of catenary is variable but within a certain range. Generally, the span is between 40m and 70m and the interdropper distance is between 4m and 10m. Hence, the IMF with the instantaneous frequency ranges from 0.1 m⁻¹ to 0.25 m⁻¹ or 0.014 m⁻¹ to 0.025 m⁻¹ can be recognized as the interdropper distance wavelength or span wavelength respectively. Based on (2.7), the recognition on whether the j th IMF is a CSW can be judged by a Boolean variable

$$\Delta_j = \max[\omega_j(t)] < \omega_u \wedge \min[\omega_j(t)] > \omega_l \quad (2.9)$$

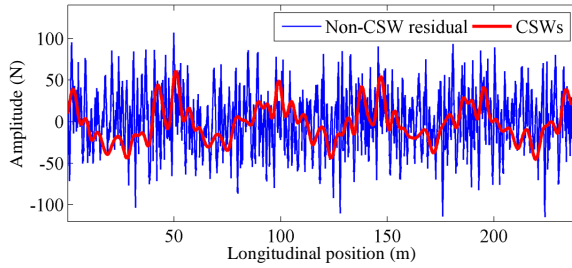


Figure 2.9: Extracted CSWs and non-CSW residual from the PCCF signal.

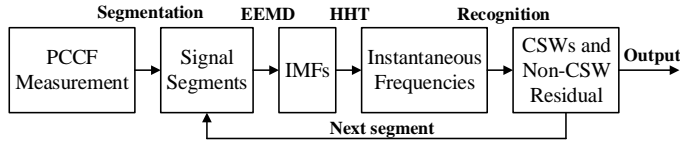


Figure 2.10: Block diagram of the automatic CSW extraction approach.

where \wedge denotes the logical conjunction and ω_u and ω_l are the upper and lower boundary for a certain CSW respectively. Since the signal decomposition based on EEMD and boundary extension can avoid the mode mixing problem between IMFs and ensure the validity of frequency segmentation of PCCF, the automatic recognition process is theoretically feasible. To sum up, Figure 2.10 depicts the block diagram of the automatic extraction approach, which is performed on several examples in the following section. Note that in the step of EEMD, the corresponding boundary extension must be performed on the signal segment beforehand.

2.4. Validation and potential applications

According to the definition of CSW and non-CSW residual in PCCF, this section shows some examples and potential applications of the CSWs and the non-CSW residual separately. The demonstration reflects both the validity and practicability of the proposed extraction approach.

2.4.1. The CSWs

Since CSWs are essentially caused by the catenary structure where the PCCF signal is measured from, it ought to change with the specific parameters of catenary structure. Once the catenary structure is determined, the speed and type of pantograph should not influence the frequency characteristic of CSW, although they may alter the amplitude of CSW. Considering PCCF can be measured from different pantograph-catenary interaction under various operation conditions, it is crucial for the extracted CSWs to be consistent and only sensitive to corresponding structure parameters. Otherwise, the CSWs cannot be useful for reflecting the overall quality of interaction. Thus, the following three cases intend to show that the extraction approach is functioning properly as expected. The 5-span PCCF signal depicted in Figure 2.4(a) and its extraction results are adopted as a reference for comparisons.

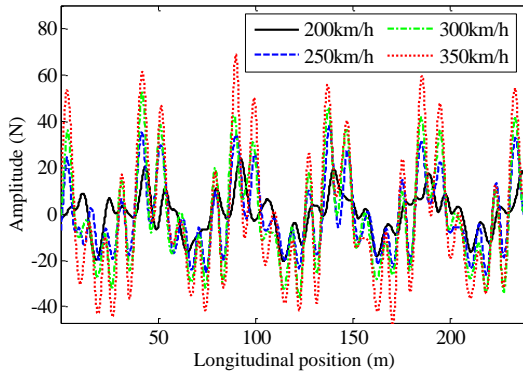


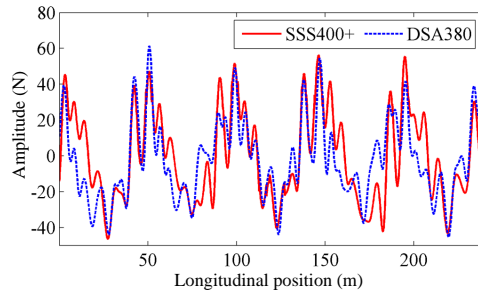
Figure 2.11: Extracted CSWs of PCCF under different operation speed in Case 1.

Case 1: Operation speed

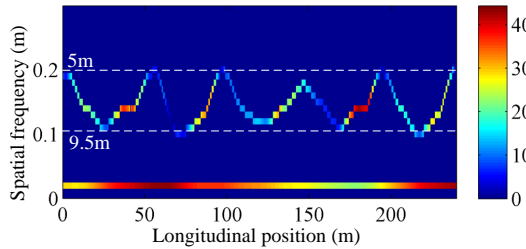
In this case, the PCCF signals adopted for extraction are from the same simulation as the reference but with different operation speed. Figure 2.11 depicts the extracted CSWs of four PCCF signals under operation speed 200 km h^{-1} , 250 km h^{-1} , 300 km h^{-1} and 350 km h^{-1} , respectively. It can be observed that, with the increase of operation speed, the amplitude of CSWs becomes larger due to the higher vibration between pantograph and contact wire. However, the peaks and valleys of the oscillations appear at the same or adjacent positions, which indicate that the periodicity of CSWs remains similar despite of the change of speed. Thus, it shows that the extraction approach works properly under different operation speed. Note that for the PCCF signals measured under nonconstant operation speed, the extraction approach can still be functional because the instantaneous frequencies of CSWs remain unaffected and can be recognized by (2.9).

Case 2: Pantograph type

In this case, the PCCF signal is from the same simulation as the reference, but using the SSS400+ pantograph given in Table 2.2 instead of the DSA380 pantograph. Figure 2.12(a) depicts the comparison between the extracted CSWs from the two types of pantograph. The new CSWs generated by SSS400+ pantograph are similar in general to the CSWs of the reference, but different at some locations due to the differences of the physical parameters of the pantographs. From the Hilbert spectrum of the new CSWs depicted in Figure 2.12(b), it can be seen that, comparing with the reference spectrum in Figure 2.8(a), the instantaneous frequencies of CSWs are within the same and valid frequency range. However, the frequency deviation in TFD is more severe than the reference TFD, namely the new TFD is less similar to the ideal TFD of catenary structure in Figure 2.8(b) than the reference. Considering the definition of CSW, since the reflection of catenary structure in the new PCCF is weakened, this phenomenon can be regarded as a sign of less favorable pantograph-catenary contact quality. The same conclusion can be drawn by comparing the means and standard deviations of the new and reference PCCF signals. Concretely, the means are 155.3 N and 155.2 N respectively and nearly



(a)



(b)

Figure 2.12: (a) Extraction results comparison and (b) CSWs spectrum in Case 2.

identical, whereas the standard deviations are 33.8N and 40.7N respectively, which indicate a relatively unfavorable contact quality in case of SSS400+ pantograph.

Case 3: Catenary structure

In this case, two PCCF signals from completely different pantograph-catenary interactions are adopted for extraction. The first one is the simulation result based on the benchmark model given in [24]. The other is from a real-life PCCF measurement data in a section of the Shanghai-Kunming railway line in China.

In the benchmark model, the main structure parameters of catenary, namely the span is 55 m, and the inter-dropper distance is 4.5 m at both ends of a span and 5.75 m in the middle of a span. Other simulation parameters such as operation speed, sampling interval, total number of spans and so on are all the same. Likewise, the 5-span PCCF signal at the same location in the middle of catenary model is adopted for extraction, whose duration is 35 m longer than the reference. As a result, the CSWs and non-CSW residual are depicted in Figure 2.13(a). It can be seen that, due to the difference of spans, the overall trends of the CSWs have a certain phase difference. Meanwhile, because there are four more droppers in each span of the benchmark model than in the reference model, the oscillations of CSWs in one span is clearly more intensive than the reference CSWs. Therefore, in the corresponding Hilbert spectrum depicted in Figure 2.13(b), the instantaneous frequencies reflecting the inter-dropper distances oscillate within a relatively narrow frequency band that ranges from 4.5 m to 5.75 m in wavelength. In general, the

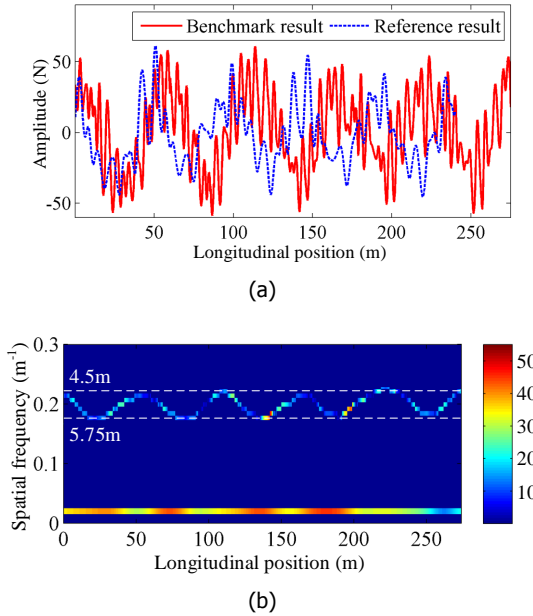


Figure 2.13: (a) Extraction result comparison and (b) CSWs spectrum of the benchmark simulation in Case 3.

extraction approach shows certain adaptability to the variation of catenary structure and pantograph parameters.

In the other trial, a segment of PCCF measurement data with 307.5 m duration and 0.5 m sampling interval is analyzed. The PCCF signal is obtained from an inspection locomotive with pressure and acceleration sensors installed under the contact strip of the pantograph. During the measuring process, the operation speed is consistent and approximately 125 km h^{-1} . There are five spans in the section where the PCCF is measured, which are 65 m, 57.5 m, 55 m, 65 m and 65 m long, respectively. Along the five spans, the droppers are unevenly distributed along the five spans and served a long-term operation. The inter-dropper distances range from 4.5 m to 8 m approximately. Figure 2.14(a) depicts the PCCF measurement data with 98.9 N mean removed and its corresponding CSWs. As a result of the extraction approach, the CSWs favorably exclude the interference of several abnormally high forces and fit the overall trend of PCCF. The result indicates that the non-CSW residual contains the abnormal signal components in the PCCF measurement data. Meanwhile, the amplitude of the CSWs ranges from -15 N to 15 N that is much lower than the amplitude of the reference CSWs in Figure 2.9 due to the lower operation speed. It agrees with the discussion regarding the operation speed in Case 1. Furthermore, from the Hilbert spectrum of the CSWs depicted in Figure 2.14(b), it can be seen that the instantaneous frequencies reflecting the inter-dropper distances oscillate in the actual span cycles in longitudinal direction and between 4.5 m and 8 m wave-lengths in spatial frequency, which meets the expectation of the frequency-domain

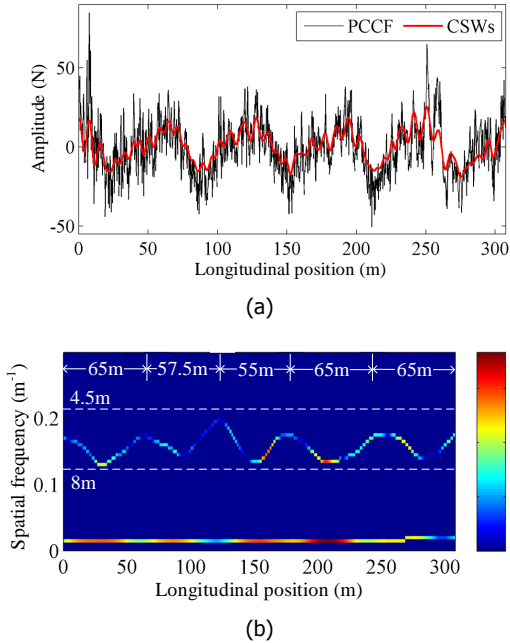


Figure 2.14: (a) The mean-removed PCCF measurement data comparing with its CSWs and (b) the CSWs spectrum of the PCCF in Case 3.

characteristics of CSWs. Although the energy distribution in the spectrum has a weaker periodicity comparing with the ones from simulation data due to complex measurement conditions, the extraction approach still produces the correct results.

To sum up, the proposed extraction approach could be functional for most PCCF signals. Meanwhile, as the dominant energy component in PCCF, the extracted CSWs can reflect the overall trend of PCCF signal in both amplitude and frequency adequately. Note that if certain anomaly happens to excites the frequency component within the frequency range of CSWs, the amplitude and energy of the CSWs will be higher than usual, which can be an indicator of the anomaly.

2.4.2. The non-CSW residual

The non-CSW residual of a PCCF signal is mainly the combined result of high-frequency vibration, measurement noise, environmental disturbance and other possible anomalies in pantograph-catenary system. Since it is essentially the PCCF residual with the elimination of CSWs, it can facilitate the analysis of signal components that are not dominant in PCCF, which contain most hidden information on early-stage anomalies or potential threats to the pantograph-catenary interaction. Tentatively, the following examples show the potential applications of non-CSW residual in the aspects of noise tolerance and anomaly detection.

Noise tolerance

With the capability given by EEMD, the extraction approach can preserve the CSWs from the contamination of measurement noise. In other words, the non-CSW residual shall automatically contain most of the measurement noise, if there is any. Thus, the measurement noises caused by different PCCF measuring system can hardly affect the extraction results.

Using the same simulation PCCF signal depicted in Figure 2.4(a), white Gaussian noise series with different signal-to-noise power ratio (SNR) are added to the signal to test the tolerance of extraction approach against noise. To quantify the effect of noise on the extraction result, a variation coefficient is defined as

$$V = \frac{\frac{1}{T} \sum_{t=0}^T |CSW_n(t) - CSW_r(t)|}{\max[CSW_r(t)] - \min[CSW_r(t)]} \times 100\% \quad (2.10)$$

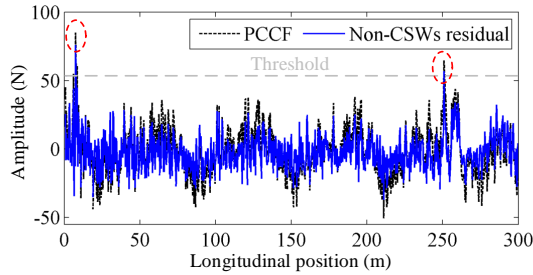
where $CSW_n(t)$ and $CSW_r(t)$ are the extracted CSWs from the PCCF signals with and without additive noise, respectively, and T is the total duration of the CSWs. The variation coefficient calculates the average shifting rate of CSWs comparing with noise-free CSW.

To show the approach performances under low and high SNR noises in different measurement condition, the adopted SNRs of noise range from 0.1 dB to 20 dB. Table III presents the average variation coefficient of 20 trials for each SNR respectively. The variation coefficient remains below 5% at low SNRs, which rarely exist in real-life PCCF measurements. Considering the pressure or acceleration sensor employed in PCCF measurement commonly has the capability to keep the output SNR above 5 dB, which is equivalent to 3.3% variation coefficient at most, the influence of measurement noise on the extraction approach could be negligible. Actually, it enhances the practicability of the extraction approach.

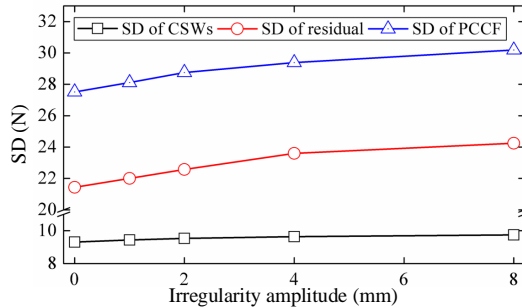
Anomaly detection

Normally, the catenary anomaly cannot influence the CSWs in PCCF since the catenary structure can hardly be altered and the energy of CSWs is too high to be submerged by anomalies. The non-CSW residual can usually preserve the signal components indicating anomalies. As examples, the PCCF measurement data depicted in Figure 2.14(a) and some simulation PCCF data under contact wire irregularity are discussed below with the help of the quadratic time-frequency representation (TFR) for PCCF analysis [22].

In the time domain, the non-CSW residual contains most of the concerned statistical characteristics in the original PCCF, such as abnormal sample point and high standard deviation. Using the same PCCF measurement data depicted in Figure 2.14(a), Figure 2.15(a) depicts the PCCF with mean removed and its corresponding non-CSW residual. When evaluating the amplitude of PCCF, there is a common threshold criterion that considers the PCCF exceeding three times of the standard deviation as an abnormal sample point. Thus, two abnormal points are obtained by the criterion as circled by the dashed red line in the figure. After the extraction,



(a)



(b)

Figure 2.15: (a) The mean-removed PCCF measurement data and its non-CSW residual. (b) Comparisons of the standard deviations (SDs) of PCCF, CSWs and non-CSW residual with respect to the irregularity amplitude.

the non-CSW residual clearly preserves the two abnormal points and keeps the corresponding CSWs unaffected as well. For comparison purposes, some simulation PCCF data from [22] are adopted, in which the contact wire irregularities simulated by 3-m wavelength cosine waveform with 1mm to 8mm amplitude are added to the contact wire. Figure 2.15(b) depicts the standard deviations of the simulation PCCF, the corresponding CSWs and non-CSW residual. It can be observed that as the irregularity amplitude increases, the standard deviation of PCCF becomes higher, which indicates the deterioration of contact quality. As for the extraction results, while the standard deviations of CSWs remains almost constant for all amplitudes, the standard deviations of non-CSW residual show the same increasing trend as the standard deviations of original PCCF. Thus, the extracted non-CSW residual can also preserve the fluctuation characteristic of PCCF properly.

In the frequency domain, Figure 2.16(a) and 2.16(b) depicts the TFRs of the measured and extracted signals in Figure 2.15(a). In the TFR of PCCF, the energy of CSWs is so large that submerges other signal components and leads to most energy locating at around the span wavelength. But in the circled and numbered region 1, 2 and 3 in Figure 2.16(b), there are still signs of other component exist. In the TFR of the non-CSW residual depicted in Figure 2.16(b), the energy of CSWs at the bottom is eliminated and the signal components in region 1, 2 and 3 are some-

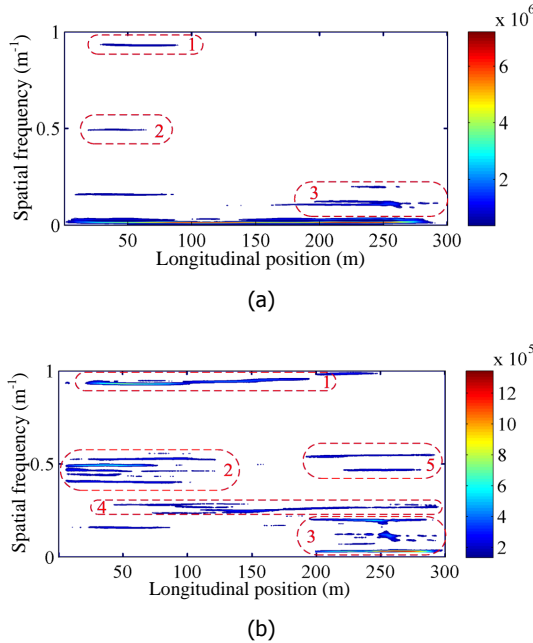


Figure 2.16: Quadratic TFRs of (a) the mean-removed PCCF measurement data and (b) the corresponding non-CSW residual.

how fully revealed and enhanced. In addition, some emerging signal components appear at region 4 and 5. It should be noted that the enhanced or emerging components are not necessarily representing anomalies, because they may be caused by high-frequency vibration and environmental disturbance too. The precise anomaly detection depends on prior information of the normal or previous components in PCCF.

Taking the PCCF adopted in Figure 2.15(b) as an example, the simulation PCCF signal, namely the unhealthy PCCF signal under the global contact wire irregularity with 3 m wavelength and 8 mm amplitude is analyzed. The simulation PCCF signal is the exact same one as in [22] to demonstrate the advantage of the proposed method. Note that in the simulation, the contact wire irregularity is controlled to be the only existing anomaly to test the performance of the extraction approach. In Figure 2.17, the quadratic TFRs of the healthy PCCF, the unhealthy PCCF and the non-CSW residual of unhealthy PCCF are depicted in the left, middle and right, respectively. The color bar of TFR is not given for simplicity. Comparing the middle TFR with the left one, the unhealthy PCCF is influenced by the contact wire irregularity that leads to an emerging signal component appearing at the corresponding wavelength of 3 m. However, as circled by the dashed line, the component is weak in energy and short in duration, which does not meet the fact that the contact wire irregularity is a global one throughout the entire longitudinal position. In the TFR of non-CSW residual on the right, it can be seen that the low-frequency part of

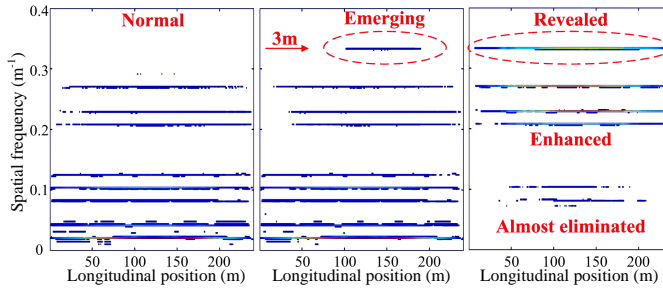


Figure 2.17: Quadratic TFRs of the healthy PCCF (left), the unhealthy PCCF (middle) and the non-CSW residual of unhealthy PCCF (right).

unhealthy PCCF is mostly eliminated after the extraction. Consequently, the part above 0.2 m^{-1} spatial frequency is largely enhanced, particularly the signal component that indicates the global irregularity as circled by the dashed line. Therefore, the employment of non-CSW residual can certainly be helpful to reveal the submerged components and make the anomalies easier to detect.

2.5. Conclusion

This chapter presents a new signal extraction approach specifically aiming at the dominant signal component, namely the CSW in PCCF generated by the interaction between soft catenary suspension and pantograph. The concept of CSW is described based on a theoretical study on pantograph-catenary interaction. To extract the CSWs automatically, the data-driven EEMD algorithm is employed to decompose the PCCF signal with proper boundary extension. Thereupon, the extraction of CSWs and non-CSW residual is realized by utilizing the property that all the decomposed signal components occupy non-overlapping frequency bands. The preliminary results based on simulation and measurement data indicate that the extraction approach is adaptive to various sources of PCCF with high tolerance against measurement noise and effective preservation of the catenary anomalies. Some potential applications of the extracted CSWs and non-CSW residual of PCCF are also suggested for further developments. As for the real-time application of the extraction approach in an on-board measuring system, assuming the extraction will be performed every 5 spans, which is equivalent to about every 3 s in an operation under 300 km h^{-1} speed, the time duration is more than sufficient for the EEMD-based extraction with 100 ensemble members according to the EEMD implementation on a laptop with 2.4 GHz GPU [33].

In future studies concerning the evaluation of current collection quality, the extraction approach could be a useful substitute for the conventional method that usually performs a filter with cut-off frequency 20Hz on a PCCF signal to obtain the low-frequency component of PCCF. It is more accurate comparing with the partial elimination and preservation of the full frequency band of PCCF. Meanwhile, the non-CSW residual of PCCF can facilitate anomaly detections, especially early-stage anomalies that may be submerged by CSWs.

References

- [1] M. Givoni, *Development and impact of the modern high-speed train: A review*, *Transport reviews* **26**, 593 (2006).
- [2] W. Zhang, Z. Shen, and J. Zeng, *Study on dynamics of coupled systems in high-speed trains*, *Vehicle System Dynamics* **51**, 966 (2013).
- [3] Y. Song, Z. Liu, H. Wang, X. Lu, and J. Zhang, *Nonlinear modelling of high-speed catenary based on analytical expressions of cable and truss elements*, *Vehicle System Dynamics* **53**, 1455 (2015).
- [4] B. Allotta, L. Pugi, and F. Bartolini, *Design and experimental results of an active suspension system for a high-speed pantograph*, *IEEE/ASME Transactions on mechatronics* **13**, 548 (2008).
- [5] *Railway applications—current collection systems—requirements for and validation of measurements of the dynamic interaction between pantograph and overhead contact line*, (2012).
- [6] A. Facchinetti and S. Bruni, *Hardware-in-the-loop hybrid simulation of pantograph–catenary interaction*, *Journal of Sound and Vibration* **331**, 2783 (2012).
- [7] S. M. M. Gazafzudi, A. T. Langerudy, E. F. Fuchs, and K. Al-Haddad, *Power quality issues in railway electrification: A comprehensive perspective*, *IEEE transactions on industrial electronics* **62**, 3081 (2014).
- [8] G. Bucca and A. Collina, *A procedure for the wear prediction of collector strip and contact wire in pantograph–catenary system*, *Wear* **266**, 46 (2009).
- [9] S. P. Jung, Y. G. Kim, J. S. Paik, and T. W. Park, *Estimation of dynamic contact force between a pantograph and catenary using the finite element method*, *Journal of computational and nonlinear dynamics* **7**, 041006 (2012).
- [10] J.-W. Kim, H.-C. Chae, B.-S. Park, S.-Y. Lee, C.-S. Han, and J.-H. Jang, *State sensitivity analysis of the pantograph system for a high-speed rail vehicle considering span length and static uplift force*, *Journal of sound and vibration* **303**, 405 (2007).
- [11] O. Vo Van, J.-P. Massat, C. Laurent, and E. Balmes, *Introduction of variability into pantograph–catenary dynamic simulations*, *Vehicle system dynamics* **52**, 1254 (2014).
- [12] W. Zhang, Y. Liu, and G. Mei, *Evaluation of the coupled dynamical response of a pantograph–catenary system: contact force and stresses*, *vehicle system dynamics* **44**, 645 (2006).
- [13] J. S. Kim, *An experimental study of the dynamic characteristics of the catenary–pantograph interface in high speed trains*, *Journal of Mechanical Science and Technology* **21**, 2108 (2007).

- [14] A. Collina, F. Fossati, M. Papi, and F. Resta, *Impact of overhead line irregularity on current collection and diagnostics based on the measurement of pantograph dynamics*, *Proceedings of the Institution of Mechanical Engineers, Part F: Journal of Rail and Rapid Transit* **221**, 547 (2007).
- [15] S. Kusumi, T. Fukutani, and K. Nezu, *Diagnosis of overhead contact line based on contact force*, *Quarterly Report of RTRI* **47**, 39 (2006).
- [16] I. Aydin, M. Karakose, and E. Akin, *Anomaly detection using a modified kernel-based tracking in the pantograph–catenary system*, *Expert Systems with Applications* **42**, 938 (2015).
- [17] J. Pombo, J. Ambrósio, M. Pereira, F. Rauter, A. Collina, and A. Facchinetti, *Influence of the aerodynamic forces on the pantograph–catenary system for high-speed trains*, *Vehicle System Dynamics* **47**, 1327 (2009).
- [18] B. Peng, X. Wei, B. Deng, H. Chen, Z. Liu, and X. Li, *A sinusoidal frequency modulation fourier transform for radar-based vehicle vibration estimation*, *IEEE Transactions on Instrumentation and Measurement* **63**, 2188 (2014).
- [19] S. Banerjee and M. Mitra, *Application of cross wavelet transform for ecg pattern analysis and classification*, *IEEE Transactions on Instrumentation and Measurement* **63**, 326 (Feb. 2014).
- [20] N. E. Huang, Z. Shen, S. R. Long, M. C. Wu, H. H. Shih, Q. Zheng, N.-C. Yen, C. C. Tung, and H. H. Liu, *The empirical mode decomposition and the hilbert spectrum for nonlinear and non-stationary time series analysis*, *Proceedings of the Royal Society of London. Series A: Mathematical, Physical and Engineering Sciences* **454**, 903 (1998).
- [21] Z. Wu and N. E. Huang, *Ensemble empirical mode decomposition: a noise-assisted data analysis method*, *Advances in Adaptive Data Analysis* **1**, 1 (2009).
- [22] H. Wang, Z. Liu, Y. Song, X. Lu, Z. Han, J. Zhang, and Y. Wang, *Detection of contact wire irregularities using a quadratic time–frequency representation of the pantograph–catenary contact force*, *IEEE Transactions on Instrumentation and Measurement* **65**, 1385 (2016).
- [23] *Railway applications—current collection systems—validation of simulation of the dynamic interaction between pantograph and overhead contact line*, (2018).
- [24] S. Bruni, J. Ambrosio, A. Carnicero, Y. H. Cho, L. Finner, M. Ikeda, S. Y. Kwon, J.-P. Massat, S. Stichel, M. Tur, *et al.*, *The results of the pantograph–catenary interaction benchmark*, *Vehicle System Dynamics* **53**, 412 (2015).
- [25] N. Tsakalozos, K. Drakakis, and S. Rickard, *A formal study of the nonlinearity and consistency of the empirical mode decomposition*, *Signal Processing* **92**, 1961 (2012).

- [26] R. Li and D. He, *Rotational machine health monitoring and fault detection using emd-based acoustic emission feature quantification*, *IEEE Transactions on Instrumentation and Measurement* **61**, 990 (2012).
- [27] P. Flandrin, G. Rilling, and P. Goncalves, *Empirical mode decomposition as a filter bank*, *IEEE signal processing letters* **11**, 112 (2004).
- [28] N. Chatlani and J. J. Soraghan, *Emd-based filtering (emdf) of low-frequency noise for speech enhancement*, *IEEE Transactions on Audio, Speech, and Language Processing* **20**, 1158 (2011).
- [29] F. Bao, X. Wang, Z. Tao, Q. Wang, and S. Du, *Emd-based extraction of modulated cavitation noise*, *Mechanical Systems and Signal Processing* **24**, 2124 (2010).
- [30] A.-O. Boudraa and J.-C. Cexus, *Emd-based signal filtering*, *IEEE transactions on instrumentation and measurement* **56**, 2196 (2007).
- [31] A. Komaty, A.-O. Boudraa, B. Augier, and D. Daré-Emzivat, *Emd-based filtering using similarity measure between probability density functions of imfs*, *IEEE Transactions on Instrumentation and Measurement* **63**, 27 (2013).
- [32] N. E. Huang, *Hilbert-Huang transform and its applications*, Vol. 16 (World Scientific, 2014).
- [33] Y.-H. Wang, C.-H. Yeh, H.-W. V. Young, K. Hu, and M.-T. Lo, *On the computational complexity of the empirical mode decomposition algorithm*, *Physica A: Statistical Mechanics and its Applications* **400**, 159 (2014).

3

Detecting irregularities using pantograph head acceleration

This chapter presents a novel approach to detect catenary local irregularities using pantograph head acceleration measurements. First, a series of experimental inspections is carried out in a section of the Beijing-Guangzhou high-speed line in China. The time intervals between the inspections are shortened from the traditional six months to about 40 days, which enables monitoring the short-term degradation of local irregularities. Then, based on the wavelet packet entropy, an approach is proposed to detect local irregularities with different scales in length. Criteria for identifying and verifying the local irregularities are established based on the gradient and repeatability of entropy from multiple measurements. Results from the experimental inspections show that different scales of local irregularities can be detected by the proposed approach. By using frequent inspections, local irregularities can be effectively verified after about seven inspections. The spatial distribution of local irregularities is found to be closely related to the catenary structure. These findings provide valuable information to deploy the approach for a railway network.

Apart from minor updates, this chapter has been published as: H. Wang, Z. Liu, A. Núñez, and R. Dollevoet, "Entropy-based local irregularity detection for high-speed railway catenaries with frequent inspections", *IEEE Transactions on Instrumentation and Measurement*, 2018, 68(10): 3536-3547.

3.1. Introduction

There are currently over 30 000 kilometers of high-speed railway lines worldwide. Most of the high-speed trains are powered by electricity transmitted from the catenary suspended above the rail. Figure 3.1 shows the basic components of catenary in one span between two masts including the messenger wire, contact wire and dropper. Both ends of the messenger and contact wires in several adjacent spans (an anchoring section) are anchored to keep certain tensions in the wires. The pantograph mounted on the train roof collects electric current when slides through the contact wire. Generally, the contact wire height along the entire line must maintain a good consistency and regularity to ensure the current collection quality. For railway infrastructure management, the irregularity of contact wire is a major issue [1–3]. Contact wire irregularities are unfavorable deviations in the contact wire height (as shown by the dashed lines in Figure 3.1) and thickness, which can affect the dynamic contact with a pantograph in the vertical direction. Because a local irregularity can induce a transient impact when a pantograph passes through, it normally has a short deterioration period and high impact on the catenary condition that can impair the life cycle of catenaries [4, 5]. Thus, local irregularities of contact wire should be timely detected to prevent severe damages to the catenary and pantograph. Due to this particularity, complete or partial wire replacement is usually the only maintenance option in case of damaged or broken contact wires, which costs much time and money, and sometimes interrupts train services.

Condition monitoring is commonly adopted to facilitate the maintenance of catenary [6]. Previous studies developed approaches that vary with the employed measurements to assess the catenary condition based on periodical inspections. The pantograph-catenary contact force (PCCF) is theoretically the preferred parameter to measure [7, 8], since the interaction between catenary and pantograph can be directly reflected by the contact force. However, the general requirement for PCCF measurement [9], in terms of sensor placement, accuracy, validation and so on, are high and expensive to implement. Optionally, the displacement or acceleration of the pantograph, the contact wire or the contact point, can be employed as substitutes [10]. These parameters can be directly measured by displacement and acceleration sensors [11], or indirectly calculated from high-resolution images

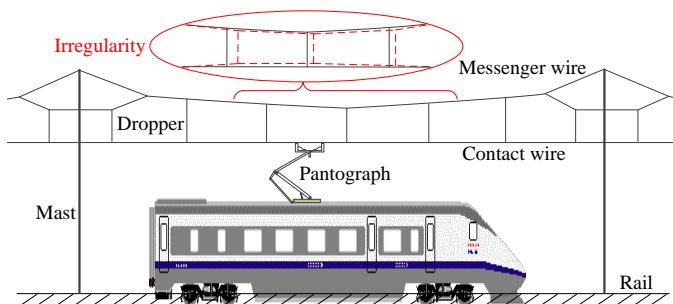


Figure 3.1: Schematics of railway catenary and the irregularity of contact wire (dashed lines).

[12, 13].

Using the aforementioned parameters, some key performance indicators (KPIs) can be computed and then compared with predetermined thresholds for condition assessment. For detecting local irregularities of contact wire specifically, both PCCF and pantograph head (pan-head) acceleration have been employed to establish KPIs. The statistical distribution and kurtosis of PCCF [2], and the root mean square of pan-head acceleration [4] were used for detecting irregularities. Recently, KPIs based on the frequency or wavelength of measurement data have been gaining attention. Frequency-based KPIs can reveal the contact wire irregularities in an early stage before time-domain KPIs could. The quadratic time-frequency representation of PCCF was found to be feasible for detecting contact wire irregularities [14]. But, the localization accuracy for detecting local irregularity was unsatisfactory. Because local irregularities have limited impact on the pantograph-catenary interaction compared with the intrinsic structural parameters of catenary including the anchoring length, span length and interdropper distance [15–17], they are generally not easy to identify from the PCCF or pan-head acceleration. To address this issue, extracting the frequency components attributed to the structural parameters can be a preprocessing step before obtaining KPIs [16].

After the preprocessing, a KPI should be accordingly established for detecting the local irregularities. As introduced above, previously employed KPIs such as kurtosis, root mean square and time-frequency representation can also be applied. However, two main properties make them unfavorable for large-scale applications in practice:

1. Lack of general applicability. These KPIs are developed to focus on certain types of irregularities, while the irregularities actually have different shapes and lengths that induce different responses due to various causes such as wear, incorrect tension of wires, etc.
2. Implementations are not simple enough. There are parameters to be predetermined for previous KPIs, such as the window length of analyzed data, resolution parameters for time-frequency representation, etc. Also, the comparison of KPIs requires prior knowledge on the defect types and the corresponding vibration responses, so that irregularities can be correctly diagnosed.

To detect generic local irregularities using frequency-based KPIs, the indicative frequency range are not constant, because the length or wavelength of local irregularities varies from centimeter [5] to tens of meters [14] attributed to different causes. In such a case, determining the indicative frequencies becomes problematic, since the types and locations of local irregularities existing in a railway line are unknown and changing with time. Therefore, an integrated KPI is proposed in this chapter to circumvent identifying the indicative frequency ranges and also simplify the detection procedure for practice.

Recent studies [5, 18] showed that the wavelet transform is effective for analyzing the local characteristics of pantograph-catenary interaction, because of the

well-proven superiority of wavelet transform for identifying singularity in signal processing [19]. This superiority is rooted in the wavelet basis function that can be scaled and translated in time, while methods such as the Fourier transform and the Hilbert-Huang transform [20] are based on functions with full scale in time. It has been widely used for detecting local features, such as rail defects [21, 22], electrocardiograph anomalies [23] and bearing faults [24]. Based on the component signals decomposed by the wavelet transform, a KPI is often extracted from a component signal (or the corresponding wavelet coefficients) with the indicative frequency range depending on the problem to be solved. To establish an integrated KPI in this chapter, the information contained in all the component signals should be combined together. Thus, the concept of entropy, which is a measure of order or disorder of a dynamic system, can be employed to establish the wavelet entropy [25] as the KPI. The local irregularities induce certain transient disorders in the pantograph-catenary dynamic interaction. Because the wavelet entropy is proven to reflect the degree of order or disorder associated with a multi-frequency signal response [26], it is suitable for analyzing both the PCCF and pan-head acceleration.

Besides the difficulty from the signal processing perspective, another situation that is also not in favor of the local irregularity detection is the periodical inspection for catenaries. Currently, the inspections are carried out annually or semiannually by a dedicated inspection train. However, the time interval between every inspection is too long to monitor the short-term degradation of defects [4]. The results from two successive inspections, when comparing with each other, cannot reflect adequately the evolvement of catenary condition. For high-speed lines, especially lines with high traffic densities, a shorter inspecting period certainly will benefit the detection and prediction of defects causing local irregularities, so that infrastructure managers can control further damages and reduce potential safety threats. Nevertheless, this is on condition that the data measurements and analyses can be timely arranged and implemented.

In this context, a series of experimental inspections was performed on a section of the Beijing-Guangzhou high-speed railway in China, which has an annual passenger demand of over 100 million. The inspections are carried out with a time interval shorter than two months. In this way, the potential to improve the stability and safety of high-speed catenary by timely eliminating or mitigating local irregularities can be explored. Moreover, instead of running at a low speed, the inspections are deliberately carried out at or close to the commercial speed of the railway line. It imitates the operation of commercial trains to examine if future inspections could be performed by commercial trains, so that overnight inspections that are costly and sometimes interfere with regular operation can be circumvented. Also, multiple commercial trains mounted with a measurement system can substantially shorten the inspection interval to cover the entire railway line or network, which is more feasible and economical compared with manufacturing and operating a number of specialized inspection trains.

Using the data measured from the aforementioned experimental inspections, this chapter employs the pan-head acceleration as the source of KPI to detect local irregularities in high-speed railway catenaries. In a previous study [27], the

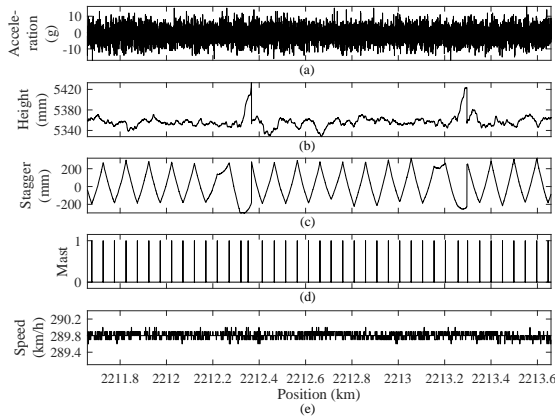


Figure 3.2: A set of inspection data.

motivation, feasibility and preliminary processing technique of using the pan-head acceleration to reduce the system cost and technical difficulty of catenary condition monitoring are presented. This chapter extends those ideas into application and further proposes an approach for catenary local irregularity detection. The rest of the chapter is organized as follows. The data set and data processing techniques employed in the proposed approach are introduced in Section 3.2. Section 3.3 presents an approach for detecting local irregularities with different scales in length. Section 3.4 presents and discusses the detection results obtained from the experimental inspections. Some conclusions and outlooks are given in Section 3.5 toward the implementation of the detection scheme for a network of railway lines.

3.2. Data description and processing

This section first describes the measurement data that are required for the proposed approach, using the data set measured from the experimental inspections as an example. Then, a preprocessing procedure is proposed to extract the essential frequency components contained in pan-head accelerations. Finally, the wavelet packet entropy is introduced for the preprocessed accelerations, which provides KPIs to identify and verify local irregularities later in Section 3.3.

3.2.1. Data description

As the input for the proposed approach, a dedicated inspection or commercial train installed with a pantograph-catenary monitoring system is required. The system should measure parameters concerning the condition of catenary, which are the pan-head acceleration and the height and stagger of contact wire for this approach. Also, a more frequent inspection strategy compared with the previous inspection interval of half a year should be employed. The new interval is preferably less than three months.

In the case of the aforementioned experimental inspections, an integrated on-

Table 3.1: Technical specifications for the parameters measured [28]

Parameter	Measurement range	Accuracy
Pan-head acceleration	0g–100g	1g
Contact wire height	5000 mm–7000 mm	25 mm
Contact wire stagger	–600 mm–600 mm	25 mm
Train speed	0 km/h–500 km/h	0.1 km/h

board measurement system was employed to measure the pan-head vertical acceleration and the height and stagger of contact wire. Simultaneously, the speed and location of the inspection train and the passage of masts between spans are also recorded. The measurements comply with the technical specification enacted by the China Railway Corporation in 2012 [28], in which requirements on the inspection of catenary and pantograph-catenary interaction are put forward. Table 3.1 presents the measurement range and accuracy required for the measured parameters. An example of the measured data set is depicted in Figure 3.2. The sampling rate for all measurements is a fixed spatial interval of 0.25 m. Figure 3.2(a) depicts the vertical acceleration of pan-head in unit of the gravitational acceleration $g \approx 9.81 \text{ m s}^{-2}$. Figure 3.2(b) and (c) depicts the height and stagger of contact wire, respectively. It can be seen that there are two locations with abnormal variations of value at around 2212.4 km and 2213.3 km in the contact wire height and stagger. These types of variation appeared because the inspection train was passing through the overlapping section between two anchoring sections of catenary. In Figure 3.2(d), the indicator of mast passage is shown as a boolean variable with 1 and 0 denoting the occurrence and absence of a mast, respectively. During the measurements, the speed of inspection train was maintained to be approximately constant around 289.8 km/h as shown in Figure 3.2(e). The measurements other than the pan-head acceleration are considered as auxiliaries to support the outcomes from acceleration.

3.2.2. Preprocessing

The pan-head acceleration signal contains essential frequency components, namely the catenary structure wavelengths (CSWs) caused by the cyclic structure of catenary [16]. As has been explained in [27], the identification of the CSWs in pan-head acceleration can be realized based on the ensemble empirical mode decomposition (EEMD) [29]. It can adaptively sift out the CSW regardless of variations in the catenary structure, operation speed and pantograph type. Given an acceleration signal $x(t)$, the EEMD firstly decomposes the signal into several intrinsic mode functions (IMFs) $d_{lj}(t)$, $l = 1, 2, \dots, N$ and a residual $r(t)$ that satisfy

$$x(t) = \sum_{l=1}^N d_l(t) + r(t). \quad (3.1)$$

In [27], the identification of CSWs is realized by eliminating IMFs with frequencies higher than the frequency range of CSWs, based on the power spectrum densities

(PSDs) of the IMFs. To further explore the usage of acceleration signal, this paper utilizes both the CSWs part and non-CSW part of the signal. Concretely, because the CSWs normally range between certain intervals of spatial frequency, the CSWs contained in the original acceleration signal can be separated from the non-CSW signal. This can be done by PSDs of the IMFs with a Boolean variable:

$$\Delta_l = \arg \max_f [P_l(f)] < f_1 \wedge \arg \max_f [P_j(f)] > f_2 \quad (3.2)$$

where $P_l(f)$ is the PSD of the l th IMF $d_l(t)$, $\arg \max_f [P_l(f)]$ denotes the argument of the maximum $P_l(f)$, and f_1 and f_2 are the upper and lower frequency boundaries to identify if a IMF is a CSW, respectively. The common pairs of value for the frequency boundaries are $(0.014 \text{ m}^{-1}, 0.025 \text{ m}^{-1})$ and $(0.1 \text{ m}^{-1}, 0.25 \text{ m}^{-1})$, corresponding to the interdropper distance wavelength and the span wavelength, respectively according to [16]. Using the two pairs of frequency boundary, the CSWs $x_c(t)$ can be obtained by summing the identified IMFs, while the non-CSW residual $x_n(t)$ is the sum of the rest of IMFs and the residual $r(t)$. The two signals satisfy

$$x(t) = x_c(t) + x_n(t) \quad (3.3)$$

Thus, the acceleration signal is essentially decomposed into two signals that are the CSWs and the non-CSW signal after the preprocessing. For example, PSDs of the IMFs decomposed from the acceleration signal in Figure 3.2 are depicted in Figure 3.3(a). Based on (2), the IMFs whose peak of PSD falls within the frequency intervals indicated by the red and blue dashed lines, namely the 4th and 7th IMFs are identified as CSWs. As a result, the CSWs and non-CSW signal of the original acceleration signal are reconstructed as depicted in Figure 3.3(b). Generally, the original signal should not be segmented beforehand to preserve intact the information contained in both reconstructed signals. This also helps to avoid the influence of the end effect of EEMD [29] by minimizing the number of signal ends.

3.2.3. Wavelet packet entropy for CSWs and non-CSW signal

The pan-head acceleration is decomposed into two signals, namely the CSWs and the non-CSW signal after the preprocessing. The CSWs can be regarded as the component resulting from the stiffness variation of contact wire in cycles of span and interdropper distance. Thus, defects with the length or wavelength that is equal or close to span and interdropper distance can be reflected in the CSWs. Meanwhile, other defects that induce different frequency responses are reflected in the non-CSW signal. For both signals, the wavelet packet transform (WPT) [30] is employed for a comprehensive feature extraction. Concretely, taking the CSWs $x_c(t)$ as an example, it can be decomposed into 2^j component signals after j ($j \in \mathbf{N}$) levels of WPT as follows:

$$x_c(t) = \sum_i^{2^j} x_j^i(t) \quad (3.4)$$

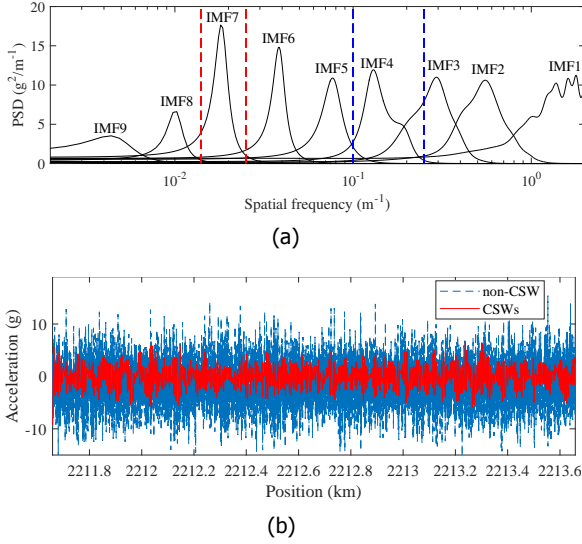


Figure 3.3: (a) PSDs of the IMFs and (b) the corresponding CSWs and non-CSW signal.

Each component signal $x_j^i(t)$ can be expressed as

$$x_j^i(t) = \sum_{k=-\infty}^{\infty} c_{j,\varphi}^i \psi_{j,\varphi}^i(t) \quad (3.5)$$

where $\psi_{j,\varphi}^i(t)$ is a wavelet packet function and integers i , j and φ are the modulation, scale and translation parameter, respectively. The wavelet packet coefficients $c_{j,\varphi}^i$ are obtained from

$$c_{j,\varphi}^i = \int_{-\infty}^{\infty} x_c(t) \psi_{j,\varphi}^i(t) dt. \quad (3.6)$$

Compared with the conventional wavelet transform that only decomposes the low-frequency component of a given signal after the first level, the WPT decomposes signals completely at every level that results in higher resolution in the high-frequency band. This ensures the extraction of high-frequency features that can be attributed to local or short-wavelength excitations, which is important for identifying local defects.

However, the complete decomposition of WPT may excessively divide the frequency band of the original signal into narrow frequency bands. Concretely, a component signal at a low level that contains useful information for irregularity detection can be unfavorably decomposed into two component signals that are lack of physical meanings. This can lead to inaccurate KPIs for further application. To address this issue, a common solution is to find the optimal decomposition tree for the given signal based on the entropy of nodes [31]. Starting from the root node of the full WPT tree, the employed entropy-based criterion computes and compares the entropy of every parent node and the two nodes split from it. To obtain the optimal

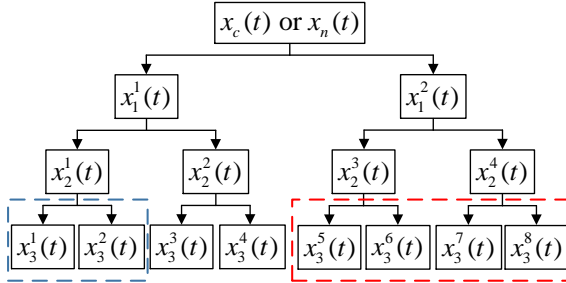


Figure 3.4: Optimal trees determined for the WPT of the CSWs $x_c(t)$ and the non-CSW signal $x_n(t)$. The red and blue dashed lines indicate nodes that are discarded by the entropy-based criterion for $x_c(t)$ and $x_n(t)$, respectively.

tree, a parent node is split only if the sum of the entropy of the two nodes is lower than the entropy of itself. In this way, the given signal has the lowest information cost with WPT based on the optimal tree. Taking the CSWs and non-CSW signal depicted in Figure 3.3(b) as examples, the optimal trees determined from the three-level WPT of both signals are shown in Figure 3.4. This is implemented by using the MATLAB toolbox in [32]. It can be seen that the optimal tree varies with signals. This consequently changes the result of WPT from for example (3.4) to as follows:

$$x_c(t) = \sum_{\{i,j\} \in \mathbf{S}_c} x_j^i(t) \quad (3.7)$$

where \mathbf{S}_c is the set of component signals remained in the optimal tree of the CSWs $x_c(t)$.

The component signals at the terminal nodes of optimal tree contain specific frequency bands decomposed from the original signal. This enables feature extraction at the concerned frequency bands that are related to abnormal excitations. To obtain a KPI that characterizes the features for local irregularity detection, the Tsallis wavelet entropy is employed. The Tsallis entropy is a kind of entropy that measures the disorder of a system. Combining with the signal decomposition results from wavelet transform, it has been applied to the identification of short-duration or transient process in the response of faulty systems [33–35]. In this paper, it is employed as an indicator to integrate the results from WPT. For a set of probabilities $\{p_{i,j}\}$ with $\sum_{\{i,j\} \in \mathbf{S}} p_{i,j} = 1$, the general Tsallis entropy can be defined as

$$S = \frac{1}{q-1} \left(1 - \sum_{\{i,j\} \in \mathbf{S}} (p_{i,j})^q \right), \quad q \in \mathbf{R} \quad (3.8)$$

where q is the non-extensive parameter and in the case of Tsallis wavelet entropy, $p_{i,j}$ is the relative wavelet packet energy of the i th node at the j th level computed by

$$p_{i,j} = \frac{E_{i,j}}{\sum_{\{i,j\} \in \mathbf{S}} E_{i,j}} \quad (3.9)$$

Table 3.2: Typical Catenary Defects and the Resulting Scales of Local Irregularities

Defect type	Scale
Incorrect tension of catenary	Spans
Unrecovered thermal expansion of catenary	Spans
Midpoint anchor misregulation	Tens of meters
Incorrect positioning of overlap	Meters
Inaccurate dropper length or position	Meters
Inaccurate steady arm angle	Meters
Uneven wear	Meters or Centimeters
Hard point	Centimeters

where $E_{i,j}$ is the wavelet packet energy for the i th node at the j th level. For a discrete signal, the computation of $E_{i,j}$ should be done within a time window centered around an arbitrary time instant t_n with

$$E_{i,j}(t_n) = \sum_{t \in T_n} (x_j^i(t))^2 \quad (3.10)$$

where the time window $T_n = \{t : |t - t_n| \leq \frac{L_w}{2}\}$ denotes the set of time instants contained in the window length L_w . This window length determines the length of data on which the Tsallis wavelet entropy is based. It can shift and scale in the time domain in a way serving as a flexible detector for anomaly detection at different scale and location. Thus, the selection of window length becomes crucial for the local irregularity detection as will be presented in the next section.

3.3. Local irregularity detection

The term 'local' is a relative description of irregularity that depends on the total contact wire length corresponding to the data scale. For instance, for the data measured from kilometers of contact wire, the contact wire irregularity with a length of hundreds of meters can thus be regarded as a local one. It means that the local irregularity only occupies a small portion of the total length of contact wire concerned. In this context, the selection of data length to be analyzed becomes crucial for local irregularity detection. It determines the length of local irregularity that can be reflected by the data. Table 3.2 shows several types of typical catenary defect that can lead to different scales of local irregularity. For a long data series from a continuous measurement, the window length selected for local irregularity detection should be varying instead of being fixed, so that different types of local irregularity can be reliably identified. It is also beneficial for recognizing the cause of local irregularities due to the enhanced local information. Therefore, this section presents a varying window strategy for local irregularity detection.

3.3.1. Entropy computation with varying windows

As presented in (3.10), the wavelet packet energy $E_{i,j}(t_n)$ computed in the window length L_w decides on which data scale the Tsallis wavelet entropy in (3.8) is based.

The idea is to employ different window length concerning the scales of defects given in Table 3.2. It can be seen that the scale of local irregularities varies from hundreds of meters (spans) to centimeters. To determine the precise window length to be employed, the actual variation of catenary structural parameter is taken into consideration for two main reasons:

1. The scales of local irregularities are all associated with physical causes that are inaccurate structure configuration or damages attributed to pantograph-catenary interaction. Because the structural parameters of catenary affecting the formation of local irregularities are not strictly consistent along the entire line, these parameter variations should be considered for window length selection.
2. Assuming that a fixed window length $L_w=300$ m, which equals to about six spans, is employed as the window for the scale of spans. When this fixed window slides through the data series measured from a catenary with uneven span lengths, it will cover different combination of spans with both ends of the window shifting erratically in the middle of certain spans. This makes the resulting entropies less comparable with each other, since they are based on vibration responses of pantograph sliding through different local parts of catenary. Therefore, it is preferred to not only use varying window to detect local irregularities with different scales, but also have windows that are adapted to the variation of catenary structural parameter.

Making use of auxiliary measurements, the lengths of every anchoring section, the lengths of every span and an average interdropper distance of five meters in the catenary are employed as the varying window lengths. First, the distance between two adjacent overlapping sections, which can be obtained based on the contact wire height, is regarded as the length of an anchoring section. Using this window length, defects that have a scale of spans such as shown in Table 3.2 could be identified. Second, the distances between two adjacent masts indicated by the Boolean values of masts are regarded as the lengths of spans. Similarly, this window length helps to identify defects that have a scale within one span but longer than five meters such as shown in Table 3.2. Finally, the shortest window of five meters is used to identify other defects with a scale shorter than five meters, which are mostly wear and hard points in the contact wire. As concretely given in Table 3.3, there are two key parameters in (3.10) involved in the varying window strategy. The first one is the window length L_w for entropy computation. The second one is the time instant t_n that decides where the midpoint of window is located. As schematically shown in Figure 3.5, the varying window slides through the signal as the time instant t_n increases in the time domain.

To pair with the aforementioned three scales of window length, three sets of time instant t_n are proposed accordingly. Basically, at each scale, the interval between adjacent time instants should not be longer than half of the window length, so that the full signal length can be entirely covered by the sliding window. This can be done by using the window lengths from the next scale as the intervals between time instants. As given in Table 3.3, for Scale 1, the window lengths are the actual

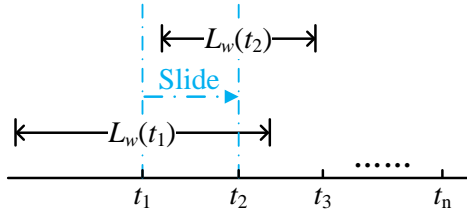


Figure 3.5: Illustration of the varying window with length $L_w(t_n)$ sliding through time instants t_n .

3

Table 3.3: Three Pairs of Scale for Entropy Computation

Scale	Window length $L_w(t_n)$	Time instant t_n
1	Lengths of anchoring sections	Positions of masts
2	Lengths of spans	Every 5 m
3	5 m	Every 0.25 m

lengths of anchoring sections. The corresponding time instants are the positions of masts within every anchoring section, which makes the interval between two adjacent time instants equal to the window length of Scale 2 that is the length of span. Similarly, the time instants of Scale 2 correspond to the window length of Scale 3. Finally, for the shortest window length of Scale 3, the sampling interval of 0.25 m is employed to essentially compute the entropy at every sampling point. In this way, the entropy-based feature extractions can be performed at three scales corresponding to the lengths of anchoring section, span and interdropper distance in descending order. It can not only ensure the complete feature extraction at every scale, but also avoid the extraction of redundant features among different scales. Most importantly, the computed entropy can be associated with certain physical meaning rooting in its spatial position and specific window length.

As introduced in Section 3.2, for subsequent entropy computation, there are two signals, namely the CSWs and the non-CSW signal decomposed by WPT with optimal trees. To apply the varying window strategy to both signals, the physical meanings of both should be taken into consideration. The CSWs signal is by definition associated with the structural parameters of catenary. It contains frequency components that are sensitive to the variation of span and interdropper distance along the catenary. This is in line with the effects of the varying window strategy at Scale 1 and 2, in which the window slides with the interval of span and interdropper distance, respectively, to detect anomalies in the frequency range related to structural parameters. Thus, Scale 1 and 2 should be applied to the CSWs. For the same reason, the non-CSW signal is suitable to be processed by the Scale 3 varying window, to detect anomalies at scales smaller than the main structural parameters. Based on the entropy computed at the three scales, the following presents the criteria for the identification and verification of local irregularities.

3.3.2. Local irregularity identification and verification

In future inspections, if the pan-head acceleration is the sole source of indicator for catenary condition monitoring, it is crucial to establish the baseline and criterion for the diagnosis of acceleration signals. For dynamic measurements such as the pan-head acceleration, the data measured from a single inspection run is considered to be not so reliable in term of repeatability under the interferences of measurement noise and environmental disturbance. This may lead to false indication of defects or overlook of actual defects. With a shortened inspection interval, data from multiple runs can be used for cross comparison to mitigate this effect and thus increase the hit rate, find new defects at early stage and obtain the degradation of different defects.

In practice, the signal baseline for pan-head acceleration is normally measured from the acceptance test of the targeted pantograph-catenary system or early in-situ inspections. It is anticipated that the system performance will decline with the increase of service time, so that infrastructure managers can keep track of the system condition by comparing new data with the baseline. For the experimental inspections in this chapter, there is no historical reference as it is a new attempt of inspection strategy. Thus, the measurement data from the first inspection is regarded as the baseline for this particular case study. It should be noted that all data are measured from an existing line where the presence of local irregularities was expected, even for the first inspection performed among the nine inspections.

To identify local irregularities that cause abnormal transients in the computed entropy, a criterion based on the variation of entropy is employed. For a series of entropy $S(t_n)$ computed by the varying window at any of the three scales, an abnormal transient could be an abrupt rise or fall in the entropy along the time. It can be mathematically described as the gradient of entropy defined as

$$G(t_n) = \frac{|S(t_{n+1}) - S(t_{n-1})|}{t_{n+1} - t_{n-1}} \quad (3.11)$$

Then, to automatically identify and locate the abnormalities in a rather long entropy series computed from kilometers of data, the following criterion is employed:

$$Y(t_n) = \begin{cases} 1, & \text{if } |G(t_n)| > \mu + 3\sigma \\ 0, & \text{otherwise} \end{cases} \quad (3.12)$$

where μ and σ denote the mean and standard deviation of the entropy gradient $G(t_n)$, respectively. $Y(t_n)$ is a Boolean variable with value 1 and 0 denoting if the corresponding entropy value is abnormal or not, respectively.

Although this criterion decides the property of entropy in an absolute sense, it does not indicate necessarily the presence or absence of local irregularity. The identified abnormal entropy can be further verified by comparing with the baseline and historical results measured from the same location. The comparison must be carried out for entropies computed at the same scale. Taking the m th ($m > 1$) measurement in this chapter as an example, its result at Scale k ($k \in \{1, 2, 3\}$) denoted by $Y_{m,k}(t_n)$ can be compared with the result of the earlier ($m - 1$)th measurement

at the same scale $Y_{m-1,k}(t_n)$ as follows:

$$Y_{m,(m-1),k}(t_n) = Y_{m,k}(t_n) \wedge Y_{m-1,k}(t_n) \quad (3.13)$$

where $Y_{m,(m-1),k}$ is the logical conjunction of $Y_{m,k}(t_n)$ and $Y_{m-1,k}(t_n)$. If $Y_{m,(m-1),k}(t_n)$ is 1 (true), it means that the results from the two inspections are consistent, since both results are positive about the presence of local irregularity at the same location. If possible, this can be extended by tracing results back to the earliest inspection where the local irregularity first appeared, so the evolution of irregularity can be observed. For the positive result that cannot find any trace of support from previous inspections, it can be temporarily labelled as a new potential local irregularity, which will be verified when subsequent inspections are performed. It should be noted that the result of a single inspection may generate several false positives and negatives. Thus, it is necessary to trace back more than one inspection when looking for support for a potential local irregularity. Generally, a potential local irregularity can be treated as a verified one when at least three positive results at the same location are successfully identified from the recent six inspections. This is to prevent the waste of maintenance resource on unverified defects. A generalized mathematical expression of the verification can be expressed as

$$Y_{\mathbf{M},k}(t_n) = Y_{m_1,k}(t_n) \wedge Y_{m_2,k}(t_n) \dots \wedge Y_{m_q,k}(t_n) \quad (3.14)$$

where $m_1, m_2, \dots, m_q \in \mathbf{M}$, and \mathbf{M} is the set of measurement number selected for local irregularity verification with $(m_q - m_1) < 6$. For a potential local irregularity at t_n , it is verified only if $Y_{\mathbf{M},k}(t_n) = 1$ and the number of elements in \mathbf{M} is no less than 3.

To sum up, Figure 3.6 shows concisely the proposed approach with the transformation of the m th acceleration signal $x_m(t)$ to the Boolean variable $Y_{m,k}(t_n)$ at Scale k . The acceleration signal is first preprocessed and decomposed into the CSWs $x_c(t)$ and the non-CSW signal $x_n(t)$ by (3.3). At this point, the best trees of both signals based on WPT are obtained and the corresponding component signals at the terminal nodes are determined for entropy computations. Then, the entropy $S_{m,k}(t_n)$ at the three scales with varying windows are computed separately by (3.8). Accordingly, the entropy gradient $G_{m,k}(t_n)$ and the Boolean variable $Y_{m,k}(t_n)$ at the three scales are obtained. Finally, comparisons for verifying the local irregularities can be realized by (3.14). In theory, the proposed approach is simple to implement, because there is no parameter needing to be predetermined and tuned from the preprocessing step to the final verification. The entire process can be computed automatically as long as the input data meet the requirements. Also, the results are simplified to a single KPI that is the criterion value at three scales. This facilitates maintenance decision-making when dealing with a massive amount of data from a railway network.

3.4. Results and discussions

The data set from the experimental inspections are employed to demonstrate the detection performance of the proposed approach. The inspections were carried out

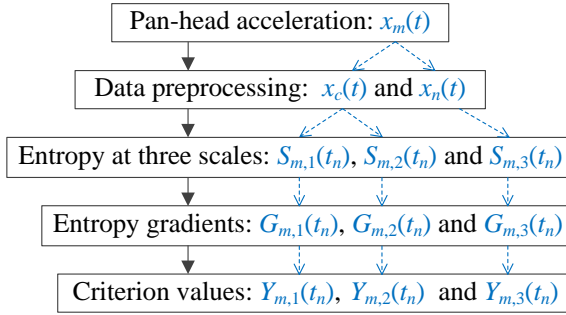


Figure 3.6: Summarized process of the signal transformation in the proposed approach. The dashed lines with arrows indicate the relationships between signals.

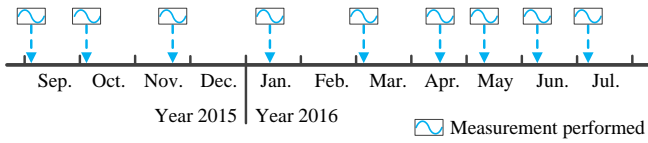


Figure 3.7: Timeline of the experimental inspections.

in a section of railway that is about 34.5 kilometers long from the Beijing-Guangzhou high-speed line starting at 2211.6 km. As depicted in Figure 3.7, nine measurements are performed in the same section with an average interval of 39 days and the maximum less than 2 months. The time intervals are uneven in consideration of minimizing the impact on regular operation. During the nine measurements, a fixed train speed of 290 km/h is consistently used, while the data measured during the acceleration and deceleration of train are omitted. Although the environmental conditions such as the temperature and wind for the nine measurements were different due to the natural change of seasons, the measurement system is considered unaffected, because the system was designed to be functioning under the temperature from $-40\text{ }^{\circ}\text{C}$ to $70\text{ }^{\circ}\text{C}$ in areas below 2500 meters above sea level. Hereafter, the measurements are referred as measurement 1 to 9 in chronological order.

Initially, it was difficult to discover any explicable pattern from the basic statistics of the nine acceleration data series. Figure 3.8 depicts the differences among the nine data series in terms of standard deviation (SD), maximum and minimum, which reflect the degree of oscillation in the pan-head acceleration. The same statistics of the corresponding CSWs and non-CSW signal are also depicted. It can be seen that the SDs of the accelerations fluctuate slightly around 3.7 g for all the nine measurements. The corresponding SDs of the non-CSW signals in blue circles almost overlap with those of the accelerations with smaller values that fluctuate around 3.5 g. This similarity agrees with the case of contact force where likewise the SD of non-CSW signal fluctuates with the SD of force [16]. The maximum and minimum values of the accelerations and the non-CSW signals also show the same similarity. Meanwhile, the CSWs have smaller fluctuations with SDs at around 0.9 g and extrema changing with a different pattern compared with those of the

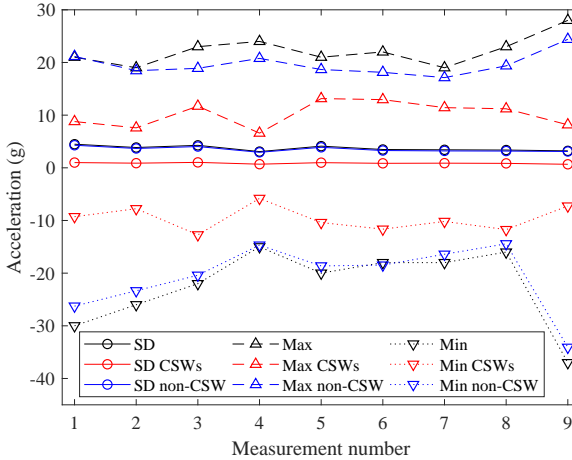


Figure 3.8: Comparisons of the standard deviation (SD), maximum (Max) and minimum (Min) of the pan-head acceleration, the corresponding CSWs and non-CSW signal, respectively, from the nine measurements.

accelerations and the non-CSW signals. In any case, it was not obvious that the acceleration is deteriorating with the increase of operational time. The same can be concluded from the PSDs of the accelerations depicted in Figure 3.9. It can be seen that the level of PSDs was neither growing nor declining consistently with the increase of measurement number. For example, measurements 3 and 4 were performed under similar speed. However, the PSD of acceleration from measurement 3 has the highest level of spectrum density, while the one from measurement 4 has the lowest.

Besides the randomness of pantograph vibration during the nine measurements, part of the reason for these uncertain results are that the indicators are globally computed from the entire data series. This can be improved by using local windows to examine indicators of local data segments. The proposed approach is precisely this type of methodology, but with frequency indicators that helps to identify early-stage irregularities which are hard to detect based on time-domain statistics. The following demonstrates the detection results at the defined three scales separately and together.

3.4.1. Results at each scale

Scale 1

The first scale aims to detect local irregularity with respect to the length of anchoring sections based on the extracted CSWs. The irregularity at this scale indicates that the overall level of contact wire height or elasticity is abnormal, likely due to the incorrect tension or unrecovered thermal expansion of catenary wires. Figure 3.10(a) depicts the entropies computed at Scale 1. It can be seen that each entropy series fluctuates moderately with several notable peaks and troughs as the pantograph runs forward in position. Since the entropies were based on CSWs and

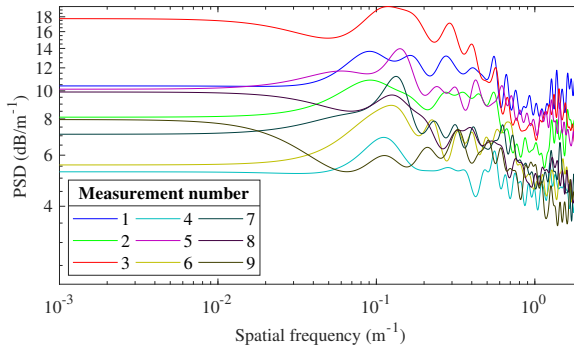


Figure 3.9: Comparisons of the PSD of pan-head acceleration from the nine measurements.

window lengths at Scale 1, the fluctuation could be attributed mostly to the changes of geographic condition along the line and differences in the catenary structure in order to adapt those changes. The entropy gradients depicted in Figure 3.10(b) provide more information on the degree of entropy fluctuations. It becomes relatively clear where the drastic changes happened in the entropies of CSWs. Based on the criterion defined in (3.12), the potential irregularities at Scale 1 from the nine measurements were identified and shown as red dots on the dashed threshold lines. Some locations of the potential irregularities from different measurement were overlapping with each other. According to the principle for local irregularity verification defined with (3.14), the locations of verified local irregularities based on all nine measurements are depicted in Figure 3.11. Four locations with irregularities are verified at Scale 1, because they were identified in at least three out of the nine measurements.

To investigate the results further, Table 3.4 provides the measurements from which the four local irregularities were identified. By referring to the inspection schedule shown in Figure 3.7, it can be inferred that these measurements performed with short intervals are indeed necessary to enable the irregularity detection. If only one or two measurements were performed in the nine-month period as per the traditional inspection interval, it would be unlikely to detect and verify the existence of any of the four irregularities. This deficiency can be largely attributed to the randomness in a single measurement run in terms of vibration, noise and environmental interference that changes with seasons. By having more frequent inspections, the detection results can be verified by historical records, in a way that offsets the influence of randomness in each measurement. This also applies to the cases of Scale 2 and Scale 3 as the criterion for verification is essentially the same.

Scale 2

The second scale is also based on the CSWs, but focus on local irregularities with a shorter length between spans and interdropper distances. The computational process is the same as in Scale 1. Figure 3.12 depicts the locations of verified local irregularities after a certain measurement was performed. Because it takes at least

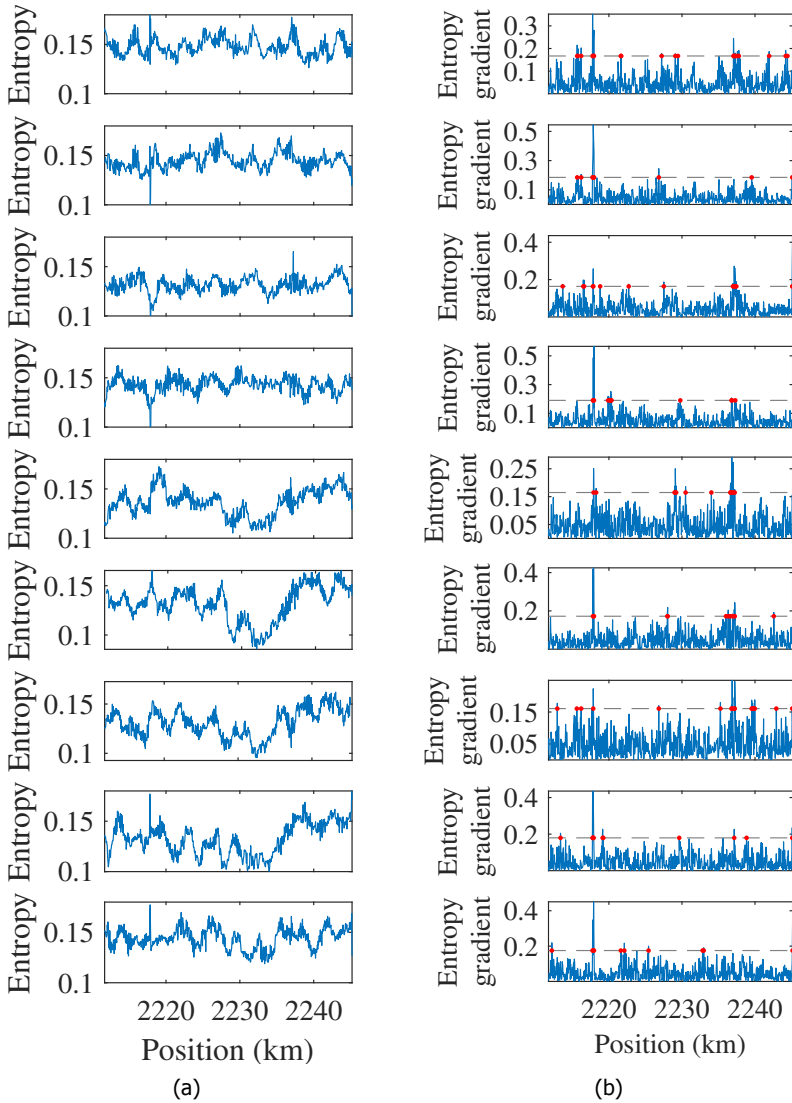


Figure 3.10: (a) Entropies of the accelerations from measurement 1 to 9 (from top to bottom) at Scale 1. (b) The corresponding entropy gradients. The dashed lines depict the thresholds in (3.12) with red dots marking the gradients higher than the thresholds.

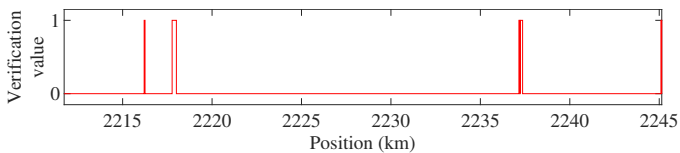


Figure 3.11: Verified local irregularities at Scale 1 based on the nine measurements.

Table 3.4: Numbers of the Measurements that Verify the Four Local Irregularities

Local irregularity	Position (km)	Measurement numbers
1	2216.2	1, 2, 3 and 7
2	2217.8	1, 2, 5, 6, 8 and 9
3	2237.2	1, 3, 6, 7 and 8
4	2245.0	2, 3, 7 and 8

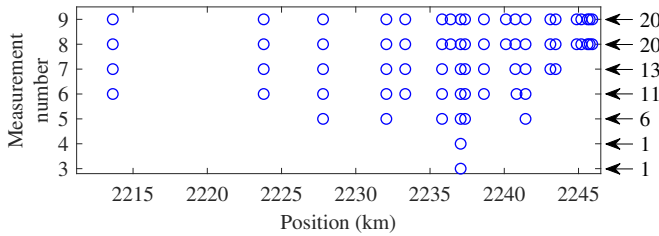


Figure 3.12: Locations of verified local irregularities at Scale 2 corresponding to the number of measurements performed. Arrows on the right indicate the number of verified local irregularities (circles) accumulated after every measurement.

three positive results at the same location to verify a potential local irregularity identified from the first measurement (baseline), the figure presents the verified results starting from measurement 3. It can be seen that only one irregularity was verified successfully after measurements 3 and 4, which indicates that there were local irregularities left undetected in one or two of the earlier measurements. Starting from measurement 5, the number of verified local irregularities increased significantly. By the time of the sixth measurement, which was the last opportunity to verify the results from the first measurement according to (3.14), the number reached 11. At this point, the detection results began with measurement 1 were regarded as finalized. Thus, the newly verified irregularities after measurement 6 can be considered as the ones missing from measurement 1, or emerging ones because the railway line was still operating between the measurements. By the end of the experimental inspections, measurement 9 output the same number of verified local irregularities as that of measurement 8. This indicates that the inspection reached a state where the existing local irregularities were mostly verified, while the emerging ones were still labelled as potential ones from the most recent six measurements.

Figure 3.13 shows the typical evolvement of entropy using two examples in Scale 2. Example 1 is a verified local irregularity that was identified continuously in the first three measurements. This implies that the local irregularity already existed before the first measurement. However, it can be seen that measurements 4 and 8 still failed to detect it later on. On the contrary, Example 2 was verified near the end of the experimental inspections. It was missing in the first three measurements and detected initially in measurement 4. This indicates that it probably appeared later than Example 1 in the catenary. Similarly, it was also missing in later measurements 5 and 6, and then detected in measurements 7 and 8. Both exam-

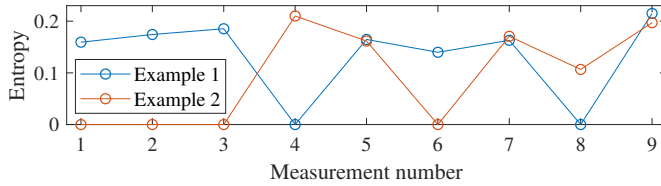


Figure 3.13: Two examples of entropy evolution at Scale 2. Example 1 shows the entropies at the position where the first and only local irregularity is verified after measurement 3. Example 2 shows the entropies at the position where the rightmost local irregularity is newly verified after measurement 8 (see Figure 3.12).

ples reflect the importance and necessity of the verifying procedure and tolerating missing detection in adjacent measurements.

Scale 3

This scale is based on the non-CSW signals to detect short local irregularities using the varying windows with time steps equal to the sampling interval. A single peak in the acceleration could be regarded as a local irregularity caused by the wear or a hard point of contact wire. This adds additional uncertainty to the detection results as it is more dependent on single values of acceleration. Figure 3.14 statistically depicts the verified and potential local irregularities at Scale 3. Similar to Scale 2, the number of verified local irregularities increased from measurement 3 and became almost constant at measurement 9. Compared with the number of potential local irregularities identified at every measurement, it can be seen that it took six or seven measurements for the verified number to approach the potential number. Also, there were small differences between the verified number and the potential number in the latest measurements. This is because there are inevitably false positives in every measurement. Moreover, the number of verified local irregularities accumulated from measurement 1 was higher than the potential number detected from measurement 8 and 9, despite the fact that the potential number from a single measurement has increased slightly over time.

In summary, although local irregularities at the three scales induce different frequency responses in the pan-head acceleration, the same criteria proposed in the approach could still identify and verify them. The repeating entropy peaks from multiple measurements assure the existences of local irregularities and also exclude false alarms that are highly possible from a single measurement as shown by the results above.

3.4.2. Overall results

When comparing the results from different scales with each other, it gives insights into the temporal and spatial distributions of the detected local irregularities. These patterns are important for understanding the differences among the three scales, and thus treating the detection results effectively.

Figure 3.15 depicts the distribution of the number of verified local irregularities from the three scales. It can be seen that the total number increases rapidly start-

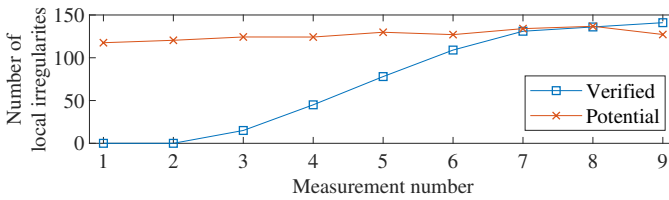


Figure 3.14: Numbers of verified and potential local irregularities at Scale 3 with respect to the measurement number.

ing from measurement 3 and levels off at the end of the inspections. The number from Scale 3 dominates the distribution of total number, because it has by definition the shortest window length to detect small defects. The tendency to grow is also mainly contributed by Scale 3, as the numbers from Scale 1 and Scale 2 became constant before measurement 9. From another perspective, the normalized numbers of every scale is shown referring to the vertical axis on the right. In this way, the slopes of the increasing numbers can be compared. From measurement 4 to 7, the slopes of the three scales are almost parallel to each other, even though the differences in number are huge. This indicates that, with the employed inspection interval, it requires about seven or eight measurements for the inspection to reach a state where most of the existing local irregularities are detected and verified. More importantly, the detection results at this point can be regarded as a new and well-established baseline, which can be utilized to reflect and distinguish the existing and emerging local irregularities. For the scale 3 specifically, one or two more measurements could help to reach this state completely.

Figure 3.16(a) depicts the distribution of verified local irregularities after measurement 9 by position. The positions of anchoring sections are also depicted for comparison. At Scale 1, three out of four local irregularities are located at or near the end of an anchoring section, except for the leftmost one. This indicates a high possibility of defects concerning the configuration of anchoring. At Scale 2, most local irregularities are found at the second half of the entire section, which should be paid more attention to when visiting the field. As for the ones at Scale 3, the distributions are quite dense and sporadic along the entire section. To have a closer look at the distributions, the intervals α and β marked by double-headed arrows, both containing local irregularities from the three scales, are selected. Figure 3.16(b) and 3.16(c) show the enlarged view of both intervals. In interval α , the local irregularity at Scale 2 is located at the position of a mast, while the one in interval β is located in the middle of a span. The causes could be errors in steady arm configuration or midpoint anchor misregulation. In both intervals, the local irregularities at Scale 3 still show signs of randomness, as the defects at this scale, such as contact wire wear and hard point, can also appear at unpredictable positions.

Overall, the resulting distribution of verified local irregularities over time, as an example, shows the expected outcome from frequent inspections after a certain period of time, so that an effective schedule for further actions can be made accordingly. In the case presented, it takes approximately the first seven inspections to find most of the existing irregularities in a railway line and then set a baseline

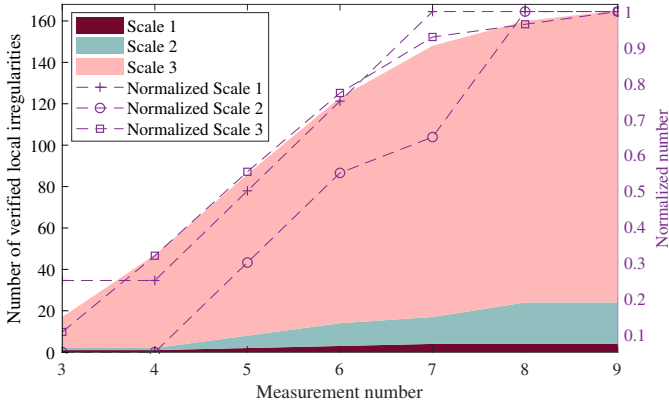


Figure 3.15: The distribution and normalized numbers of verified local irregularities from the three scales with respect to the measurement number.

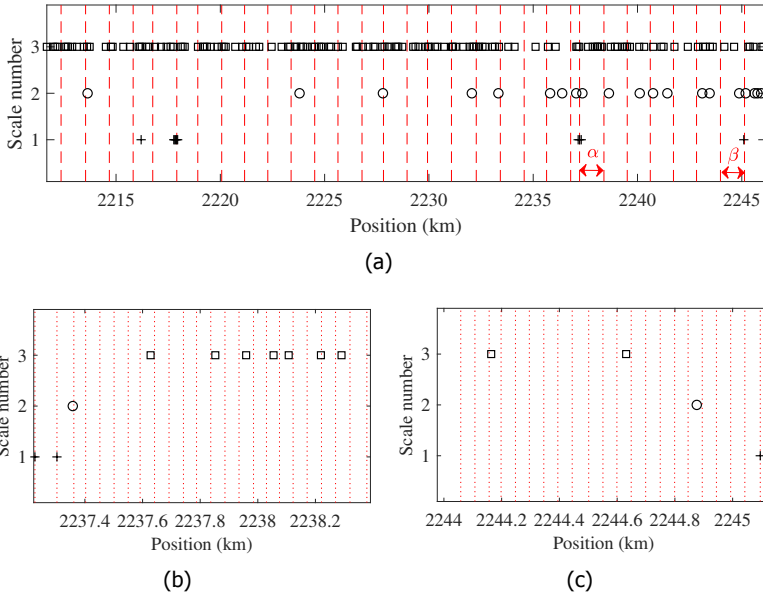


Figure 3.16: (a) Positions of verified local irregularities from the three scales. The dashed lines show the positions of the ends of anchoring sections. (b) and (c) are the enlarged views of the intervals α and β marked in (a), respectively. The dotted lines show the positions of masts.

for detecting emerging irregularities in the future. Meanwhile, the distribution of local irregularities in position has certain tendencies to converge on the structural boundaries of catenary, namely the ends of spans and anchoring sections. For the verified local irregularities at Scale 1 and Scale 2, which are relatively observable and have high impacts on the pantograph-catenary interaction, it is important to set priorities for field visits depending on the density of irregularities.

3.5. Conclusion

This chapter proposed a new scheme for the local irregularity detection of catenary in high-speed railways based on experimental in-situ inspections. The inspections were carried out in a section of a high-speed line with inspection time intervals shortened from the traditional six months to an average of 39 days. This helps to explore and achieve eventually the desired inspection interval of 10 days required by the national standard [28] for high-speed railway catenaries. To achieve accurate detections, a preprocessing step is proposed for the measured pan-head accelerations. The wavelet packet entropy of preprocessed pan-head acceleration is employed as the indicator for identifying and verifying local irregularities with different scales in length. Analyses showed that, based on the repeatability of entropies from multiple measurements, the proposed scheme can detect different scales of local irregularities that exist in a long railway line. It is simple to implement in practice while covering almost all types of local irregularities of catenary. Furthermore, frequent inspections are beneficial to the monitoring of catenary in high-speed lines with emerging needs for condition-based maintenance. The proposed scheme is adapted and suitable for when frequent inspections are implemented in the near future.

To further develop the proposed scheme and make it feasible to cover a network of railway lines, the following can be considered:

1. The actual causes of early-stage local irregularities are not easily observable without performing additional field tests with specialized equipment. This is still an important and ongoing task to relate the detection results with actions that can be taken to facilitate maintenances.
2. Big data analytics can be applied to the massive data accumulated for long-term catenary condition monitoring.
3. The commercial trains performing the inspections and the inspection frequency should be optimized considering the existing timetable of trains and the deterioration rate of catenary in different railway lines.

References

- [1] W. Zhang, G. Mei, X. Wu, and Z. Shen, *Hybrid simulation of dynamics for the pantograph-catenary system*, *Vehicle System Dynamics* **38**, 393 (2002).
- [2] A. Collina, F. Fossati, M. Papi, and F. Resta, *Impact of overhead line irregularity on current collection and diagnostics based on the measurement of pantograph dynamics*, *Proceedings of the Institution of Mechanical Engineers, Part F: Journal of Rail and Rapid Transit* **221**, 547 (2007).
- [3] Z. Liu, Y. Song, Y. Han, H. Wang, J. Zhang, and Z. Han, *Advances of research on high-speed railway catenary*, *Journal of Modern Transportation* , 1 (2016).
- [4] M. Carnevale and A. Collina, *Processing of collector acceleration data for condition-based monitoring of overhead lines*, *Proceedings of the Institution of Mechanical Engineers, Part F: Journal of Rail and Rapid Transit* **230**, 472 (2016).
- [5] H. Wang, A. Núñez, Z. Liu, Y. Song, F. Duan, and R. Dollevoet, *Analysis of the evolution of contact wire wear irregularity in railway catenary based on historical data*, *Vehicle System Dynamics* **56**, 1207 (2018).
- [6] V. J. Hodge, S. O'Keefe, M. Weeks, and A. Moulds, *Wireless sensor networks for condition monitoring in the railway industry: A survey*, *IEEE Transactions on Intelligent Transportation Systems* **16**, 1088 (2015).
- [7] S. Kusumi, T. Fukutani, and K. Nezu, *Diagnosis of overhead contact line based on contact force*, *Quarterly Report of RTRI* **47**, 39 (2006).
- [8] M. Boccione, G. Bucca, A. Collina, and L. Comolli, *Pantograph–catenary monitoring by means of fibre bragg grating sensors: Results from tests in an underground line*, *Mechanical Systems and Signal Processing* **41**, 226 (Dec. 2013).
- [9] *Railway applications—current collection systems—requirements for and validation of measurements of the dynamic interaction between pantograph and overhead contact line*, (2012).
- [10] E. Karakose, M. T. Gencoglu, M. Karakose, I. Aydin, and E. Akin, *A new experimental approach using image processing based tracking for an efficient fault diagnosis in pantograph-catenary systems*, *IEEE Transactions on Industrial Informatics* (Nov. 2016), 10.1109/TII.2016.2628042.
- [11] P. Boffi, G. Cattaneo, L. Amoriello, A. Barberis, G. Bucca, M. F. Boccione, A. Collina, and M. Martinelli, *Optical fiber sensors to measure collector performance in the pantograph-catenary interaction*, *IEEE Sensors Journal* **9**, 635 (2009).
- [12] I. Aydin, M. Karakose, and E. Akin, *Anomaly detection using a modified kernel-based tracking in the pantograph–catenary system*, *Expert Systems with Applications* **42**, 938 (2015).

- [13] D. Zhan, D. Jing, M. Wu, D. Zhang, L. Yu, and T. Chen, *An accurate and efficient vision measurement approach for railway catenary geometry parameters*, *IEEE Transactions on Instrumentation and Measurement* (2018), 10.1109/TIM.2018.2830862.
- [14] H. Wang, Z. Liu, Y. Song, X. Lu, Z. Han, J. Zhang, and Y. Wang, *Detection of contact wire irregularities using a quadratic time–frequency representation of the pantograph–catenary contact force*, *IEEE Transactions on Instrumentation and Measurement* **65**, 1385 (2016).
- [15] J.-W. Kim, H.-C. Chae, B.-S. Park, S.-Y. Lee, C.-S. Han, and J.-H. Jang, *State sensitivity analysis of the pantograph system for a high-speed rail vehicle considering span length and static uplift force*, *Journal of sound and vibration* **303**, 405 (2007).
- [16] Z. Liu, H. Wang, R. Dollevoet, Y. Song, A. Núñez, and J. Zhang, *Ensemble emd-based automatic extraction of the catenary structure wavelength from the pantograph–catenary contact force*, *IEEE Transactions on Instrumentation and Measurement* **65**, 2272 (Jun. 2016).
- [17] D. Song, Y. Jiang, and W. Zhang, *Dynamic performance of a pantograph–catenary system with consideration of the contact surface*, *Proceedings of the Institution of Mechanical Engineers, Part F: Journal of Rail and Rapid Transit* (2016), 10.1177/0954409716664934.
- [18] J. Zhang, W. Liu, and Z. Zhang, *Study on characteristics location of pantograph–catenary contact force signal based on wavelet transform*, *IEEE Transactions on Instrumentation and Measurement* (2018), 10.1109/TIM.2018.2851422.
- [19] S. Mallat and W. L. Hwang, *Singularity detection and processing with wavelets*, *IEEE Transactions on Information Theory* **38**, 617 (Mar. 1992).
- [20] N. E. Huang, Z. Shen, S. R. Long, M. C. Wu, H. H. Shih, Q. Zheng, N.-C. Yen, C. C. Tung, and H. H. Liu, *The empirical mode decomposition and the hilbert spectrum for nonlinear and non-stationary time series analysis*, *Proceedings of the Royal Society of London. Series A: Mathematical, Physical and Engineering Sciences* **454**, 903 (1998).
- [21] Z. Li, M. Molodova, A. Núñez, and R. Dollevoet, *Improvements in axle box acceleration measurements for the detection of light squats in railway infrastructure*, *IEEE Transactions on Industrial Electronics* **62**, 4385 (Jan. 2015).
- [22] M. Molodova, Z. Li, A. Núñez, and R. Dollevoet, *Automatic detection of squats in railway infrastructure*, *IEEE Transactions on Intelligent Transportation Systems* **15**, 1980 (Mar. 2014).
- [23] S. Banerjee and M. Mitra, *Application of cross wavelet transform for ecg pattern analysis and classification*, *IEEE Transactions on Instrumentation and Measurement* **63**, 326 (Feb. 2014).

- [24] E. C. Lau and H. Ngan, *Detection of motor bearing outer raceway defect by wavelet packet transformed motor current signature analysis*, *IEEE Transactions on Instrumentation and Measurement* **59**, 2683 (Oct. 2010).
- [25] S. Blanco, A. Figliola, R. Q. Quiroga, O. Rosso, and E. Serrano, *Time-frequency analysis of electroencephalogram series. iii. wavelet packets and information cost function*, *Physical Review E* **57**, 932 (1998).
- [26] O. A. Rosso, S. Blanco, J. Yordanova, V. Kolev, A. Figliola, M. Schürmann, and E. Başar, *Wavelet entropy: a new tool for analysis of short duration brain electrical signals*, *Journal of Neuroscience Methods* **105**, 65 (2001).
- [27] H. Wang, Z. Liu, A. Núñez, and R. Dollevoet, *Identification of the catenary structure wavelength using pantograph head acceleration measurements*, in *2017 IEEE International Instrumentation and Measurement Technology Conference* (Turin, Italy, May 2017) pp. 453–458.
- [28] *Overall technical specifications of traction power supply safety inspection and monitoring system (6c system) of high-speed railway*, (2012).
- [29] Z. Wu and N. E. Huang, *Ensemble empirical mode decomposition: a noise-assisted data analysis method*, *Advances in Adaptive Data Analysis* **1**, 1 (2009).
- [30] L. Eren and M. J. Devaney, *Bearing damage detection via wavelet packet decomposition of the stator current*, *IEEE Transactions on Instrumentation and Measurement* **53**, 431 (2004).
- [31] R. R. Coifman and M. V. Wickerhauser, *Entropy-based algorithms for best basis selection*, *IEEE Transactions on Information Theory* **38**, 713 (1992).
- [32] M. Misiti, Y. Misiti, G. Oppenheim, and J.-M. Poggi, *Wavelet toolbox*, The MathWorks Inc., Natick, MA **15**, 21 (1996).
- [33] Z. Liu, Z. Han, Y. Zhang, and Q. Zhang, *Multiwavelet packet entropy and its application in transmission line fault recognition and classification*, *IEEE Transactions on Neural Networks and Learning Systems* **25**, 2043 (Nov. 2014).
- [34] W.-X. Ren and Z.-S. Sun, *Structural damage identification by using wavelet entropy*, *Engineering Structures* **30**, 2840 (2008).
- [35] Y. İşler and M. Kuntalp, *Combining classical hrv indices with wavelet entropy measures improves to performance in diagnosing congestive heart failure*, *Computers in Biology and Medicine* **37**, 1502 (2007).

4

Evolution of contact wire irregularities

This chapter studies the evolution of the wear irregularity of contact wire using wire thickness data measured yearly from a section of railway catenary. The power spectral density and time-frequency representation based on the wavelet transform are employed for data analysis, with an emphasis on local wear irregularities that are crucial for contact wire condition assessment. To investigate the cause of wear irregularity evolution and the mutual influence with the pantograph-catenary dynamic interaction, simulations considering the influence of wear irregularity are carried out based on the finite element method. Analyses of the actual wear irregularities and the dynamic contact force under singular and complex wear irregularities are performed. Although the wear irregularity has limited impact on the pantograph-catenary interaction, it can induce the vibration of pantograph and contact wire that will lead to a notable increase of contact force standard deviation. The evolution of wear irregularity is closely associated with the span length and dropper distribution of catenary structure and the running direction of pantograph. In addition, it is found feasible to detect the wear irregularity based on contact force, on condition that the sampling frequency is high enough to reflect the indicative frequencies.

Apart from minor updates, this chapter has been published as: H. Wang, A. Núñez, Z. Liu, Y. Song, F. Duan, R. Dollevoet, "Analysis of the evolution of contact wire wear irregularity in railway catenary based on historical data", *Vehicle System Dynamics*, 2018, 56(8): 1207-1232.

4.1. Introduction

With the massive construction of railway infrastructure and continuous upgrade of high-speed railway lines all over the world, various problems emerge intensively in operation and maintenance. For the power transmission of electrified railway industry, the overhead contact line system, namely the catenary system is the dominantly adopted subsystem. As the train runs through, the pantograph mounted on the train roof collects current from the catenary through the sliding contact with contact wire. During the process, the catenary system suffers impact from the pantograph, leading to the vibration of contact wire and the fluctuation in pantograph-catenary contact force. This brings problems for maintaining the quality of current collection and the stability of train operation. In The Netherlands, more than 327 operation disruptions are recorded as the results of defected catenary since 2011. Among all causes of disruption, the defected catenary usually requires the maximum average duration to recover [1, 2], because of the difficulty of maintenance operation at meters above the ground. Aiming at reducing the amount of disruptions caused by defected catenary and cost saving, researchers and engineers pay more attention on the health condition monitoring of catenary system. In particular, as a major geometric property of the catenary system, the contact wire irregularity (CWI) [3] or unevenness [4] directly affects the sliding contact between the contact strip and the contact wire. So far, the impacts of CWI on the pantograph-catenary interaction still remain ambiguous whether and to what degree it is good or bad for current collection. Moreover, these impacts are likely to be amplified under high speeds, resulting in contact loss, arcing, severe wear, etc. that impair the current collecting quality and the service life of catenary system. Thus, aiming at improving the performance of catenary system, the concept of CWI has been drawn more and more attentions in recent years [3–9].

CWI is the result of all factors that deviates the spatial position of the lower surface of contact wire from the nominal position. Since CWI is mainly caused from the manufacture, installation and wear of the contact wire, it can be regarded as an inevitable existence in any soft catenary system in reality [5]. Some other random environmental factors such as wind, temperature, icing and so on can also cause and change the irregularity under certain circumstances. Generally speaking, the combination of the geometry deformation and the lower surface unevenness of contact wire together constitute the CWI. While the causes of the geometry deformation can be much complex in practice, the causes of the lower surface unevenness mainly include the manufacturing defect, sliding wear and electric corrosion of contact wire [6]. In previous studies, some experiments and simulations are carried out to investigate the influence of CWI on pantograph-catenary interaction [6–9]. However, due to the difficulties in measurement and data analysis, some sporadic conclusions are obtained concerning the local singularity and distributed irregularity of contact wire. Because the local singularity can induce an instantaneous impact on both pantograph and catenary, its acceptable level of amplitude is sensitive to the operation speed and pantograph type [6, 7]. Normally, the requirement will be higher if the operation speed is faster. For the distributed irregularity, the irregularity wavelength is considered to be crucial for the influences on pantograph-catenary

interaction [7, 8]. Instead of treating the CWI as a whole, the geometry deformation and lower surface unevenness can also be studied separately [9] considering their different cause and level of magnitude. But above all, the influence of CWI on pantograph-catenary interaction has not yet been fully revealed. The effects of various irregularities on the pantograph-catenary contact force still requires intensive study to understand if they are actually favorable or unfavorable for current collection. It is the premise for maintenance decision-making so that catenary systems can be maintained under an acceptable condition for long-term normal operations while reducing overall cost.

This chapter focuses on the lower surface unevenness of contact wire, namely the wear irregularity that can be described by the contact wire thickness from in-situ measurements. It not only influences the current collection quality, especially when the train speed is higher than 200 km/h, but also correlates with the life cycle cost of contact wire. It is also believed to be one of the main reasons that cause wire breakages in extreme cases. Normally, if the wire thickness at a certain location is less than a default threshold, the corresponding wire must be replaced partially or integrally depending on the maintenance strategy. The formation of contact wire wear is mainly determined by the material types of contact strip and contact wire, amplitude of contact force, current flow intensity and environmental factors. Accordingly, some methodologies and experiments are carried out to predict the contact wire wear [10, 11], which can provide general predictions of contact wire wear rate under the influence of pantograph passages. To understand how the contact wire wear are formed under electric current, the wear mechanism between contact strip and contact wire are experimentally analyzed in [12–15]. It is believed that the contact temperature induced by sliding friction and arcing determines the wear modes between contact strip and contact wire.

However, in daily operations, the contact wire suffers much complex loads that may be varying with every pantograph passage. For a section of contact wire at a certain location, the pantograph speed, arcing, temperature, wind, rainfall, and in some cases even the pantograph type are all variable factors that change constantly. Moreover, contact wires at various geographical locations face significant climate differences. Thus, the actual wear growth of contact wire is difficult to be fully simulated by mathematical models or experimental setups. But, with the help of historical measurement data, the evolvement of contact wire wear irregularity in term of wire thickness variation can be precisely acquired. Through analyzing and grasping the pattern of wear irregularity in both time and frequency domains, the wear evolvement and the corresponding causes could be objectively observed and potentially explained. This can also be considered as the prior knowledge for the design of prognostics and health management for the catenary system. It provides references to achieve the preventive maintenances depending on prognostics rather than traditional diagnostics, thus leading to lower maintenance costs eventually.

Therefore, this chapter aims to investigate the evolvement of contact wire wear irregularity based on historical data. To comprehensively obtain data features and the evolvement of features over time, the commonly used time-domain statistics including mean, standard deviation and extrema, and the power spectral density

(PSD) estimation are adopted for feature extraction [16–18]. In addition, because the local CWIs possess limited spatial distance along the entire contact wire, they cannot be observed by PSDs in the frequency domain. Thus, the time-frequency analysis with information concerning the spatial position is employed [19, 20]. Techniques such as short-time Fourier transform, quadratic time-frequency distributions and wavelet transform can transform signals into the time-frequency domain. Thus, the frequency deviations or emergences of signal can be observed with knowing the corresponding positions of occurrence. This effect is particularly practical for observing the degradation of local irregularity in both distance and frequency. Meanwhile, the distributed irregularity can also be recognized in the time-frequency domain with long distance intervals. Because the local irregularity of contact wire is important for condition assessment and thus maintenance decision making, the wavelet transform with the superiority in the singularity detection of signals [21] is utilized for the time-frequency analysis in this chapter.

With all the observed evolutionment patterns, their reasons of occurrence still need to be explained and associated with controllable elements in the catenary system. In practice, the direct cause of contact wire wear is undoubtedly the repetitive pantograph-catenary sliding contact. The contact force between pantograph and contact wire is directly proportional to the force of sliding friction. In undesirable cases, it gives rise to arcing if too low or induces severe wear if too high, through which eventually lead to observable wear irregularities along the wire. Therefore, in order to understand the mutual effects of wire wear and pantograph-catenary contact force on each other, it is necessary to employ a numerical model to simulate the pantograph-catenary dynamic interaction under wear irregularities of contact wire. In this way, influences of different degrees of wear irregularity on the current collection quality can be obtained, which can facilitate the decision making of necessary maintenance actions. Moreover, concerning the upgrade of maintenance strategy, the feasibility of using contact force as an indicator for wear irregularity diagnosis [22] or prognosis is investigated as well.

The rest of this chapter firstly analyses the wear irregularity of contact wire from measurements and then studies its mutual influence with the pantograph-catenary interaction through simulations. Concretely, some basic information about the measurement data of contact wire thickness is given in Section 4.2. The adopted PSD estimation and time-frequency analysis methods are introduced in Section 4.3 and applied to the measurement data in Section 4.4. Section 4.5 presents the simulation of pantograph-catenary interaction under the contact wire wear irregularity from measurements. Section 4.6 discusses the evolutionment of wear irregularity combining both measurement and simulation results. Finally, some conclusions are drawn in Section 4.7.

4.2. Measurement data description

The data employed in this chapter are measured from a railway line that operates daily in The Netherlands. For condition-based monitoring of the catenary, the contact wire thickness, with a nominal value of 12 mm is inspected regularly. The spatial positions of sampling points are obtained simultaneously based on the GPS

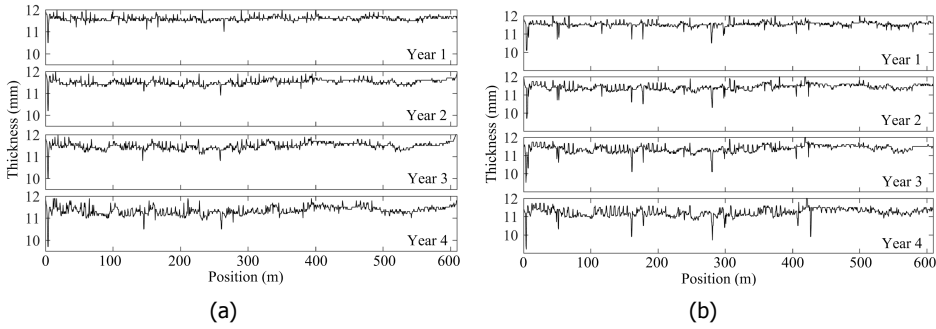


Figure 4.1: A set of contact wire thickness data (year 1 to year 4 from top to bottom). (a) Contact wire average thickness. (b) Contact wire minimum thickness.

device installed on the measurement coach. Since the measurements are carried out on a yearly basis, the evolution of contact wire thickness can be observed corresponding to the same spatial positions. The sampling rate is a fixed interval of 0.5 m. The measured two types of wire thickness are described as follows.

1. Contact wire average thickness that is the average vertical thickness of contact wire profile in every sampling interval.
2. Contact wire minimum thickness that is the minimum vertical thickness of contact wire profile in every sampling interval.

The measurement resolution of wire thicknesses is 0.1 mm, which is equal to the suggested minimum resolution for CWI measurements [4]. Since the wire thickness is measured one year apart and sampled at a fixed interval, it cannot be guaranteed that the sampling point is from precisely the same position for every year. But, to compute the average in a 0.5 m interval should somehow mitigate this minor deviation in position. In cases of severe local wear that could be overlooked by the averaging, the minimum thickness in one interval can preserve their presences, as they are important for deciding if wire replacement or maintenance is required. Therefore, together the minimum and average thicknesses of contact wire can provide a comprehensive view of the growth of contact wire wear.

Figure 4.1 depicts a set of contact thickness data measured at the same section of railway line from year 1 to year 4, during which the contact wire had never been replaced nor maintained. It can be seen that the wear of contact wire is growing yearly, on the basis of the pattern that is already formed in the first measurement of year 1. Also, there is a severely worn sampling point near the beginning of this section of catenary and some others are only observable from the minimum thickness data.

Figure 4.2 depicts the box plots of the two types of thickness with respect to time. According to the box plot of the average thickness data, the contact wire wear, in term of thickness loss, increases slowly by about 0.09 mm per year and becomes more unevenly distributed with the increasing dispersion. The minimum

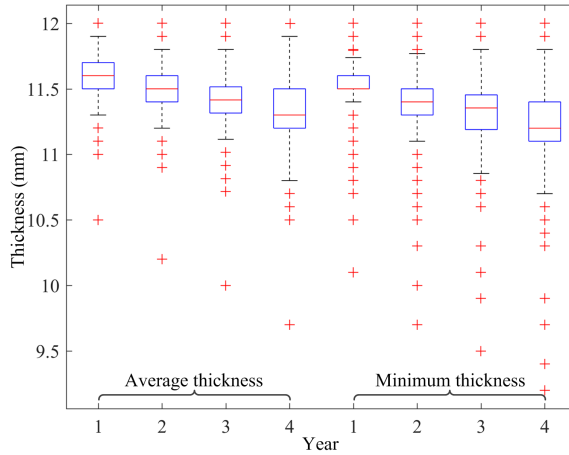


Figure 4.2: Box plot comparisons of evolutions of the average thickness and the minimum thickness.

values of the average thickness, representing the severest worn section of contact wire, have a much more rapid decrease of about 0.27 mm per year. The similar trend can be found from the box plot of the minimum thickness data with smaller overall thickness and rapid decrease in thickness comparing with that of the average thickness. In addition, the outliers in the thickness data marked by the plus signs reflect the existences of some significant local irregularities. As a result, there are more local irregularities revealed by the minimum thickness than by the average thickness for obvious reasons. For a different railway line, the decrease rate of wire thickness varies proportionally with the traffic density of the line considering the number of pantograph passages per unit time.

4.3. Data analysis methods

4.3.1. PSD estimation

To analyze the frequency characteristics of catenary measurement data, the PSD estimation is frequently adopted. It is mainly used for analyzing the dominant frequencies of CWI or contact force [6–9] that are intrinsic and constant depending on the structural parameters of catenary and pantograph. Although these measurement data might not be strictly time-invariant due to the existence of local CWI and other interferences, PSD by its nature can still extract the dominant frequencies while neglecting the time-variant components. Traditional PSD estimation methods are non-parametric and mostly based on the Fourier transform, including the periodogram method and the enhanced periodogram methods such as the Bartlett method and the Welch method [23]. For a discrete stochastic process with N data

samples $\{x(n); n = 1, 2, \dots, N\}$, the Fourier transform of the data set is

$$X(\omega) = \sum_{n=1}^N x(n)e^{-i\omega n}. \quad (4.1)$$

The PSD estimated by the periodogram is

$$P_x(\omega) = \frac{1}{N} |X(\omega)|^2 \quad (4.2)$$

However, even with several enhancements for the periodogram method, the non-parametric methods still suffer from the spectral leakage problem, which is inconvenient for the precise frequency identification of a physical signal. Thus, the parametric methods with high frequency resolution are proposed. One of the well-known representatives is the autoregressive (AR) model estimation method [24]. The data series $x(n)$ can be described by the basic form of AR model

$$x(n) = \sum_{k=1}^p a_k x(n-k) + e_n \quad (4.3)$$

where p is the order of AR model, a_k are the AR coefficients and e_n is a white noise process with zero mean and finite variance σ_e^2 . The estimated PSD based on the AR model is

$$S(\omega) = \frac{\sigma_e^2}{\left| 1 - \sum_{k=1}^p a_k e^{-i\omega k} \right|^2} \quad (4.4)$$

where σ_w^2 and a_k can be calculated by solving the Yule-Walker equations [25].

In the AR model, the determination of order p is crucial for the precise representation of data set $x(n)$. If the order p is too high, the estimated PSD will deviate from the actual PSD and even generate false frequencies. If the order p is too low, some true frequency components may be submerged and become unobservable. To obtain the best order that fits a given data set with minimum information lost, there is one criterion frequently employed, namely the Akaike information criterion (AIC) [24]. It is computed by

$$AIC(p, N) = N \ln \hat{\sigma}^2 + 2p \quad (4.5)$$

where $\hat{\sigma}_i$ is the mean square of residuals defined as

$$\hat{\sigma}^2 = \frac{1}{N} \sum_{i=1}^N \hat{\varepsilon}_i^2 \quad (4.6)$$

and $\hat{\varepsilon}_i$ are the estimated residuals from the fitted model using least squares estimation. The order that results in the minimum criterion value is considered to be

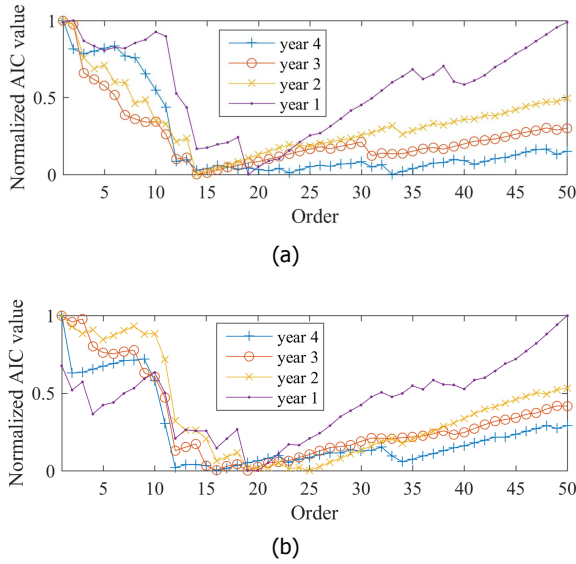


Figure 4.3: Comparisons of the normalized AIC value with respect to the model order for thickness data from different year. (a) Contact wire average thickness. (b) Contact wire minimum thickness.

optimal for the AR model of the data set. To facilitate the comparison of AIC values, the normalized values can be calculated by

$$NAIC(p, N) = \frac{AIC(p, N) - \min(AIC)}{\max(AIC) - \min(AIC)} \quad (4.7)$$

where $\min(\cdot)$ and $\max(\cdot)$ denote the minimum and maximum criterion values among all the model orders under consideration. Taking the data set in Figure 4.1 as an example, Figure 4.3(a) and 4.3(b) depicts the normalized AIC criterion values of the average thickness and the minimum thickness respectively, considering the model order ranges from 1 to 50. It can be seen that the two types of thickness result in different optimal model order that varies from one year to another. Thus, it is necessary to properly determine the model order beforehand to avoid inaccurate PSD estimation. Then, the corresponding PSDs can be obtained by Equation (4.4). Hereafter, the order selection for every data series is realized by comparing the criterion values within orders from 1 to 100 to ensure accurate PSD estimations.

4.3.2. Time-frequency analysis

The time-frequency representation (TFR) of a signal is a three-dimensional representation that describes the energy distribution of the signal in the time-frequency plane. It has been widely used in engineering problems concerning the analysis of signals with varying frequency. In general, if a signal contains transient frequencies or its basic frequencies are changing with time, the time-frequency analysis can

reveal the existence of these time-variant components while the PSD could not. Considering the contact wire wear with local irregularity or singularity caused by a hard point or arcing, the wire thickness data should have varying statistics along the longitudinal direction. This feature accords with the superiority of time-frequency analysis so that it can be fully represented.

Based on the fundamental Fourier transform, the basic time-frequency analysis, namely the short-time Fourier transform can be realized through multiplying the target signal by window functions with short duration before transformation. It utilizes the multiple one-dimensional transformations to constitute a two-dimensional representation. However, the time and frequency resolutions of short-time Fourier transform are constrained by the uncertainty principle as a trade-off between each other. Consequently, the combined time-frequency resolution is limited in the resulting TFR. This becomes especially inconvenient for analyzing the local irregularities in contact wire wear, as the length and position of local irregularity are likely to be distorted by the short-time Fourier transform. Addressing this issue, the TFR based on wavelet transform is frequently employed. Instead of using trigonometric functions as signal basis for signal decomposition, the wavelet transform utilizes the mother wavelet that can shift and scale in time to fit the target signal, particularly for the local variation in signals. Thus, the TFR based on wavelet transform is proven to have a general higher resolution than the short-time Fourier transform. The wavelet coefficients from the data series $x(n)$ decomposed by wavelet transform are defined as [26]

$$W_x(u, s) = \sum_{n=1}^N x(n) \frac{1}{\sqrt{s}} \psi^* \left(\frac{(n-u)\Delta t}{s} \right) \quad (4.8)$$

where Δt is the time interval of data series $x(n)$, $*$ denotes complex conjugate, ψ^* is a family of wavelets deduced from the mother wavelet by translation and scaling operations, u and s are the translation and scale parameters, respectively, and $W_x(u, s)$ are the wavelet coefficients of data series $x(n)$. The corresponding TFR or the so-called scalogram is defined as

$$S_T(f) = |W_x^2(u, s)| \quad (4.9)$$

where $S_T(f)$ is the wavelet-based power spectrum that indicates the frequency response in an interval of time or position T . For consistency, the following TFRs are computed choosing the Morlet function as the mother wavelet for wavelet transform. It should be noted that for both PSD and time-frequency analysis in the following, the mean value of each data series is removed beforehand to cancel its influences on frequency reflection. This is to achieve a better frequency extraction results without the interferences of the overall energy level.

4.4. Data analysis of wear irregularity

If necessary, regular maintenances normally adjust the contact wire height to meet the general requirement of pantograph-catenary contact. Little maintenance can be

done specifically to control the growth of wear irregularity. The wear irregularity of contact wire is constantly evolving with the everyday operation until replacements. As discussed above, the average wear of contact wire is normally growing slower comparing with the local wear with higher thickness loss. However, replacements of contact wire are mostly depending on these thin spots, where wire breakages are likely to happen, regardless of the overall wear rate. Thus, additional attentions are paid to the severe local wear in the data analysis of contact wire wear irregularity. Based on the aforementioned methods, some frequency characteristics of the contact wire wear irregularity can be obtained.

Figure 4.4(a) and 4.4(b) depicts the PSDs of the average thickness and the minimum thickness, respectively. By identifying the minimum criterion value presented in Figure 3, the selected AR model order for the contact wire average thickness from year 1 to year 4 are respectively 19, 14, 14, and 33, and for the minimum thickness from year 1 to year 4 are respectively 19, 20, 19, and 12. For both types of thickness, the overall spectral density is increasing every year with the cumulative thickness loss. The trend and peaks of the PSDs are all similar, but among which the PSDs of the minimum thickness appear to be more smooth and consistent. In particular, there are two frequency peaks standing out and observably raising with the year. As indicated in the figures, for the average thickness and the minimum thickness, the highest peaks are locating at the spatial frequency of 0.178 m^{-1} and 0.172 m^{-1} , respectively. They are equivalent to the wavelength of 5.6 m and 5.8 m, approximatively representing the distance between droppers that are consistently about 5.5 m. This can be considered as the effect of repetitive sliding friction force exerting on the contact wire surface, which is directly proportional to the amplitude of pantograph-catenary contact force. Due to the variation of stiffness along the contact wire attributed to the existence of droppers, the contact force contains the wavelength induced by the placement of droppers [27]. Thus, it introduces the wavelength into the friction force that eventually results in this frequency feature of contact wire wear. Including analyses on other data that are not shown in this chapter, this wavelength is highly consistent and invariable.

From another perspective, Figure 4.5(a) and 4.5(b) depict the TFRs of the average thickness and the minimum thickness based on wavelet transform, respectively. Since the mean of each data series is removed, the overall power in terms of wavelet coefficient for both types of thickness is actually increasing because the yearly growth of thickness loss is uneven. From Figure 4.5(a), it can be seen that the growth of wear irregularity appears mainly in three regions that are circled by dashed lines and numbered as region 1, 2 and 3 in the TFRs. The region 1 is at the beginning of the data interval with a wide frequency range centralized around the spatial frequency 0.17 m^{-1} , which is equivalent to the wavelength of inter-dropper distance. It agrees with the frequency peaks in the PSDs and indicates the severe local wear at the same position as shown in Figure 4.1(a). The region 2 is located at the low-frequency range below 0.02 m^{-1} throughout the entire contact wire. It indicates the increasing overall level of wear irregularity related to the long wavelength of spans. The region 3 indicates emerging frequencies that initially appear in year 1 around 0.034 m^{-1} in spatial frequency, which is about 30 m in wavelength

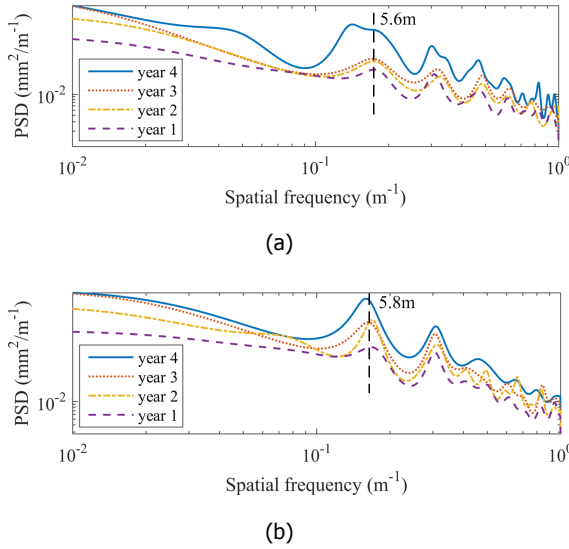


Figure 4.4: Comparisons of PSDs of the thickness data from different year. (a) Contact wire average thickness. (b) Contact wire minimum thickness.

related to half a span or five times of inter-dropper distance. Then, it becomes more severe with time and expands along the contact wire until reaching 380 m in position in year 4. Meanwhile, the same type of severe local wear emerges in year 4 at the same frequency range around 0.17 m^{-1} as the region 1 mentioned before. These emerging local irregularities are reflected more clearly in the TFRs of minimum thickness in Figure 4.5(b). It can be seen that, aside from the region 1, 2 and 3 in the case of average thickness, there are three local irregularities revealed in year 1 and located at around 61 m, 181 m and 298 m in position, respectively. They are marked as region 4, 5 and 6 in Figure 4.5(b). They are constantly growing in power and associated with irregularities that are also growing around 0.034 m^{-1} . In year 3 and 4, another similar local irregularity marked as region 7 appears at around 424 m with the same pattern as the region 4, 5 and 6. The four local irregularities are at a distance of approximate 2 spans, as a result of the high-amplitude contact force around the location where the pantograph passes the contact wire regulated by registration arms.

Combining analyses on both the TFRs of average and minimum thicknesses, it can be found that there is a directional property for the evolvement of contact wire wear irregularity. As the actual running direction of trains is from 0 to 600 m in position, the wear irregularity is increasing in the same direction with the emerging distributed irregularity identified around 0.034 m^{-1} and local irregularities identified around 0.17 m^{-1} . While the location and frequency of these emerging irregularities can be associated with the wavelengths attributed to the catenary structure, this directional property implies that the growth of wear irregularity is also influenced by those pre-existing irregularities, in this case the local wear at the beginning of the

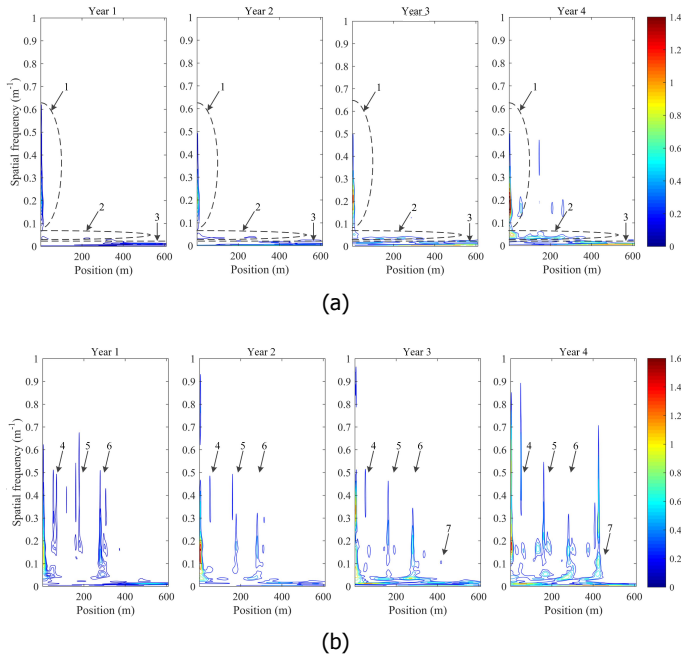


Figure 4.5: Comparisons of TFRs of the thickness data from different years. (a) Contact wire average thickness. (b) Contact wire minimum thickness.

contact wire interval. Therefore, influences of contact wire wear irregularity on the pantograph-catenary interaction can help to explain these patterns of evolvement and facilitate the control of wear irregularity.

4.5. Simulations

4.5.1. Simulation of pantograph-catenary interaction

The simulation technique of pantograph-catenary interaction is well-developed in the past years and comprehensively summarized in [28]. At present, the finite element method (FEM) is the dominant technique in pantograph-catenary dynamic simulation. In this chapter, the pantograph-catenary interaction is modelled by combining the catenary model based on the cable and truss elements and the basic three-lumped-mass model of pantograph [29]. In the catenary model, the contact wire and messenger wire are modelled by nonlinear cable elements, and the droppers are modelled by nonlinear truss elements. First, the initial configuration of catenary model is obtained by the shape-finding method that is verified by several numerical examples. Then, to solve the dynamic response of catenary under a moving load, a structural dynamic equation is formed as

$$\mathbf{M}\Delta\ddot{\mathbf{X}}(t) + \mathbf{C}\Delta\dot{\mathbf{X}}(t) + \mathbf{K}(t)\Delta\mathbf{X}(t) = \Delta\mathbf{F}(x, t) \quad (4.10)$$

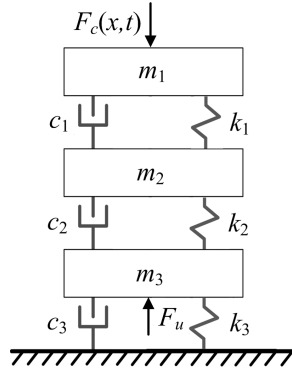


Figure 4.6: The three-lumped-mass model of pantograph.

where $\Delta\ddot{\mathbf{X}}(t)$, $\Delta\dot{\mathbf{X}}(t)$ and $\Delta\mathbf{X}(t)$ are the incremental vectors of the global acceleration, velocity and displacement for the catenary, respectively. \mathbf{M} and \mathbf{C} are the global lumped mass matrix and the global damping matrix, which are considered constant during the simulation. The global stiffness matrix $\mathbf{K}(t)$ of the catenary is formulated through the FEM at time instant t . $\Delta\mathbf{F}(x, t)$ is the incremental vector of the excitation at position x , which includes the PCCF exerted on the contact point and the internal force of catenary structure.

The PCCF is the connection between the catenary model and the three-lumped-mass pantograph model depicted in Figure 6, which is composed of three lumped masses and three spring-damper elements. The dynamic response of pantograph can be described as

$$\begin{cases} m_1\dot{y}_1 + c_1(\dot{y}_1 - \dot{y}_2) + k_1(y_1 - y_2) = -F_c(x, t) \\ m_2\dot{y}_2 + c_1(\dot{y}_2 - \dot{y}_1) + c_2(\dot{y}_2 - \dot{y}_3) + k_1(y_2 - y_1) + k_2(y_2 - y_3) = 0 \\ m_3\dot{y}_3 + c_2(\dot{y}_3 - \dot{y}_2) + c_3\dot{y}_3 + k_2(y_3 - y_2) + k_3y_3 = F_u \end{cases} \quad (4.11)$$

where $F_c(x, t)$ is the dynamic contact force exerting on the pantograph, F_u is the uplifting force of pantograph, and y_1 , y_2 and y_3 are the vertical displacements of the three lumped masses.

Finally, the pantograph-catenary contact force is calculated by the frequently adopted penalty function based on the penetration depth and the contact stiffness K_c between the contact wire and the pantograph as follows:

$$\begin{cases} F_c(x, t) = K_c(u_p(t) - u_c(t))u_p(t) \geq u_c(t) \\ F_c(x, t) = 0u_p(t) < u_c(t) \end{cases} \quad (4.12)$$

where $u_p(t)$ and $u_c(t)$ are vertical positions of the pantograph and the contact wire at the time instant, respectively. During the interaction, the aerodynamic force exerting on the pantograph head is considered based on an empirical equation

$$F_a = 0.00095v^2 + 0.0017v - 0.2 \quad (4.13)$$

where v is the speed of pantograph in the unit ms^{-1} . The total uplifting force of pantograph F_u is the sum of the aerodynamic force F_a and the initial contact

Table 4.1: Selected parameter values for model validation and other related parameters.

Parameter	Value
Contact stiffness (N/m)	For model validation: From 20,000 to 90,000 For further simulations: 50,000
Number of elements between adjacent droppers or dropper and registration point	For model validation: 18 and 36 For further simulations: 24
Sampling interval (m)	For model validation: 0.025 and 0.075 For further simulations: 0.05
Span length (m)	60
Dropper distribution	10 droppers evenly distributed in one span
Contact wire tension (kN)	10
Messenger wire tension (kN)	10.8
Stagger (m)	± 0.2
Operation speed (km/h)	120

force that is 140 N in the case of Dutch conventional lines. The above pantograph-catenary modelling approach has been verified by both the recent benchmark presented in [28] and the EN 50318 standard [30].

The current standard and benchmark specify the validation of pantograph-catenary simulation based on statistics of simulation data at the frequency range below 20 Hz. However, this chapter intends to analyse the information contained in the simulation data at the range above 20 Hz. It is thus necessary to validate the model at a high frequency range. To this end, the model validation is carried out by comparing the mean and PSD of contact forces when the simulation parameters including contact stiffness, element length and sampling time are different. The selected values of the three parameters for model validation are listed in Table 4.1. Some related parameters for the pantograph-catenary dynamic simulations in this chapter are also given. Parameters that are not specified in the table, including those of pantograph and the material properties of contact wire, messenger and dropper, are selected as in the benchmark model in [28] due to the unavailability of these parameters. While this might not be favourable for the simulation results comparing with using real-life parameters, it should be noted that this chapter mainly discusses the relationship between the catenary geometrical shape concerning the clamping points on contact wire and the wear irregularity of contact wire.

For the model validation and further simulations, the catenary model has a unified structure of 14 spans. The dynamic simulation results from the two spans at both ends of the catenary structure are abandoned due to the severe influence of boundary effect. The results for model validation at high frequencies are depicted in Figure 4.7. The mean of contact force that is not low-pass filtered are depicted in Figure 4.7(a), 4.7(b) and 4.7(c), corresponding to the change of the three parameters respectively. It can be seen that the mean contact forces vary slightly with the change of parameters, resulting in a maximum variation of 0.88‰, 0.86‰ and 0.28‰ comparing with the case of the employed values for further simulations.

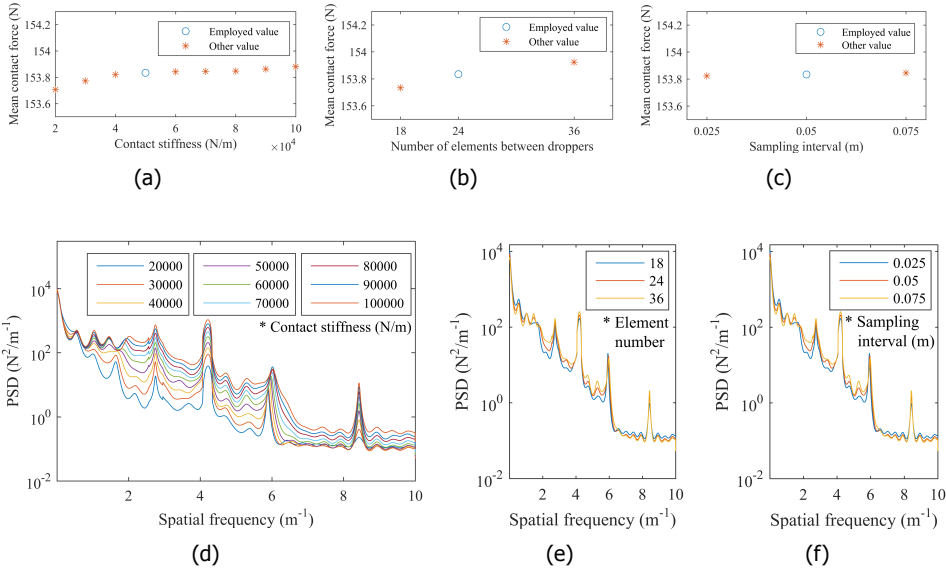


Figure 4.7: Figure 7. Comparisons of mean and PSD of contact force when the (a), (d) contact stiffness, (b), (e) element number and (c), (f) sampling interval are different.

Similarly, comparisons of the PSDs of contact forces are depicted in Figure 4.7(d), 4.7(e) and 4.7(f) corresponding to the change of the three parameters respectively. It can be seen from Figure 4.7(d) that while the spectral density becomes higher with the increase of contact stiffness, the frequency characteristic of contact force remains the same in term of frequency peaks. Meanwhile, the PSDs in the cases element number change and sampling interval change are very similar. For further analysis of simulated contact forces, these consistencies of mean and PSD prove the model validity at high frequencies to a certain extent.

4.5.2. Simulation of contact wire wear irregularity

The wire irregularity caused by geometric deformation that can lead to the variation of contact wire height is often the results of errors in dropper length or placement, wire tension and so on. Thus, it should be considered in the configuration stage of catenary modelling. However, the wear irregularity of contact wire basically differs from the irregularity caused by geometric deformation. Since it is irrespective to the initial configuration of catenary, it can be neglected in the configuration stage. Thus, the wire thickness loss can be simply included in the penalty function in Equation (4.12) as a modification to the penetration depth [9, 31],

$$\begin{cases} F_c(x, t) = K_c(u_p(t) - u_c(t) - z_w(x))u_p(t) - u_c(t) - z_w(x) \geq 0 \\ F_c(x, t) = 0u_p(t) - u_c(t) - z_w(x) < 0 \end{cases} \quad (4.14)$$

where $z_w(x)$ is the contact wire thickness loss at position x .

To simulate the actual growth of contact wire wear irregularity, the average

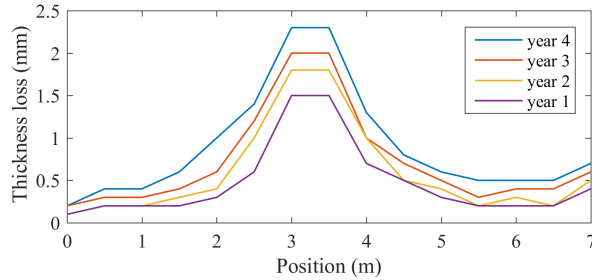


Figure 4.8: Growth of singular local wear irregularity employed in simulations.

4

thickness loss reflected by the data depicted in Figure 4.1(a) is employed. Correspondingly, the mutual influences of wear growth and pantograph-catenary interaction on each other can be investigated. Both local and distributed irregularities are considered for simulation. In the case of local wear irregularity, the severe thickness loss of contact wire located at the beginning of the dataset is selected as the input. As a singular irregularity, it includes the thickness loss with a total contact wire length of 7 m as shown in Figure 4.8. In the interaction model, the thickness loss from each year is equivalently added to the penalty function, simulating the local wire wear locating at the 7th span where the influence of boundary effect is negligible in the 14-span catenary model. For the complex distributed wear irregularity, the entire data series of contact wire thickness loss from year 1 to year 4 are added to the interaction model in the same manner. It simulates a 10-span section of contact wire with actual wear irregularity locating at the middle of the catenary model, i.e. from the 3rd span to the 12th span. Since the sampling interval is set to 0.05 m in simulation, the thickness loss data is interpolated by linear interpolation to form smooth wear irregularities that will be reflected in the contact force.

4.6. Wear irregularity and pantograph-catenary contact force

4.6.1. Influence of singular local wear irregularity

Simulations are carried out with a constant operation speed that is the average commercial speed of 120 km h^{-1} for the pantograph motion. To study the relationship between contact wire wear irregularity and pantograph-catenary interaction, the contact force between pantograph and catenary is selected as the reflection of the interaction. The contact force simulated without intentionally adding wear irregularity to the contact wire is regarded as the reference of normal contact force. Generic technical standards suggest that, before using the contact force to evaluate the pantograph-catenary interaction, the contact force should be filtered by a low-pass filter with 20 Hz cut-off frequency. But, recent advances realized the limitations of this frequency boundary and suggested a boundary up to 200 Hz to preserve useful information in the contact force concerning the condition monitoring of catenary [32, 33]. In the case of contact wire wear, the wavelength of

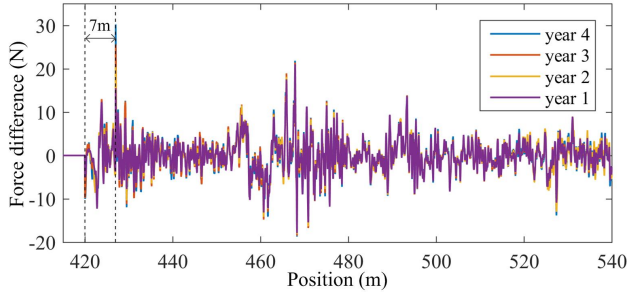


Figure 4.9: Contact force differences under singular local wear irregularity comparing with the reference force.

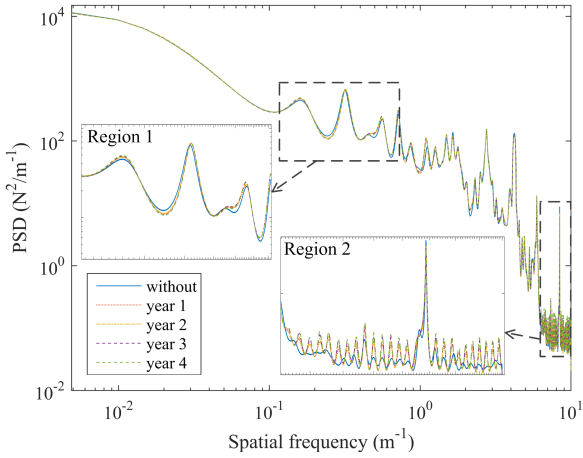
distributed irregularity or the length of local irregularity are likely to be shorter than those of geometric deformation, which consequently requires a high sampling frequency to be observable from measurements. Therefore, the sampling interval in simulations is set to be 0.05 m that is equivalent to over 600 Hz sampling frequency under the 120km/h operation speed, as an attempt to discover new insights in a higher frequency band.

Figure 4.9 depicts the force differences between the contact forces simulated under the growing local wear irregularity described in the previous section and the reference contact force. The location of the local wear irregularity is indicated by the interval between the dashed lines. It can be seen that, starting from the origin of the local irregularity located at 420 m, the contact forces deviate from the reference one due to the influence of the irregularity. The influence continues after the pantograph passed through the irregularity. The overall amplitude of the caused deviation is higher when the irregularity is severer with higher thickness loss every year. As statistically shown in Table 4.2, the thickness losses result in small decreases of the average contact force and increases of standard deviation (SD) in the 2-span duration from 420 m to 540 m. This is because the thickness loss actually reduces the penetration depth as given in Equation (4.14), but also elevates the vibration between the pantograph and contact wire. Meanwhile, the variation in the SD of contact force difference is significantly higher comparing with that of the average contact force difference. Although the variation in this case of singular irregularity only has a small impact on the overall contact force, the impact will be much higher when multiple local irregularities exist and their impacts accumulate to a considerable change of the contact force statistic.

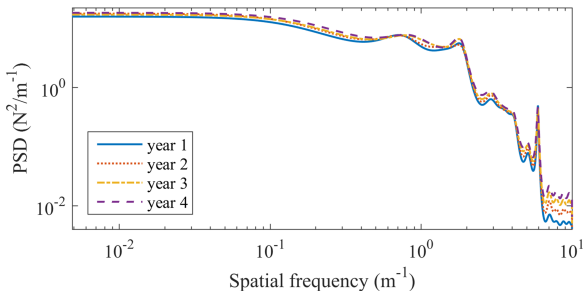
In the frequency domain, it can be seen from Figure 4.10(a) that the PSDs of contact forces under local irregularities have very small variations comparing with the PSD of contact force without irregularity. In the enlarged low-frequency Region 1, the first two frequency peaks respectively locate at around 5.5 m and 3.2 m wavelength, which corresponds to the first two peaks depicted in Figure 4.4 as a result of contact force acting on the contact wire. Although the impact of the singular local wear irregularity is limited, it still slightly increases the energy of the dominant frequency peaks. In the enlarged high-frequency Region 2, the

Table 4.2: Comparisons of the mean and SD of contact forces and contact force differences under singular local wear irregularity.

Condition	Contact force (N)		Contact force difference (N)	
	Mean	SD	Mean	SD
Reference	153.3231	27.1895	0	0
Year 1	153.3222	27.2492	-0.0009	2.6474
Year 2	153.3215	27.2752	-0.0016	2.7735
Year 3	153.3189	27.2944	-0.0043	2.8872
Year 4	153.3135	27.3099	-0.0096	2.9884



(a)



(b)

Figure 4.10: PSD Comparisons of (a) contact forces and (b) contact force differences under local wear irregularities.

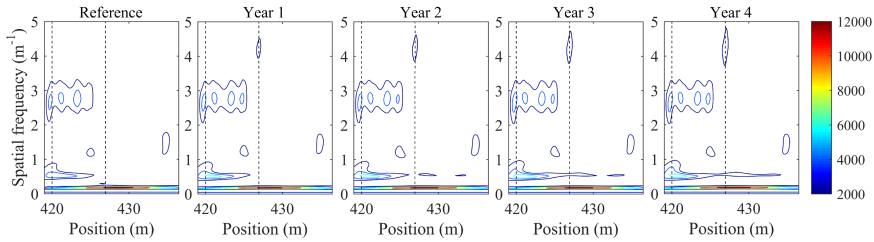


Figure 4.11: TFR Comparisons of contact forces with and without local contact wire wear irregularities.

changes of high-frequency peaks are considerable. It indicates that the singular irregularity induces more intense high-frequency vibration as the irregularity grows. From the PSDs of contact force differences depicted in Figure 4.10(b), influences of the singular irregularity on contact force are easily observable. While the overall level of spectrum is increasing with the yearly irregularity growth, the spectrum difference in the high-frequency range is relatively more significant than that in the low-frequency range. This reflects that the singular irregularity can contribute to the vibration of pantograph-catenary interaction, especially at high-frequency ranges, despite its limited alteration in the penetration depth of contact.

The frequency variation of contact forces along the longitudinal position is depicted in Figure 4.11 with TFRs based on wavelet transform. The interval between the dashed lines indicates the location of the singular irregularity. A narrow position window from 419 m to 436 m near the location of the singular irregularity is used to compute the TFRs. This is to make the small frequency variation caused by the singular irregularity observable. Taking the TFR of normal contact force on the left as the reference, two types of frequency variation can be identified as the impact of the singular irregularity on the contact force. The first one is located at the end of the singular irregularity around 4.4 m^{-1} spatial frequency. It is the reflection of the abnormally high contact force corresponding to the high contact force difference located at the end of the singular irregularity as depicted in Figure 4.9. It also corresponds to the frequency peak of PSDs located at around 4.4 m^{-1} spatial frequency outside the Region 2 depicted in Figure 4.10(a). This emerging frequency can be considered as a new indicator to identify local wear irregularity from the TFR of contact force, but it is only applicable when the measurement frequency for contact force is sufficiently high. The second one is located at around 0.4 m^{-1} where the similar directional property is found in the evolution of contact force as the effect of pantograph passage. In the reference TFR, there is already an energy peak at 420 m that is presumably due to the fixing of registration arm. When the singular irregularity is added, the energy is growing and also expanding in the longitudinal direction, i.e. the running direction of pantograph with the yearly growing irregularity. Since the singular irregularity is only alteration in the simulation, this pattern of change can also be identified as the result of the singular irregularity. Therefore, with multiple local wear irregularities existing along the contact wire, the pattern will aggregate and leading to the formation of contact wire wear with the same directional property as previously discussed.

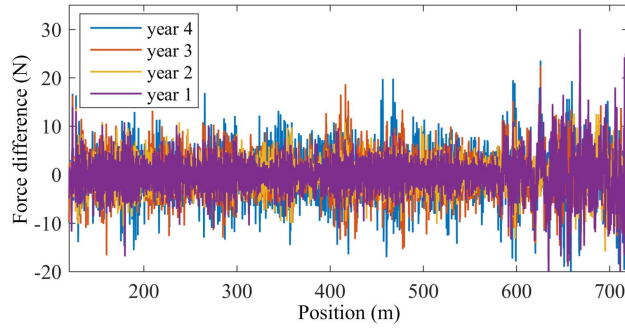


Figure 4.12: Contact force differences under complex distributed wear irregularity comparing with the reference force.

Table 4.3: Comparisons of the mean and SD of contact forces and contact force differences under complex distributed wear irregularity.

Condition	Contact force (N)		Contact force difference (N)	
	Mean	SD	Mean	SD
Reference	153.8336	27.6230	0	0
Year 1	153.7214	29.2038	-0.1122	5.0848
Year 2	153.7056	29.5203	-0.1280	5.6087
Year 3	153.6803	29.7413	-0.1533	6.0639
Year 4	153.6266	29.9924	-0.2070	6.5194

4.6.2. Influence of complex distributed wear irregularity

The added complex wear irregularity is the combination of multiple local and distributed irregularities existed along the 10 spans long catenary in real life. Presumably, it should have a higher impact on the pantograph-catenary interaction than in the case of singular local irregularity. Through simulations according to previous description, the contact force under complex irregularities is acquired and the force differences with the reference contact force are depicted in Figure 4.12. With some exceptional sample points, the force difference is generally higher as the contact wire wear becomes severer. Also, the force variation is abnormally drastic after 600 m due to the boundary effect of simulation model. From the statistics listed in Table 4.3, it can be seen that while the mean of contact force still remains close, the SD of contact force increases significantly by at least 5.7% comparing with the 0.4% when only the singular irregularity is added. For the same cause, the mean and SD of the contact force difference also change considerably.

The impact of complex wear irregularity can also be reflected by the PSD of contact forces. Figure 4.13(a) and 4.13(b) respectively depict the PSDs of the simulated contact forces and contact force differences against the reference. Comparing Figure 4.13(a) with Figure 4.10(a), it can be seen that the spectrum difference caused by the complex irregularity becomes more significant than that of the singular irregularity. Particularly, in the high-frequency range shown in Region 1, the additional spectrum rise and decline caused by the added irregularity indicate that the contact

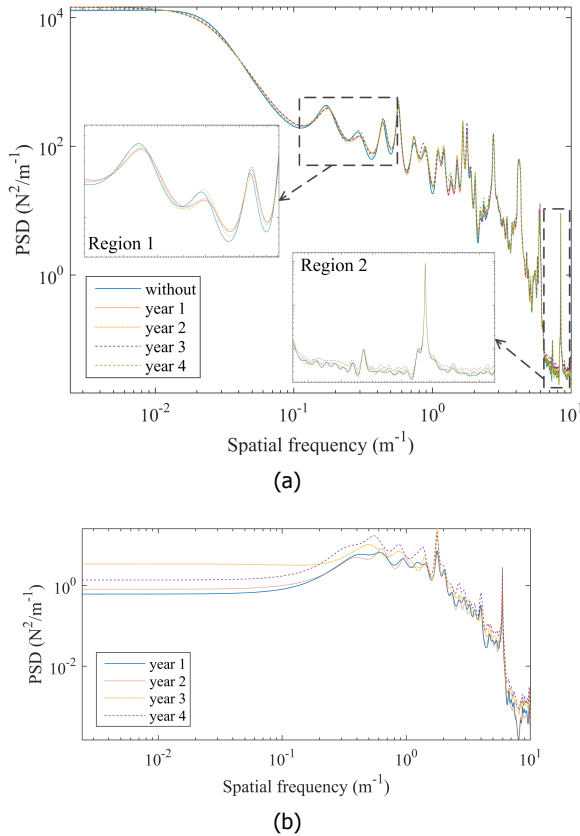


Figure 4.13: PSD comparisons of (a) contact forces and (b) contact force differences under complex wear irregularities.

force fluctuation in the dominant frequency band is influenced by the irregularity. It is mainly because the wear irregularity is the result of actual pantograph-catenary interaction and thus shares the same frequency pattern that is related to the catenary structure, which correspondingly excites the vibration of catenary. The PSDs of contact force differences in Figure 4.13(b) also shows the rise of spectral density is shifting to higher frequencies comparing with those in Figure 4.10(b). However, these changes in PSDs are still small and difficult to be quantified concerning the awareness of the existence of wear irregularities. The results suggest that the PSD of contact force can only reveal limited information on the contact wire wear irregularity, entailing the needs of TFR for the complete characterization, or even the detection and localization of wear irregularity.

The TFR of contact forces from the 10-span catenary can reveal the distribution of frequency variation caused by the complex wear irregularity along the contact wire. Because the impact of wear irregularity compared with the overall contact force is relatively small in amplitude, instead of computing the TFRs of contact

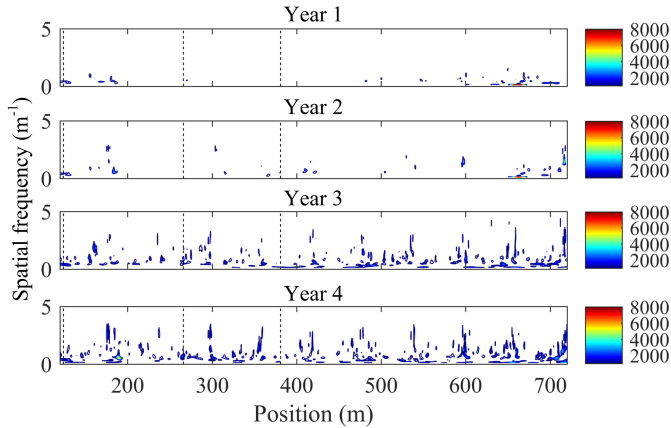


Figure 4.14: TFR comparisons of contact force differences under complex distributed wear irregularities.

force, TFRs of the contact force differences against the reference force are adopted and depicted in Figure 14 for concise comparisons. In each TFR, three vertical dashed lines indicate the middle position of three severely worn wire segments that stand out in the data depicted in Figure 4.1(a), which are located at 3.5 m, 146 m and 261 m, respectively. In the catenary model, the corresponding positions are at 123.5 m, 266 m and 381 m, respectively, with two additional spans at the front. It can be clearly seen that the impact of complex irregularity is increasing with the deterioration of wear irregularity mostly in low frequency range. By the year 3 and 4, there is a periodical pattern showing that the contact force is additionally excited at about every 60 m in higher frequency range, which accelerates the formation of severe local irregularity for contact wire at the registration arm. Meanwhile, in these TFRs with a wide time window, the effects of local irregularities whose position are indicated by dashed lines cannot be fully observed. Only the first and severest one at the beginning shows certain indication of frequency variation at about 0.4 m^{-1} spatial frequency that is in accordance with the variation illustrated in Figure 4.11.

For the thorough observation of local irregularities among the complex irregularity, Figure 4.15 depicts the TFRs of local contact forces around the midpoints of three local irregularities indicated by dashed lines. Impacts of the local irregularities on the contact force shows similar but also different representation due to their distinguishing location in catenary structure and amplitude in thickness loss. From Figure 4.15(a), it can be seen that the first local irregularity, as the severest one, shows very similar representation comparing with when it is solely added in the catenary model as depicted in Figure 4.11. There are emerging frequency components identified around 0.4 m^{-1} and 4.4 m^{-1} , which are expanding with the grow of thickness loss. It is worth noting that in the TFR of reference contact force, there is originally a frequency component around 3 m^{-1} that is caused by the fixing of registration arm at 120 m. For the second and third local irregularities that are not near the fixing points, there is naturally no such kind of interference for irregularity identification. In Figure 4.15(b), the similar frequency variations can be

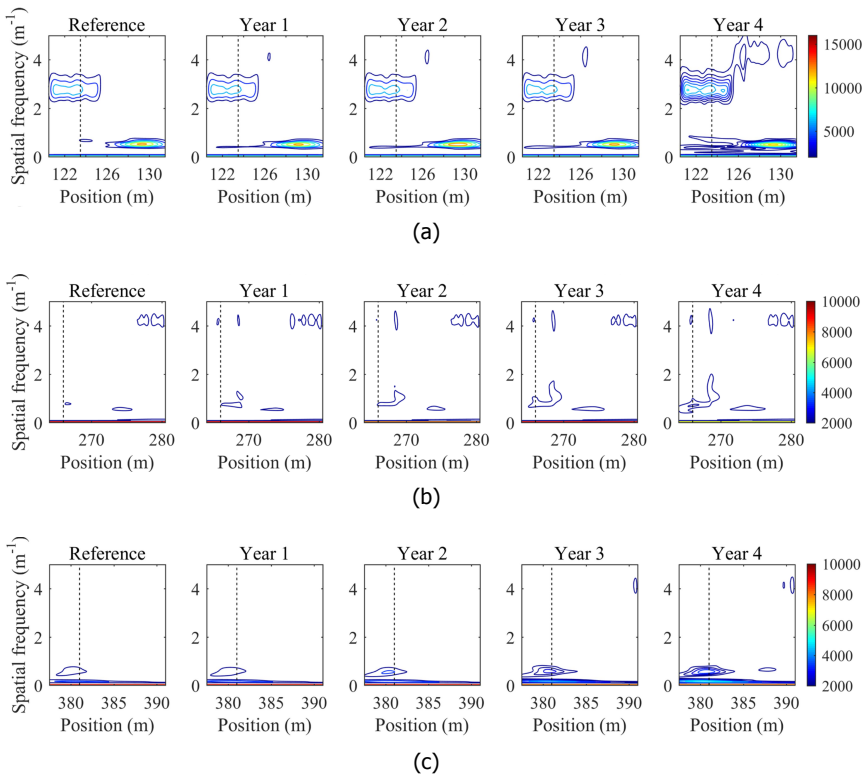


Figure 4.15: TFR comparisons of contact forces around the three local wear irregularities in (a), (b) and (c), respectively.

found near the midpoint of the second irregularity comparing with those caused by the first one in Figure 4.15(a). Meanwhile, Figure 4.15(c) shows that the third one has relatively lower impact on the contact force than the first two with only the frequency variation around 0.4 m^{-1} identified. This is likely the result of a relatively low thickness loss.

From the above analyses on both singular and complex irregularities, it can be speculated that the reflection of local wear irregularities in the contact force requires a high measurement frequency to reveal. In the case of this chapter, the indicative spatial frequency of 4.4 m^{-1} means that a sampling interval shorter than 0.23 m or frequency higher than 147 Hz is necessary.

4.6.3. From contact force to wear irregularity

The pantograph-catenary interaction not only suffers the impact caused by the wear irregularity of contact wire, but also contributes to the formation of the irregularity. The causes of contact wire wear mainly include sliding friction and electric corrosion [10–15]. In this chapter, since the electrical aspect of wear formation is not considered, the growth of wire wear cannot be quantitatively estimated. However,

based on the simulation results of pantograph-catenary contact force, the cause of wear evolution can be qualitatively analyzed, assuming that the friction coefficient is approximately constant. By comparing the simulated contact force and the corresponding wear growth over time, the pattern of wear irregularity evolution can be partly identified and explained according to the variation of contact force simulated from the thickness loss measured in different year.

Concretely, the contact forces simulated under complex distributed wear irregularities in the previous section are adopted as the reflections of contact wire wear. For example, the contact force under the influence of thickness loss measured in year 1 can be associated with the growth of the thickness loss measured in year 2. To this end, the contact force $F_c(x, t)$ is first transformed using the threshold-based criterion as follows:

$$\begin{cases} F_T(x, t) = 1F_c(x, t) \geq \text{mean}[F_c(x, t)] + 3 \cdot \text{std}[F_c(x, t)] \\ F_T(x, t) = 0F_c(x, t) < \text{mean}[F_c(x, t)] + 3 \cdot \text{std}[F_c(x, t)] \end{cases} \quad (4.15)$$

where $\text{mean}[F_c(x, t)]$ and $\text{std}[F_c(x, t)]$ denote the mean and standard deviation of contact force, respectively. The value 1 indicates the existences of abnormally high contact force that can leads to severe wear. Then, the measured minimum thickness of contact wire is employed to show the distribution of wear corresponding to the contact force. The thickness loss $L(x)$ from different year is normalized for comparisons with the transformed contact force:

$$L_N(x) = \frac{L(x) - \min[L(x)]}{\max[L(x)] - \min[L(x)]}. \quad (4.16)$$

The results of the qualitative comparison are depicted in Figure 4.16 by showing the normalized thickness loss from a certain year with the transformed contact force from the previous year. It can be seen that, from year 1 to year 3, most of the sample points of high contact force overlap with or locate close to the locations where severe thickness loss exists in year 2, 3 and 4, respectively. Since the contact force is theoretically proportional to the growth of thickness loss, the wear irregularity of contact wire thus increases year by year because of the abnormal contact forces. Also, the occurrence rate of high contact force, namely the proportion of value 1 in the transformed contact force is 1.4%, 1.7% and 2.1% in year 1, 2 and 3, respectively. It means that the number of local wear irregularity on the contact wire is also increasing with the deterioration of contact force after every year. Meanwhile, some severe thickness loss appear not to be related to the contact force. This can be the results of electric corrosion, especially arcing effects that are not considered in this chapter.

4.7. Conclusion

Making use of the annually recorded contact wire thickness data in past years, this paper presents the analysis of the evolution of contact wire wear irregularity under daily operation. The evolution itself and its influence on pantograph-catenary interaction are studied by the PSD and wavelet transform with the help

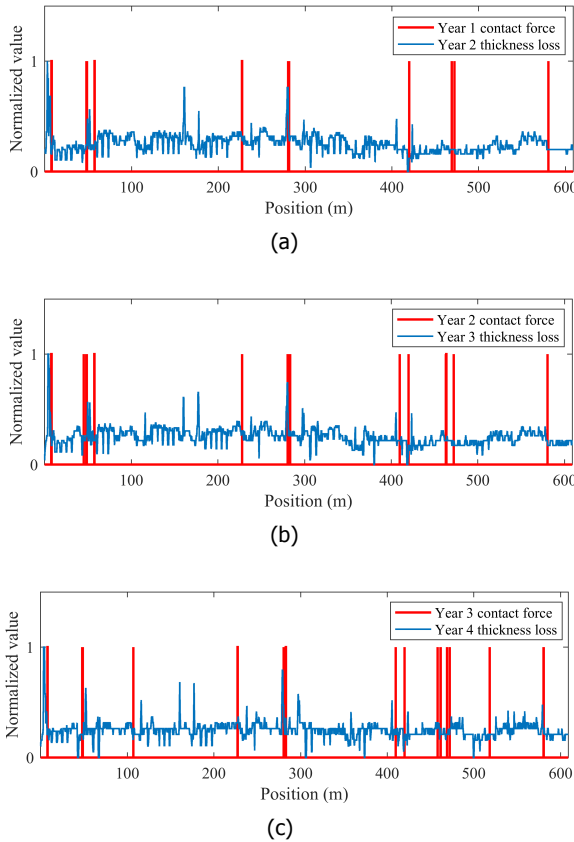


Figure 4.16: Comparisons between transformed contact force and normalized thickness loss. (a) Contact force simulated from year 1 and thickness loss measured in year 2. (b) Contact force simulated from year 2 and thickness loss measured in year 3. (c) Contact force simulated from year 3 and thickness loss measured in year 4.

of FEM model. Based on the measured data from a local section of catenary and tailored pantograph-catenary numerical simulations, the following conclusions can be drawn.

1. The formation of wear irregularity is mainly associated with the catenary structure. Thus, the wear irregularity contains structure wavelengths of catenary such as span and inter-dropper distance. The degree of irregularity in terms of these wavelengths will grow with time as the catenary structure is fixed. The contact wire segment located at the registration arm most likely suffers severe wear due to the high stiffness attributed to the fixing effect.
2. The pattern of wear irregularity has a directional property that is depending on the common or dominant running direction of trains in the specific line. The wear irregularity of contact wire tends to spread toward the running direction

with time. In this sense, the wire wear near the beginning of a tensioning section is generally severer than that near the end of the section.

3. The contact wire wear irregularity has certain impact on pantograph-catenary contact force. While it can hardly influence the mean of pantograph-catenary contact force, it excites the vibration of pantograph and contact wire that results in the increasing SD of contact force, which will eventually exacerbate the degree of wear irregularity.
4. It is possible to detect the contact wire wear irregularity by using the TFR of contact force to identify abnormal frequency peaks. In particular, local irregularities can be detected and localized in a short time window by emerging frequencies related to the local wear pattern and structural vibration frequency. The indicative frequency range is relatively high so that the commonly used upper measurement frequency bound of 20 Hz may be insufficient.

It should be noted that conclusion 3 and 4 concerning the contact force are drawn based on simulation results. They are essentially inferences to be realistically proven in the future based on dynamic measurements. Furthermore, contact wire thickness data from the same railway network with different operation condition and traffic density, or data from a different railway network should be comparatively investigated. Also, it is suggested that the measurement frequency band for whether the contact wire thickness or the contact force (or the pantograph head acceleration) should be expanded to enable the observation of short-wavelength wear irregularity and the corresponding high-frequency vibration response.

References

- [1] O. Cats, M. Yap, and N. van Oort, *Exposing the role of exposure: Public transport network risk analysis*, *Transportation Research Part A: Policy and Practice* **88**, 1 (2016).
- [2] Y. Zhu and R. Goverde, *System-based vulnerability measures for railway systems*, in *Proceedings of the 7th International Conference on Railway Operations Modelling and Analysis (IAROR): RailLille* (2017).
- [3] W. Zhang, G. Mei, and J. Zeng, *A study of pantograph/catenary system dynamics with influence of presag and irregularity of contact wire*, *Vehicle system dynamics* **37**, 593 (2002).
- [4] S. Nagasaka and M. Aboshi, *Measurement and estimation of contact wire unevenness*, *Quarterly Report of RTRI* **45**, 86 (2004).
- [5] W. Zhang, Z. Shen, and J. Zeng, *Study on dynamics of coupled systems in high-speed trains*, *Vehicle System Dynamics* **51**, 966 (2013).
- [6] A. Collina, F. Fossati, M. Papi, and F. Resta, *Impact of overhead line irregularity on current collection and diagnostics based on the measurement of pantograph dynamics*, *Proceedings of the Institution of Mechanical Engineers, Part F: Journal of Rail and Rapid Transit* **221**, 547 (2007).
- [7] W. Zhang, G. Mei, X. Wu, and Z. Shen, *Hybrid simulation of dynamics for the pantograph-catenary system*, *Vehicle System Dynamics* **38**, 393 (2002).
- [8] H. Wang, Z. Liu, Y. Song, X. Lu, Z. Han, J. Zhang, and Y. Wang, *Detection of contact wire irregularities using a quadratic time–frequency representation of the pantograph–catenary contact force*, *IEEE Transactions on Instrumentation and Measurement* **65**, 1385 (2016).
- [9] O. Vo Van, J.-P. Massat, C. Laurent, and E. Balmes, *Introduction of variability into pantograph–catenary dynamic simulations*, *Vehicle system dynamics* **52**, 1254 (2014).
- [10] A. Collina, S. Melzi, and A. Facchinetti, *On the prediction of wear of contact wire in the lines: a proposed model*, *Vehicle system dynamics* **37**, 579 (2002).
- [11] G. Bucca and A. Collina, *A procedure for the wear prediction of collector strip and contact wire in pantograph–catenary system*, *Wear* **266**, 46 (2009).
- [12] C. YAMASHITA and A. SUGAHARA, *Wear modes of contact wire and contact strip under electric current condition*, *Quarterly Report of RTRI* **55**, 67 (2014).
- [13] H. Nagasawa and K. Kato, *Wear mechanism of copper alloy wire sliding against iron-base strip under electric current*, *Wear* **216**, 179 (1998).
- [14] H. Zhao, G. Barber, and J. Liu, *Friction and wear in high speed sliding with and without electrical current*, *Wear* **249**, 409 (2001).

- [15] T. Ding, G. Chen, J. Bu, and W. Zhang, *Effect of temperature and arc discharge on friction and wear behaviours of carbon strip/copper contact wire in pantograph–catenary systems*, *Wear* **271**, 1629 (2011).
- [16] J.-W. Kim, H.-C. Chae, B.-S. Park, S.-Y. Lee, C.-S. Han, and J.-H. Jang, *State sensitivity analysis of the pantograph system for a high-speed rail vehicle considering span length and static uplift force*, *Journal of sound and vibration* **303**, 405 (2007).
- [17] W. Zhang, Y. Liu, and G. Mei, *Evaluation of the coupled dynamical response of a pantograph–catenary system: contact force and stresses*, *vehicle system dynamics* **44**, 645 (2006).
- [18] P. N avik, A. R onnquist, and S. Stichel, *The use of dynamic response to evaluate and improve the optimization of existing soft railway catenary systems for higher speeds*, *Proceedings of the Institution of Mechanical Engineers, Part F: Journal of Rail and Rapid Transit* **230**, 1388 (2016).
- [19] A. R onnquist and P. N avik, *Dynamic assessment of existing soft catenary systems using modal analysis to explore higher train velocities: a case study of a norwegian contact line system*, *Vehicle System Dynamics* **53**, 756 (Feb. 2015).
- [20] S. Kudo, S. Honda, and M. Ikeda, *Contact force signal analysis of current collecting with bispectrum and wavelet*, in *Proceedings of the 41st SICE Annual Conference. SICE 2002.*, Vol. 4 (IEEE, 2002) pp. 2478–2482.
- [21] S. Mallat and W. L. Hwang, *Singularity detection and processing with wavelets*, *IEEE Transactions on Information Theory* **38**, 617 (Mar. 1992).
- [22] S. Kusumi, T. Fukutani, and K. Nezu, *Diagnosis of overhead contact line based on contact force*, *Quarterly Report of RTRI* **47**, 39 (2006).
- [23] P. Stoica and R. L. Moses, *Introduction to spectral analysis*, Vol. 1 (Prentice hall Upper Saddle River, NJ, 1997).
- [24] H. Akaike, *Power spectrum estimation through autoregressive model fitting*, *Annals of the institute of Statistical Mathematics* **21**, 407 (1969).
- [25] Y. Sakamoto, M. Ishiguro, and G. Kitagawa, *Akaike information criterion statistics*, Dordrecht, The Netherlands: D. Reidel **81** (1986).
- [26] S. Mallat, *A wavelet tour of signal processing* (Academic press, 1999).
- [27] Z. Liu, H. Wang, R. Dollevoet, Y. Song, A. N u nez, and J. Zhang, *Ensemble emd-based automatic extraction of the catenary structure wavelength from the pantograph–catenary contact force*, *IEEE Transactions on Instrumentation and Measurement* **65**, 2272 (Jun. 2016).
- [28] S. Bruni, J. Ambrosio, A. Carnicero, Y. H. Cho, L. Finner, M. Ikeda, S. Y. Kwon, J.-P. Massat, S. Stichel, M. Tur, et al., *The results of the pantograph–catenary interaction benchmark*, *Vehicle System Dynamics* **53**, 412 (2015).

- [29] Y. Song, Z. Liu, H. Wang, X. Lu, and J. Zhang, *Nonlinear modelling of high-speed catenary based on analytical expressions of cable and truss elements*, *Vehicle System Dynamics* **53**, 1455 (2015).
- [30] *Railway applications—current collection systems—validation of simulation of the dynamic interaction between pantograph and overhead contact line*, (2018).
- [31] D. Song, Y. Jiang, and W. Zhang, *Dynamic performance of a pantograph–catenary system with consideration of the contact surface*, *Proceedings of the Institution of Mechanical Engineers, Part F: Journal of Rail and Rapid Transit* (2016), 10.1177/0954409716664934.
- [32] P. Boffi, G. Cattaneo, L. Amoriello, A. Barberis, G. Bucca, M. F. Bocciolone, A. Collina, and M. Martinelli, *Optical fiber sensors to measure collector performance in the pantograph-catenary interaction*, *IEEE Sensors Journal* **9**, 635 (2009).
- [33] M. Carnevale and A. Collina, *Processing of collector acceleration data for condition-based monitoring of overhead lines*, *Proceedings of the Institution of Mechanical Engineers, Part F: Journal of Rail and Rapid Transit* **230**, 472 (2016).

5

An integral condition assessment approach

This chapter proposes a data-driven approach that uses a Bayesian network (BN) to integrate the inspection data from catenaries into a key performance indicator (KPI). The BN topology is structured based on the physical relationships among data types, including train speed, dynamic stagger and height of the contact wire, pantograph head acceleration, and pantograph-catenary contact force. The tailored performance indicators are individually defined and extracted from the five types of data as the BN input. As the output of the BN, the KPI is defined as the overall condition level of the catenary considering all defects that can be reflected by the data types. Finally, using historical inspection data and maintenance records from a section of the Beijing-Guangzhou high-speed line in China, the BN parameters are estimated to establish a probabilistic relationship between the input and output. An approach that applies the estimated BN to catenary condition monitoring is proposed. Testing of the BN-based approach using new inspection data shows that the output KPI can adequately represent the catenary condition, leading to a nearly 66.2% reduction in the false alarm rate of defect detection compared with current practice. It is also tested that when the input data quality is not ideal, the approach can still work acceptably on noisy data with a signal-to-noise ratio greater than 3 dB or with one type of data missing.

Apart from minor updates, this chapter has been published as: H. Wang, A. Núñez, Z. Liu, D. Zhang, R. Dollevoet, "A Bayesian Network Approach for Condition Monitoring of High-Speed Railway Catenaries", *IEEE Transactions on Intelligent Transportation Systems*, 2019, In press.

5.1. Introduction

Condition monitoring of the railway infrastructure currently plays an important role in railway asset management. It enables condition-based maintenance that can improve the reliability, availability, and safety of the railway infrastructure. In recent years, emerging techniques have been developed for monitoring the conditions of the tracks [1–3], catenaries (overhead lines) [4–6], bridges [7], tunnels [8], etc. These techniques vary with the different demands of the railway networks, which are expanding worldwide [9].

The catenary is a predominant structure used in power transmission of electrified railways. It is normally constructed along the track with a contact wire suspended above so that trains can collect electric current from the catenary using a pantograph. Figure 5.1 shows the basic elements of a catenary and a pantograph mounted on the train roof. While a train is running on the track, the pantograph slides through and presses against the contact wire of the catenary, and thus electric current can flow from the contact wire to the train locomotive through the pantograph. To ensure that the trains have a continuous and stable power supply, it is important to maintain a good current collection quality resulting from the dynamic interaction between the catenary and pantograph [10]. Well-maintained catenaries not only enhance the safety and reliability of train operations but also lead to a reduction in life cycle costs. To this end, technical standards and specifications [11, 12] have been developed in which catenary condition monitoring is an indispensable measure. In China, defective catenaries require an average of more than 2 hours to repair, and up to 64% of these repairs lead to a loss of power for an average duration of 1.3 hours, which interrupts train services.

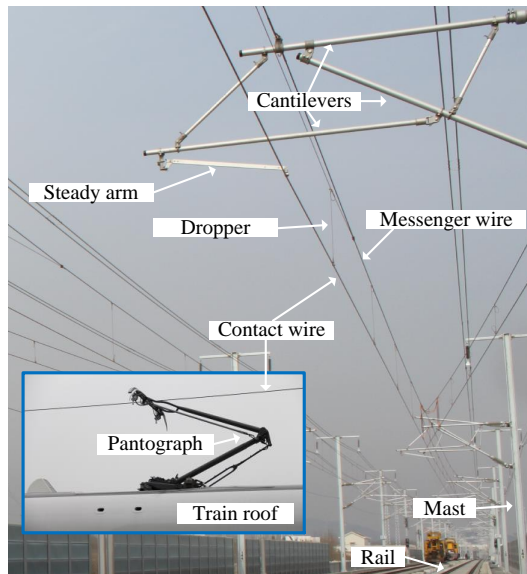


Figure 5.1: Elements of a railway catenary and a pantograph.

As a distributed structure spanning kilometers of distances, condition monitoring of the catenary is commonly performed by specialized inspection trains that run through the catenary such that the entire catenary structure can be covered. Traditionally, condition monitoring is periodically performed to inspect the geometrical parameters of the contact wire, including height, stagger and thickness [13, 14]. This approach is widely applied for conventional lines with an inspection interval between six months and one year. However, the geometrical parameters cannot reflect the dynamic response of the catenary in operation. Thus, dynamic parameters such as the contact force between the pantograph and catenary [4, 10, 15], the acceleration of the pantograph head (collector) [13], the displacement of the contact point [16], and the dynamic height and stagger of the contact wire [17], are becoming preferable in practice [18, 19], especially for high-speed lines. Other components of catenary systems, such as the insulator, isoelectric line, etc., are also monitored [20–22] because they are important to ensure the full functionality of the catenary.

Depending on the measurements applied for condition assessment, the condition of the catenary is commonly quantified by a performance indicator (PI) extracted from measurement data. For geometrical parameters, PIs consist mostly of comparisons with a threshold that is predefined according to nominal values or expert experience. The PIs based on dynamic parameters can be highly diverse because the dynamic responses of the catenary and pantograph, in terms of amplitude and frequency of vibrations, are contained in the measurement data. Therefore, the statistical distribution, kurtosis, power spectrum density and time-frequency representation of the pantograph-catenary contact force (PCCF) were selected as PIs to detect contact wire irregularities attributed to a wide range of catenary defects [10, 23–25]. As a substitute for PCCF, the pantograph head acceleration (PHA) is more cost-efficient to measure. Similarly, PIs such as the root mean square [13] and wavelet entropy [26] of the PHA were also chosen to detect contact wire irregularities. Based on the physical meanings of PIs, the condition of the catenary can be quantified for further assessment and maintenance decision-making.

In recent years, condition monitoring techniques deployed in practice are gradually making greater use of data-driven approaches [27]. For catenary condition monitoring, the types of geometrical and dynamic parameters measured and the increasing frequency of inspections [26] generates a large volume of multivariate data sets. However, approaches that can make full use of these data sets are lacking. In previous studies, PIs were mostly extracted from a single type of parameter. For defect detection of high-speed lines in China, the false alarm rate can reach up to 30.5% based on only one type of catenary data measured from a single inspection run, according to maintenance records. Learning from techniques developed for other applications, such as bearing fault diagnosis [28–30] and rail condition monitoring [31–33], improvements in condition monitoring of the high-speed railway catenary can be realized by the following:

1. Extraction of multiple PIs from one type of parameter;
2. Measurement of multiple parameters to extract and fuse the respective PIs.

This chapter proposes an approach that combines both measures.

As specified in the technical standard for condition monitoring of high-speed railways in China [12], the PCCF, the PHA, and the dynamic height and stagger of the contact wire are simultaneously inspected by specialized measurement trains. Individually, these parameters can reflect the condition of the catenary under dynamic interaction with a pantograph, although from different perspectives, and they are also physically related to each other as the results of pantograph-catenary interaction. Because of the inherent physical relationships, the measurement data of the parameters contain probabilistic correlations in terms of dynamic responses. This feature can be used in enhanced condition monitoring in which the output rarely suffers from disadvantages due to a single type of data, such as measurement errors or missing data.

It is observed in the literature that multiple types of data are simultaneously measured and applied for monitoring the condition of a single system or device. For example, the diagnosis of power systems [34], airplane engines [35] and heat pumps [36] relies on multiple data types as the input. A similarity among these applications and catenary condition monitoring is fusion of multiple data types for assessment of the overall condition of a system. The data can be fused because of the probabilistic correlations between different data types indicating the healthiness of the same system. The Bayesian network (BN) [37], which mathematically represents a set of variables and their probabilistic relationships, can precisely address the data fusion problem described. Multiple PIs, each extracted from the different types of data measured for a catenary, can be fused using a BN to perform comprehensive condition assessment.

This study is an extension of a previous work [38]. In summary, the contributions and extensions of this study include the following:

1. A new BN is structured specifically for condition monitoring of the catenary.
2. Tailored PIs are proposed for different types of catenary inspection data and used as the input of the BN.
3. A data-driven approach using the BN is proposed to supply a comprehensive assessment of the catenary condition based on inspection data.

The remainder of this chapter is organized as follows. Section 5.2 introduces the basic theory of BN. Section 5.3 proposes a BN for catenary condition assessment. Based on the proposed BN, an approach for catenary condition monitoring is presented in Section 5.4 using inspection data from a high-speed railway line. Section 5.5 demonstrates the results and performances of the approach. Conclusions are drawn in Section 5.6.

5.2. Bayesian networks

BNs, also known as belief networks, are a type of probabilistic graphical model based on directed acyclic graphs [39]. This approach combines graph theory and probability theory, which makes it intuitively interpretable and mathematically rigorous. A BN constitutes of a set of random variables with conditional dependencies

between the variables. In the directed acyclic graph of a BN, a node represents a random variable, and a directed arc pointing from node A (the parent node) to node B (the child node) indicates that the value of variable B depends on the value of variable A. Informally, the directed arc between a parent node and its child node forms a cause-effect relationship between the corresponding variables. This representation can be summarized as the local Markov property of BN, which states that each variable is independent of its nondescendants given its parent variables, where the descendants are the set of variables that can be reached on a direct path from the variable [40]. Although the directions of the arcs encode the cause-effect relationships among all variables, inference in a BN can be performed both forward along the arc directions and backward in the reverse directions. In practice, this feature enables estimation of the effect of an event when the status of causes is observed or identification of the causes when the effects are observed. This chapter belongs to the former category.

A BN is defined by a pair (G, θ) , where G is a directed acyclic graph on a set of n nodes (variables) $\mathbf{X} = \{X_1, X_2, \dots, X_n\}$ with independence assumptions among the variables according to the local Markov property, and θ is a set of n conditional probability distributions $\theta = \{p(x_1|\pi_1), \dots, p(x_n|\pi_n)\}$ corresponding to each realization x_i of variable X_i conditioned on π_i , which is the set of parents of X_i in G . The joint probability distribution of variables \mathbf{X} defined by the BN can be described as

$$p(\mathbf{X}) = \prod_{i=1}^n p(x_i|\pi_i). \quad (5.1)$$

When certain of the variables in the BN are observable, they supply evidence for the probabilistic inference of BN to obtain the posterior probability distributions of unobservable variables. This aspect is fundamental for BNs to address the uncertainties associated with diagnosis or prognosis [41], evaluation or assessment [42], forecast or prediction [43], etc.

For most practical problems, the BN must be learned from prior information and relevant data, including specification of both the graph structure and parameters of BN, to fully represent the joint probability distribution. Depending on the problem to be solved, the BN can be learned or estimated in the case in which the graph structure is unknown or certain variables are not fully observable. In this chapter, the graph structure is first established based on the physical relationships among the variables involved in catenary condition monitoring. The parameters of the BN with the specific structure are estimated from historical measurement data. Because the overall condition of the catenary is considered to be a partially observable variable in the proposed BN, the BN parameters in such a case can be estimated by the expectation maximization algorithm [44] or the Markov chain Monte Carlo algorithm [45].

5.3. A BN for catenary condition monitoring

5.3.1. Graph structure

The directed acyclic graph G consists of $n = 6$ variables $\mathbf{X} = \{X_1, \dots, X_6\}$ representing the speed of inspection train, the PIs extracted from the contact wire dynamic stagger (CDS) and dynamic height (CDH), PHA, PCCF, and the status of catenary condition (SCC), respectively. Figure 5.2 depicts the structure of graph G , where the conditional dependencies among the six variables are indicated by the directed arcs. The physical relationships underlying the structure are described as follows:

1) Variable X_1 represents the train speed at the moment when the data are measured. As a parent node, it is directed to the four variables representing the PI extracted from CDS, CDH, PHA and PCCF, respectively. This direction is based on the fact that the faster the train speed, the more intense the vibration excited between the pantograph and catenary, which leads to higher amplitude of oscillations in the four types of dynamic responses. Thus, the PIs from the four types of data are dependent on the level of train speed when the data are measured. At the same time, the speed of inspection train itself is irrelevant to the SCC, and thus no arc is connecting the two variables.

2) Variables X_2, X_3, X_4 , and X_5 represent PIs extracted from CDS, CDH, PHA and PCCF, respectively. Because they are all indicators for the SCC X_6 , they affect the value of the SCC with four directed arcs pointing to the SCC in the graph structure shown in Figure 5.2.

3) Variable X_2 represents the PI extracted from the CDS, which is the only parameter measured in the lateral direction parallel to the ground. This variable reflects whether the stagger of the contact wire is within an acceptable range for pantograph contact. The CDS is not physically related to the data of CDH, PHA and PCCF, because the latter three parameters are defined and measured in the direction vertical to the ground.

4) Variables X_3, X_4 , and X_5 represent the PIs extracted from CDH, PHA and PCCF, which are all dynamic responses in the vertical direction. Assuming that at a time instant t during the pantograph-catenary interaction, the CDH $h_c(t)$ is uplifted by the pantograph head with an acceleration $a_p(t)$. If the contact between the pantograph and catenary is continuously maintained by the PCCF $f_c(t) > 0$, the CDH $h_c(t)$ becomes numerically equivalent to the vertical displacement of the contact point, and the PHA $a_p(t)$ becomes equivalent to the vertical acceleration of the contact point. Thus, the relationship between the CDH $h_c(t)$ and the PHA $a_p(t)$ can be written as

$$a_p(t) = \frac{d^2}{dt^2} h_c(t). \quad (5.2)$$

This relationship can be transformed from the time domain to the frequency domain by the Fourier transform as

$$\widehat{a}_p(\xi) = F(a_p(t)) = (2\pi i \xi)^2 \widehat{h}_c(\xi) = -4\pi^2 \xi^2 \widehat{h}_c(\xi) \quad (5.3)$$

where $F(a_p(t))$ denotes the Fourier transform of $a_p(t)$, $\widehat{h}_c(\xi) = F(h_c(t))$, and ξ

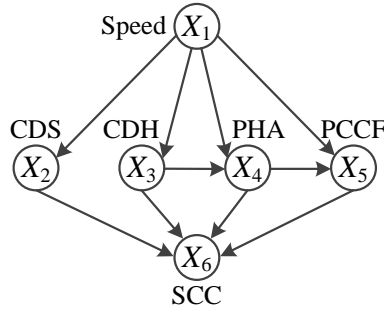


Figure 5.2: Graph structure of the BN for catenary condition monitoring.

denotes frequency. This formulation reflects that

$$|a_p(\xi)| \propto |\xi^2 \widehat{h}_c(\xi)|. \quad (5.4)$$

Therefore, when the vibration response induced by a defect or fault of the catenary with a certain frequency can be captured by the CDH, it can also be observed from the PHA with a higher level of spectral energy. This representation forms a correlation between the PIs of CDH and PHA that can be mapped into the directed acyclic graph of BN as a directed arc between the two variables, as shown in Figure 5.2. In the measurements, the PCCF $f_c(t)$ is considered to be the sum of three component forces [46, 47], i.e. the pressure measured by force sensors $f_{\text{sensor}}(t)$, the inertia force $f_{\text{inertia}}(t)$ and the correction of aerodynamic force $f_{\text{aero}}(t)$,

$$f_c(t) = f_{\text{sensor}}(t) + f_{\text{inertia}}(t) + f_{\text{aero}}(t). \quad (5.5)$$

The inertia force $f_{\text{inertia}}(t)$ is calculated depending on where the force sensors are installed on the pantograph. If the sensors are installed under the pantograph head, i.e., the majority of the cases, the inertia force is given by

$$f_{\text{inertia}}(t) = m_p \cdot a_p(t) \quad (5.6)$$

where m_p is the mass of the pantograph head. It can be observed that the measurement data of PCCF depend on the PHA data. The PCCF $f_c(t)$ inherits a portion of the dynamic responses contained in the PHA $a_p(t)$. Thus, a directed arc pointing from variable X_4 to variable X_5 is established in the BN, as shown in Figure 5.2, indicating a cause-effect relationship between the data of PHA and PCCF.

Through the relationships formed between the six variables, the graph structure of the BN supplies a physics-based model that integrates all available sources of PIs to comprehensively evaluate the SCC. The next step is quantifying the SCC, namely, obtaining a comprehensive key performance indicator (KPI) of the catenary by specifying the probabilistic relationships between the variables based on historical observations.

5.3.2. Variable extraction

The observations of the six variables are extracted from historical measurement data, and the method of extraction varies for each variable. As a prerequisite,

the different types of measurement data should be synchronized to ensure matching sampling frequency and spatial location. A synchronized data set ensures that the data of different catenary parameters reflect the same dynamic responses excited at the same moment. This condition is fairly important for obtaining accurate probabilistic relationships between variables. In practice, it is uncommon to have perfectly synchronized data because the data are measured by separate sensors, especially when the inspection train runs at a high speed. Therefore, it is necessary to mitigate synchronization errors that might cause inaccurate outputs generated from the data. This synchronization can be performed by calibrating the position of all data based on a unified reference position in the data set. In addition, the data can also be reconstructed by downsampling to a lower frequency to offset minor errors in position. In this manner, synchronization errors between different data types can be mitigated, especially those leading to shifting of features in spatial position.

The following describes the PI extraction of every variable in a manner that best reflects and quantifies the catenary condition.

5

Speed X_1

As the only variable with unconditional probability in the proposed BN, the train speed X_1 is of great importance. Without knowing the level of train speed, evaluation of the catenary condition based only on the four types of dynamic responses is meaningless and invalid. To establish a corresponding relationship between the level of speed and the intensity of the dynamic responses using the available data, a step size s_{step} is chosen to partition the data into different levels of speed. This step size is selected to ensure that sufficient data are measured under each level of speed for estimation of the parameters of BN. In this way, the data for extracting variables X_2 , X_3 , X_4 and X_5 are automatically partitioned by the levels of speed.

CDS X_2 and CDH X_3

Compared with the static position of the contact wire, the dynamic position of the contact point during operation (hereafter referred as the dynamic position of the contact wire) vibrates in both the vertical and lateral directions, resulting in the CDS and CDH, as schematically shown in Figure 5.3. For evaluation of the catenary condition, the CDS and CDH behave in a similar manner and are normally equal to or greater than the static values because a positive contact force always uplifts and also laterally deflects the contact wire. Thus, an excessive peak or trough in the CDS and CDH indicates a strong impact on the contact wire, loss of contact, or abnormal contact wire positioning, which reflects an unfavorable condition that requires attention.

To extract PIs for variables CDS X_2 and CDH X_3 that can supply evidence for variable X_6 , the frequency contents contained in the CDH and CDS are not extracted because according to (5.4), an anomaly is more significantly perceived in the frequency domain of acceleration rather than that of displacement. Additionally, in the proposed BN, the frequency-domain PI is considered for variable X_4 . Therefore, the PIs for variables X_2 and X_3 , both extracted from a measure of displacement, are time-domain indicators determined by the deviations of CDS and CDH from their

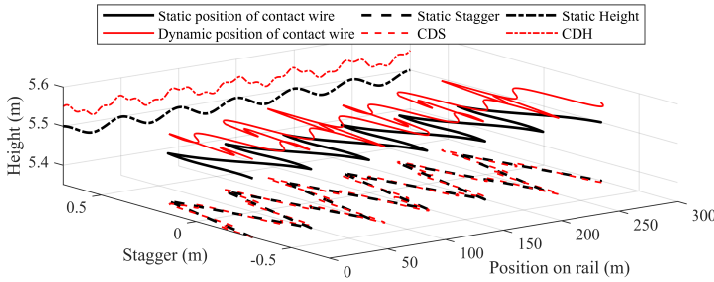


Figure 5.3: Comparison between the static and the dynamic spatial position of contact wire.

healthy states. The definitions of healthy states for CDS and CDH are dependent on the levels of speed segmented by the step size s_{step} . Based on large amounts of historical data partitioned into every speed level, the PIs of CDS X_2 and CDH X_3 can be extracted at each speed level, thus building the dependencies of X_2 and X_3 on the speed level X_1 .

To determine whether the value of CDS or CDH is healthy or not, the judgement is highly dependent on the monitored catenary because the structural parameters (including the suspension type, nominal position of contact wire, contact wire tension, etc.) are diverse by design for different railway lines. Thus, the healthy range of variation for CDS and CDH should be defined with respect to the change in speed for a specific catenary. This definition can be constructed in a data-driven manner based on sufficient historical data from the same catenary. It is also implied that the majority of the observations should represent a healthy condition of the catenary for the data to be sufficient. The percentile of available observations can be used to perform statistics-based clustering in which the probability of a value falling into a certain condition level is quantitatively considered.

Concretely, assuming that a set of CDS or CDH data $C = \{c_1, c_2, \dots, c_N\}$ is partitioned to a certain speed level, the N observations can be clustered into J ($2 \leq J \leq N$) sets $\mathbf{S} = \{S_1, S_2, \dots, S_J\}$ corresponding to J levels of condition of CDS or CDH, which are viewed as the time-domain PIs extracted from CDS or CDH at the specific speed level. As an example shown in Figure 5.4, the observations in C can be clustered based on the percentile intervals defined by the percentile boundary of healthy observations h_1 , which is defined as the data located in the middle of the full percentile, and the percentile boundaries of unhealthy observations $\{h_2, \dots, h_J\}$, which are data located at both ends of the full percentile. This representation can be mathematically written as

$$S_j = \begin{cases} P(h_1) \setminus P(100 - h_1), & j = 1 \\ P(h_j) \setminus P(100 - h_1) \setminus \bigcup_{m=1}^{j-1} S_m, & 2 \leq j < J \\ P(100) \setminus \bigcup_{m=1}^{J-1} S_m, & j = J \end{cases} \quad (5.7)$$

where \setminus denotes the set difference operator, and $P(h_j)$ denotes the h_j th percentile of the data in set C . To include all data in C , h_j should be equal to 100. The se-

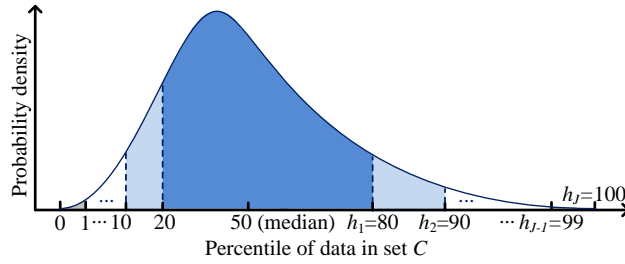


Figure 5.4: Illustration of the percentile-based clustering.

lection of h_1 ($h_1 > 50$) determines the tolerance of the system against unhealthy conditions reflected by CDS or CDH, and the sensitivity to report such unhealthy conditions through the system. The number of levels J depends on the demand to subdivide the levels of unhealthy conditions; nevertheless, it cannot be too large by displaying too many levels of unhealthy conditions that produce redundant information. Normally, a classic description of healthy or low, medium, high or extreme risk levels in risk assessment can be sufficient, meaning that $J = 5$. In this context, the values from h_2 to h_J should ascend in a decelerating manner such that S_J contains the smallest set of data for the most extreme condition. When the CDS or CDH data partitioned to every speed level are clustered based on the corresponding percentiles, the influences of speed on CDS or CDH are automatically considered for evaluation of the catenary condition.

PHA X_4 and PCCF X_5

As noted by previous studies [24, 26], both PHA and PCCF contain frequency contents that are useful for reflecting the catenary condition. In particular, the catenary structure wavelengths (CSWs) have a strong correlation with the catenary structure, including anomalies such as installation errors and structural defects. As shown in Figure 5.5, the CSWs are frequency components of PHA and PCCF attributed to the cyclic variation of the contact wire stiffness along the catenary structure. Thus, the PHA and PCCF can be decomposed into two signals, namely, the CSWs and the non-CSW signal. The former is often used as an indication for structure-related defects, and the latter mostly reflects local defects such as hard points and uneven wear on the contact wire. In this way, diagnoses based on PHA and PCCF can be performed with less interference and thus output more accurate results compared with the situation in which the PHA and PCCF are not decomposed. Empirical mode decomposition (EMD) [48] is commonly selected to perform an adaptive decomposition so that the PHA and PCCF measured from different catenary systems can be consistently decomposed into the CSWs and the non-CSW signal. The general steps needed to obtain the two signals are described as follows using the PCCF signal $f_c(t)$ as an example:

Step 1: Decompose the PCCF signal $f_c(t)$ into a number of intrinsic mode functions

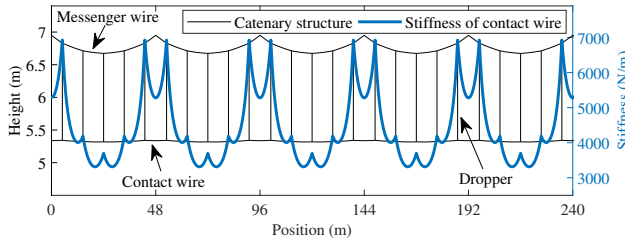


Figure 5.5: Schematic of contact wire stiffness varying cyclically with the catenary structure. The left vertical axis shows the height of catenary structure including the messenger wire, contact wire and droppers, and the right vertical axis shows the stiffness.

(IMFs) $f_{c,l}(t)$ and a residual $r(t)$ using EMD or its improvements,

$$f_c(t) = \sum f_{c,l}(t) + r(t). \quad (5.8)$$

Step 2: Identify the CSWs from all IMFs by checking whether the dominant wavelength (or spatial frequency) of an IMF falls into the range of structure wavelengths. Two generic wavelength intervals [4m,10m] and [40m,70m] indicating the wavelengths of interdropper distances and spans, respectively, can be used in the identification, even if no prior information on the catenary is available to narrow them down.

Step 3: Based on the IMFs identified as CSWs $f_{c,l}(t)$, $l \in C$, compute the CSWs $f_{c,C}(t)$ and non-CSW signal $f_{c,N}(t)$ by

$$f_{c,C}(t) = \sum_{l \in C} f_{c,l}(t) \quad (5.9)$$

and

$$f_{c,N}(t) = \sum f_{c,l}(t) - f_{c,C}(t), \quad (5.10)$$

respectively.

After obtaining the CSWs and the non-CSW signal of PHA and PCCF, the energy density of both signals corresponding to the instantaneous frequencies can be computed as the sources of frequency-domain PIs. Using the CSWs of PCCF $f_{c,C}(t)$ as an example, the analytic forms of its IMFs $f_{c,l}(t)$, $l \in C$ can be obtained with the Hilbert transform:

$$z(t) = f_{c,l}(t) + i \cdot \mathcal{H}[f_{c,l}(t)] = a(t)e^{i\theta(t)} \quad (5.11)$$

where $\mathcal{H}[f_{c,l}(t)]$ denotes the Hilbert transform of $f_{c,l}(t)$,

$$a(t) = \sqrt{f_{c,l}(t)^2 + \mathcal{H}[f_{c,l}(t)]^2} \quad (5.12)$$

and

$$\theta(t) = \arctan\left(\frac{H[f_{c,l}(t)]}{f_{c,l}(t)}\right). \quad (5.13)$$

The instantaneous frequency is defined as

$$\omega(t) = \frac{d\theta(t)}{dt}. \quad (5.14)$$

Thus, the Hilbert spectrum of $f_{c,c}(t)$ can be obtained as the real part \mathcal{R} in the following form

$$H(\omega, t) = \mathcal{R} \left\{ \sum_{l \in \mathcal{C}} a(t) \exp \left[i \int \omega(t) dt \right] \right\} \quad (5.15)$$

which is a time-frequency representation showing the energy density distributed with the change in time and instantaneous frequency. To examine the instantaneous energy level of the CSWs $f_{c,c}(t)$ at a certain time instant, the accumulated energy density can be computed as

$$A(t) = \sum_{l \in \mathcal{C}} a(t)^2. \quad (5.16)$$

This parameter indicates the intensity of vibration at a frequency range identical to that of the CSWs or non-CSW signal. It can thus be applied for fault diagnosis in general and also supplies PIs for the catenary at the specific location.

The PIs input into the BN as values of variable PHA X_4 and PCCF X_5 , similar to the time-domain PIs extracted from CDS and CDH, should be indicators clustered into different levels. For consistency with the PIs from CDS and CDH, it is ideal that those from PHA and PCCF share the same number of condition levels. Because the PIs result from the same excitations, a certain coherence is preserved if they are clustered in the same way, in the sense that an equivalent PI among the four types of variables indicates the same degree of 'unhealthiness' or defect. Moreover, this coherence can be passed down to the final variable SCC X_6 in the form of evidence for probabilistic inference. However, both PHA and PCCF are decomposed into two signals and thus have two independent indicators $A_C(t)$ and $A_N(t)$ via (5.16) from the CSWs and the non-CSW signal, respectively. Both indicators represent the catenary condition in the frequency range corresponding to their own physical meanings. This is a unique feature of the indicators extracted from PHA and PCCF, because no such frequency contents can be found in CDS and CDH. Thus, a PI of variable X_4 or X_5 should be constructed to preserve the information contained in both indicators. A maximum criterion is proposed to combine the two indicators. Concretely, for the PHA or PCCF, indicators $A_C(t)$ and $A_N(t)$ can be partitioned by the same speed levels defined by step s_{step} such that the influences of speed variation are eliminated. Sets C_C and C_N are indicators partitioned to a same speed level from $A_C(t)$ and $A_N(t)$, respectively. Using percentile-based clustering according to (5.7), sets $\mathbf{S}_C = \{S_{C,1}, S_{C,2}, \dots, S_{C,J}\}$ and $\mathbf{S}_N = \{S_{N,1}, S_{N,2}, \dots, S_{N,J}\}$ can be obtained from C_C and C_N , respectively. Consequently, this formulation gives a condition level

Table 5.1: List of SCC Values (KPIs) with Respect to Verifying Parameters

#	Verifying parameter	# of severity levels	SCC X_6
1	Contact wire height	4	[1,5]
2	Height difference in a span	2	{1,3,5}
3	Contact wire stagger	4	[1,5]
4	Maximum PCCF	4	[1,5]
5	Minimum PCCF	4	[1,5]
6	Standard deviation PCCF	2	{1,3,5}
7	Hard point	4	[1,5]
8	Duration of arcing	2	{1,3,5}
9	Percentage of arcing	2	{1,3,5}
10	Angle of steady arm	1	{1,3}
11	Catenary voltage	1	{1,3}
12	EMU current	1	{1,3}

to every value in $A_C(t)$ and $A_N(t)$. Assuming at any time instant t' ,

$$A_C(t') \in S_{C,a} \quad \text{and} \quad A_N(t') \in S_{N,b}. \quad (5.17)$$

which equivalently assigns condition levels, namely, PIs a and b to $A_C(t')$ and $A_N(t')$ as

$$L_C(t') = a \quad \text{and} \quad L_N(t') = b. \quad (5.18)$$

The maximum criterion defines a combined PI as

$$L(t') = \max(L_C(t'), L_N(t')). \quad (5.19)$$

In this manner, an unhealthy condition can be always reported regardless of its indicative frequency range. It is not only consistent with PIs of CDS and CDH, but also offers necessary evidence for the variable SCC X_6 .

SCC X_6

This is the only variable with partial observability in the BN and is also an output as the quantification of SCC for maintenance decision-making. In this context, the available observations of variable X_6 are defined as the severity of defects that are detected in an inspection run and, most importantly, verified later by human inspectors on site. Due to the massive workload required to perform manual verifications, in most cases, only a portion of historical inspection results can be selectively verified and recorded as observations, thus creating the partial observability.

Although the protocols established to verify catenary defects differ from one railway line to another, the results normally conclude whether a defect exists and its severity. The SCC X_6 supplies such a conclusion based on the evidence given by the other variables, whereas previously, only the observations from one variable in a single run were considered. Thus, the value of SCC is the overall condition level of the catenary, namely, a KPI that considers all potential defects reflected by the available observations of other variables. This can be achieved by unifying the different severities of all known defect types. Based on expert experience, the unified

value can be manually estimated according to the severity of defects defined in protocols. In a protocol designed to quantify the severity level of catenary defects, the severity levels are commonly defined by a group of multidisciplinary experts who consider both the mechanical and electrical performances of the catenary. To propose a unified severity level considering all types of defects, the potential negative effects or consequences of a defect at different severity levels should first be quantitatively estimated in terms of cost, loss of time, etc. Subsequently, the probability of such effect actually occurring is also estimated using maintenance records and available knowledge. By multiplying the effect with the corresponding probability, the risk of a defect can be obtained as a unified value indicating the healthiness of the catenary. In this manner, a unified condition level can be defined rationally with controllable variations depending on the accuracy of the effect and probability estimations.

As a new paradigm, Table 5.1 proposes a summarized list of the estimated catenary condition levels in the case of high-speed lines in China. The condition levels correspond to a certain type of catenary defect indicated by a verification parameter measured on-site. A total number of 12 verification parameters, each with several levels of severity determined by predefined thresholds, are assigned to the unified values of SCC X_6 as a standardization effort. It can be observed from Table 5.1 that depending on the type of verification parameter, the numbers of the severity levels are different. This scenario is defined by the protocol for inspection of high-speed railway catenaries, in which parameters such as the contact wire height are divided into four levels of value corresponding to four severity levels, and other parameters such as the percentage of arcing has two levels and the catenary voltage has one level, meaning that it is out of a required range. The values of SCC, namely, the KPIs range from 1 to 5 with 1 representing a healthy state and higher values representing unhealthier conditions. The range is consistent with the values defined for variables from X_2 to X_5 . This list is applied to obtain the available observations of variable X_6 that indicate the verified condition level of the catenary in the maintenance record. In addition, a number of observations with value 1 (healthy) are assigned to variable X_6 , when the corresponding observations of variables from X_2 to X_5 are 1, showing no indication that the catenary is unhealthy. Similarly, a number of observations with value 5 (extreme risk) are also assigned when the observations of the four variables are all equal to 5. For a specific railway line, the list can be modified by considering the differences in operation condition and pantograph-catenary dynamic characteristics.

5.3.3. Parameter estimation

The proposed BN has a known structure but incomplete observability for variable SCC X_6 . In the case of full observability, the maximum likelihood estimation can directly find a set of parameters that maximize the likelihood function of the given set of probabilistic relationships defined by the BN structure. When data are partially missing, an initial set of BN parameters can be assumed to complete the missing data through inference. A new expected likelihood function can be computed based on the newly completed data set. This procedure is known as expectation. The set

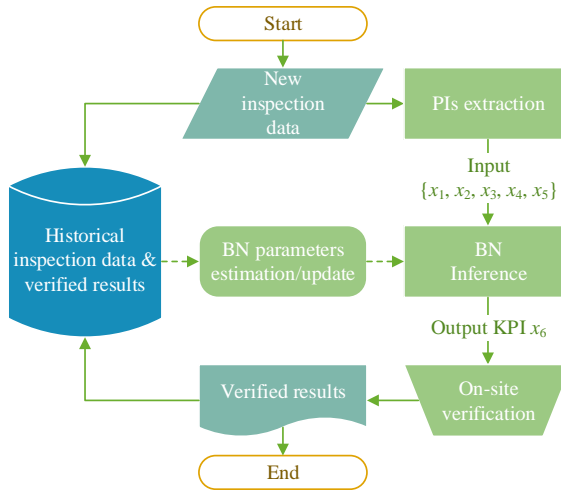


Figure 5.6: Brief flowchart of the BN-based approach. The dashed lines denote alternative flows.

of BN parameters can be updated by maximizing the current expected likelihood function, which is known as maximization. By iterating between the expectation and the maximization, a final set of parameters can be eventually estimated when the likelihood function converges, which is the well-proven realization of the expectation maximization (EM) algorithm for estimating parameters of the BN with incomplete data [44]. The use of the EM algorithm requires that the data are missing at random, meaning that the value of X_6 and the event that X_6 is missing are conditionally independent, given other observed variables, which is true in this case because the existence of SCC is independent of whether the SCC is verified on site or not.

In this application, the parameters estimated based on a set of data by nature inherit the dynamic characteristics of the specific catenary type and pantograph-catenary couple from the line on which the data set is measured. Therefore, the input data should be measured from the same railway line when the same pantograph is mounted. This situation is often realized by a specialized inspection train.

5.4. A BN-based approach

Based on an established BN, a data-driven approach for catenary condition monitoring is proposed. Figure 5.6 depicts the general architecture of the approach for a railway line with inspection data available. The approach initiates with BN parameter estimation. New inspection data can subsequently be input for catenary condition assessment. The BN parameters are updated after on-site verifications are performed.

When the BN parameters are estimated, the ratio of variation (ROV) of a parent variable to its child can be computed. This value quantifies the importance or contribution of a parent variable that leads to the value of its child. For the proposed BN, the ROV can be used to describe which of the four variables representing the

PIs of CDS, CDH, PHA and PCCF, respectively, have more impact on the final KPI of SCC. Concretely, the ROV of variable X_i with respect to the final variable X_6 is defined as:

$$R(X_i) = \frac{p(x_i \neq 1 | x_6 = j) - p(x_i \neq 1)}{p(x_i \neq 1)} \quad (5.20)$$

where $p(x_i \neq 1)$ is the marginal probability of $x_i \neq 1$, representing the probability that variable X_i is unhealthy.

5.4.1. Input

An estimated BN can be applied as a diagnostic tool formulated based on the historical data for parameter estimation and expert knowledge for defect verification and severity quantification. Because the BN is estimated using inspection data from a certain railway line, it can only function correctly when the input is also extracted from new data measured in the same line. New inspection data containing CDS, CDH, PHA and PCCF together with the train speed can be used in input extraction. The BN inputs are values of variables from X_1 to X_5 , namely, the speed level, PIs extracted from CDS, CDH, PHA and PCCF. The PIs should be extracted in the same manner as described in the previous section and summarized as follows:

- Step 1: Synchronize data with respect to sampling frequency and spatial position.
- Step 2: Decompose the PHA and PCCF data into CSWs and non-CSW signal by (5.9) and (5.10).
- Step 3: Partition the CDS, CDH, decomposed PHA and PCCF data into different speed levels determined by a step size s_{step} .
- Step 4: Extract the PIs of CDS and CDH based on their data percentiles using (5.7), and the PIs of PHA and PCCF using (5.19).

It should be noted that the BN parameters can always be updated by new inspection data and the corresponding verified defects. This update can be performed regularly to make the BN more knowledgeable and up to date for catenary condition assessment. The feedback loop formed among the BN-based condition assessment, the on-site defect verification and the BN parameter updates can further improve the accuracy of condition assessment and defect detection.

5.4.2. Output

Given the BN input, i.e., the values of variables from X_1 to X_5 , as evidence for BN inference, the posterior probability of the final KPI $x_6 = j$, i.e., $p(x_6 = j | \{x_2, x_3, x_4, x_5\})$, can be inferred. The expectation of the posterior probability distribution of variable SCC X_6 can be computed as the final output:

$$E(X_6) = \sum_{j=1}^J p(x_6 = j | \{x_2, x_3, x_4, x_5\}) \cdot j. \quad (5.21)$$

The output KPI indicates the expected condition level of the catenary at the corresponding location where the data are measured. Alternatively, the output KPI can be the most probable value of variable X_6

$$\arg \max_j p(x_6 = j | \{x_2, x_3, x_4, x_5\}). \quad (5.22)$$

This KPI of SCC is stricter and especially useful for recognizing unhealthy conditions compared with the expected value. Depending on the preference of the decision makers, the expected value can be used in general condition assessment, and the most probable value is better for determining whether a track visit is necessary by looking at SCC at suspicious unhealthy locations.

5.5. Results and performance discussions

This section presents the results of BN estimation and application of the estimated BN. The condition monitoring performances of the BN-based approach for reducing false alarms and addressing low-quality data are discussed. Hereafter, the potential defects of the catenary represent defects that are identified based only on the inspection data without on-site verifications. When on-site verifications are performed for the potential defects, the hits and false alarms are defined as the successfully verified defects and falsely identified defects, respectively. Accordingly, the hit rate and false alarm rate are the ratios of the numbers of hits and false alarms to the total number of potential defects, respectively. In practice, because on-site verifications were not performed for every potential defects found from historical data, this study considers the defects that were actually verified when calculating the number hits and false alarms detected by the proposed approach.

5.5.1. BN estimation

The BN parameters can be estimated through available observations extracted from historical data. In this chapter, the data used as the source of observations are periodic inspection data measured from a section of Beijing-Guangzhou high-speed line in China during a period from December 2014 to June 2018. All measurements of speed, PCCF, PHA, CDH and CDS have a synchronous sampling interval of 0.25 m with the position recorded and calibrated by differential GPS and radio-frequency identification (RFID) using RFID tags attached on the masts of the catenary along the railway line. Observations of variables are extracted per procedures presented in the previous section. As a result of the periodic inspection, approximately 1.546×10^6 observations are acquired from an accumulated mileage of 1546.4 km of the catenary in the same section of railway line with the speed of the inspection train ranging from 100 km h^{-1} to 300 km h^{-1} . Data measured below 100 km h^{-1} are omitted because the data size is too small to represent a set of balanced observations at lower speed levels. These data can still be added for estimation of the BN parameters if sufficiently collected. Figure 5.7 shows the number distribution of observations with respect to the speed above 200 km h^{-1} , which contains 94.9% of all observations. Because the inspection train is dedicated to run near 290 km h^{-1} in every inspection, 78.7% of observations are located at speeds

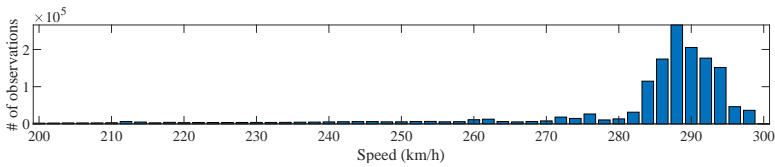
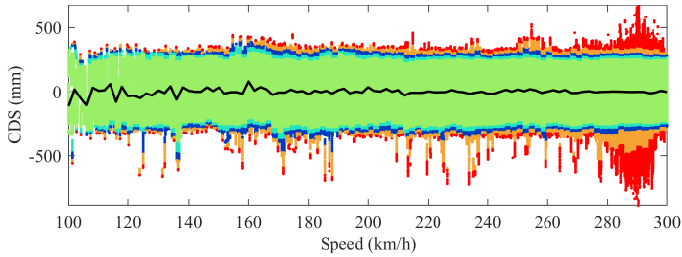
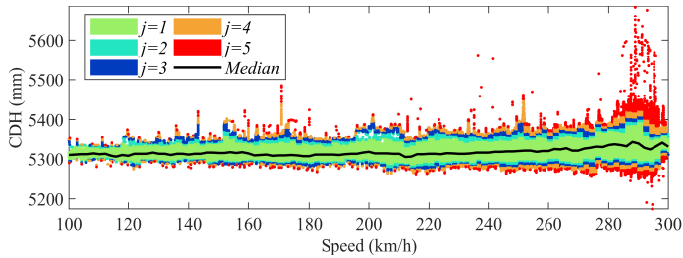


Figure 5.7: Number of observations distributed with inspection train speed.



(a)



(b)

Figure 5.8: Clustered (a) CDS and (b) CDH with respect to speed levels.

between 280 km h^{-1} and 300 km h^{-1} . Other speeds are mostly measured when the inspection train is accelerating or decelerating.

In this study, the step size $s_{\text{step}} = 2 \text{ km h}^{-1}$ is selected for data partitioning, meaning that for every 2 km h^{-1} increase from zero speed, the data measured within an increment are considered under the same speed level. Once all data are partitioned by speed levels X_1 , the values of variables from X_2 to X_5 are extracted. Figure 5.8 depicts the PI values j of CDS X_2 and CDH X_3 clustered by (5.7) using the set of percentile boundaries $\{h_1, \dots, h_5\} = \{95, 97.5, 99, 99.8, 100\}$, which represent the condition level of healthy, low risk, medium risk, high risk, and extreme risk, respectively. It can be generally observed that the greater the speed, the larger the deviation of CDS and CDH. An outburst of extreme-risk conditions occurs at approximately 290 km h^{-1} , because the observations are concentrated at this speed level, which is close to the highest speed designed for this railway line. The clustered CDS in Figure 5.8(a) are evenly distributed around the median, which is approximately zero, whereas the median of CDH and the range of healthy CDH ($j = 1$) gradually increase as the speed increases in Figure 5.8(b). A sudden narrowing of the CDH range can be noted near the highest speed level, which is caused

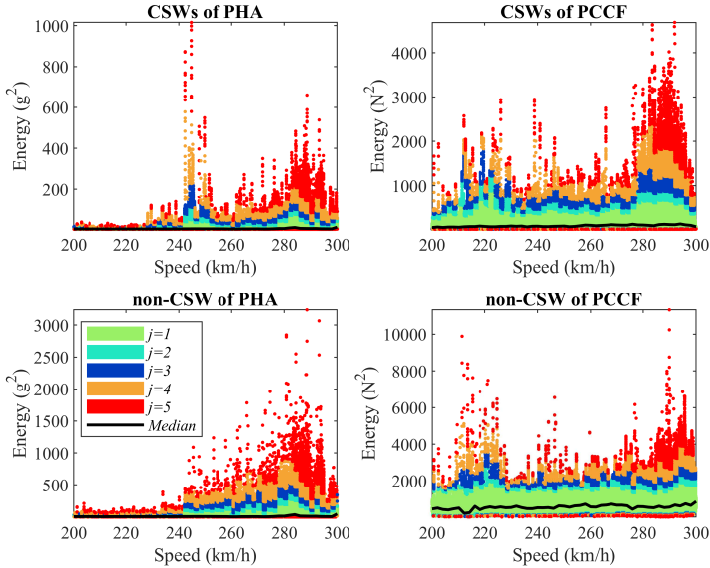


Figure 5.9: Clustered instantaneous energy of CSWs and non-CSW signal of PHA (left) and PCCF (right).

by the drastic drop in observation number starting from 296 km h^{-1} , as shown in Figure 5.7.

For variables X_4 and X_5 , the CSWs and non-CSW signal are first extracted to obtain the accumulated instantaneous energy via (5.16). Using the same percentile boundaries for CDS and CDH, Figure 5.9 depicts the clustered energy of the CSWs and non-CSW signal of PHA on the left and those of PCCF on the right. It can be observed that the distribution of unhealthy indicators ($j > 1$) differs between the CSWs and the non-CSW signal, and between the PHA and PCCF. In all four types of clustering results, the catenary condition worsens at high speeds near 290 km h^{-1} . On the left, the CSWs of PHA reveals a particularly sensitive speed at approximately 245 km h^{-1} , where the condition also worsens, whereas the result of non-CSW signal shows no such particularity. This result indicates that for this pantograph-catenary couple, the dynamic responses related to the structural parameters of the catenary are sensitive under this operation speed. Similarly, the results of PCCF on the right reflect that speeds near 225 km h^{-1} and 215 km h^{-1} are particularly sensitive for the CSWs and non-CSW signal of PCCF, respectively. These results are crucial for inclusion in probabilistic inference such that the influences of speed variation, especially these sensitive speeds, are already considered in the parameter estimation of BN. Consequently, Figure 5.10 depicts the final clustering results from PHA and PCCF combining those from CSWs and non-CSW signal by applying (5.19). As the combination between two independent indicators covering different frequency ranges, the percentage of unhealthy condition levels increases compared with the predefined percentile boundaries. Additionally, an overall ten-

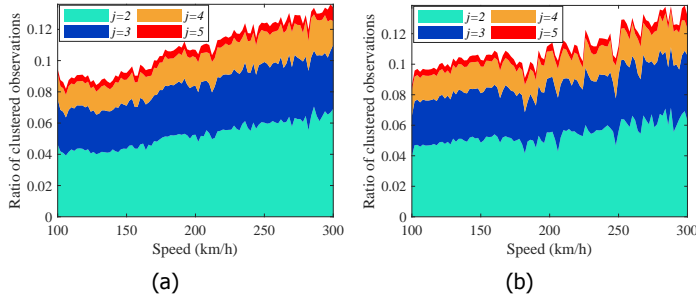


Figure 5.10: Clustering results from (a) PHA and (b) PCCF showing the ratio of clustered observation number to the total observation number at every speed level when $j \geq 2$.

Table 5.2: ROVs of Variables from X_2 to X_5 with Respect to X_6

j	$R(X_2)$	$R(X_3)$	$R(X_4)$	$R(X_5)$
2	0.880	0.740	1.013	0.909
3	0.697	1.286	0.791	1.003
4	0.463	0.627	1.323	0.985
5	1.244	0.811	0.732	1.032
Total	3.284	3.464	3.859	3.929

endency to increase with the increasing speed is also found in the results of both PHA and PCCF. This result shows that the catenary performance gradually declines as more PIs worsen at higher speeds. This observation is in line with the time-domain PIs extracted from CDS and CDH.

The observations of the final variable SCC X_6 are verified defects quantified through Table 5.1 and healthy observations indicated by parent variables. As a variable with incomplete observability, the available observations are assigned to X_6 according to the location of a defect and the corresponding observations of parent variables from X_2 to X_5 that triggered the verifying procedure. In total, 9.090×10^3 observations of defects are assigned to X_6 , and 8.446×10^5 healthy observations are found as all values of parent variables are 1, which results in a 55.2% observability of variable X_6 . The remainder of the observations and BN parameters are estimated by the EM algorithm such that the BN is finally inferable.

Table 5.2 gives the ROVs of variables from X_2 to X_5 when $j \geq 2$ defined by (5.20). It is shown that at condition levels of variable X_6 from 2 to 5, variables representing the PHA, CDH, PHA and CDS have the highest impact on the SCC, respectively. These variables are more indicative at the specific condition level than other variables. Notably, the CDS becomes highly impactful for the worst SCC when $j = 5$, because it is the only source of indicator measured in the lateral direction and thus offers particularly strong evidence indicating a severe condition. Overall, the total ROVs accumulated from all unhealthy SCC show that the PIs of PCCF X_6 contribute the most to an unhealthy SCC among all variables. This observation is in line with the fact that PCCF is considered to be a direct reflection of the catenary performance.

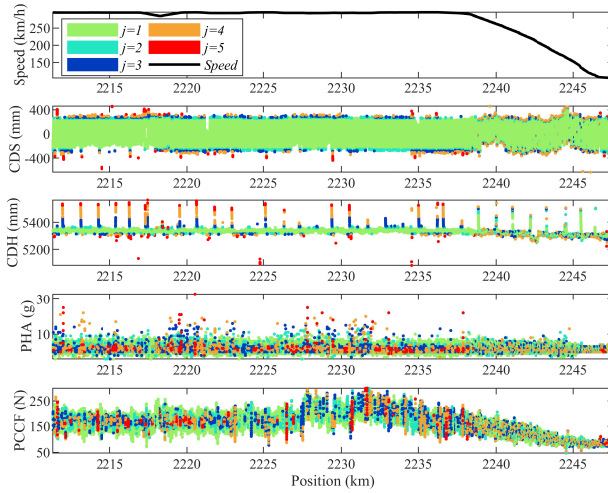


Figure 5.11: A segment of new and reconstructed inspection data set with PIs extracted and shown. The speed, CDS, CDH, PHA, and PCCF are depicted from top to bottom.

5.5.2. Reduction in false alarms

Hereafter, new inspection data are applied for result analysis. The differences of measurement condition in different inspection runs are considered insignificant for the collection and quality of data. Figure 5.11 depicts a set of new inspection data for extraction of the BN inputs. The PIs are extracted from the CDS, CDH, PHA and PCCF and are shown by different colors. From the speed profile, it can be observed that this data set represents first a uniform motion followed by a deceleration of the inspection train. The effect of deceleration on the four types of parameters can be observed from 2238 km to the end. The ranges of parameter variation become narrower as the speed decreases. Some unstable vibrations are also found during the deceleration, especially in the lateral direction reflected by the CDS. These effects are considered by the proposed BN with the BN parameters estimated based on historical data with similar characteristics. For the PHA and PCCF, PIs are extracted based on frequency features such that they can indicate an unhealthy condition even when the corresponding time-domain value is low. The speed levels and PIs generated from the new data can be subsequently input into the BN to obtain the output through inference.

According to the record of on-site verifications performed based on the new segment of inspection data, this data section resulted in a 58.3% rate of false alarm among 132 potential defects verified on site, which is particularly high out of all data sections from the same inspection run. The on-site verification procedures were triggered by predefined thresholds that identified potential defects as peaks or troughs in the data.

By applying the BN-based approach, Table 5.3 gives the summarized statistics of the detection results from the data section compared with previous results. The

Table 5.3: Improvements in Hit Rate and False Alarm Rate

Type	Amount	Rate	# of SCC $x_6 = j$			Rate of $x_6 \geq 4$
			$j \leq 3$	$j = 4$	$j = 5$	
False alarms	77	0.583	64	10	3	0.169
Hits	55	0.417	2	13	40	0.964

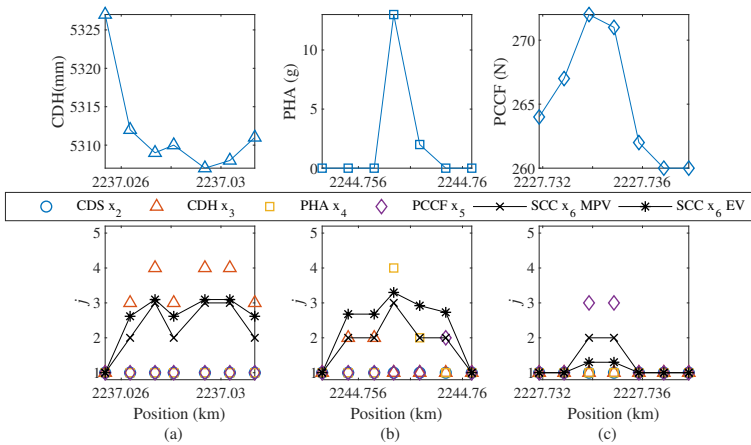


Figure 5.12: Three previous false alarms that are identified as medium risk or below ($j \leq 3$) by the BN-based approach. The false alarms were previously triggered by the (a) CDH, (b) PHA and (c) PCCF data shown at the top, respectively. The data PIs and BN outputs using the most probable value (MPV) and the expected value (EV) are shown at the bottom.

first two columns present the previous results using the traditional threshold-based method that identified 132 potential defects in total. The output KPIs of SCC are the most probable values from BN inference by (5.22). It can be observed that most of the previous false alarms are recognized as medium risk or lower with $j \leq 3$ and most of the previous hits are recognized as high or extreme risk with $j \geq 4$. When the criterion for determining a potential defect and triggering an on-site verification is that the output risk level at a certain location is high or extreme with a KPI $j \geq 4$, only 16.9% of previous false alarms remain, and 96.4% of previous hits are still correct. This results in an improved false alarm rate of 19.7%, i.e., 66.2% lower than the previous rate, and a new hit rate of 80.3% out of all 66 new potential defects with KPI $j \geq 4$. Both the amount of potential defects and the rate of false alarms are largely reduced according to the output most probable SCC values. Thus, the BN-based approach offers the potential to save a notable amount of maintenance resources if implemented for an entire railway line or network.

As examples, Figure 5.12 depicts three previous false alarms that are identified as medium or lower risk ($j \leq 3$) by the BN output KPI. In Figure 5.12(a), the CDH on the top becomes too low, which triggered an on-site verification, while the output

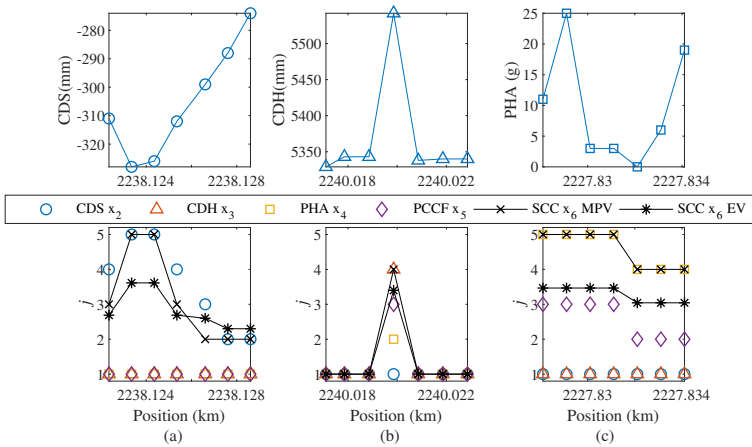


Figure 5.13: Three previous hits that are identified as high or extreme risk ($j \geq 4$) by the BN-based approach. The hits were previously triggered by the (a) CDS, (b) CDH and (c) PHA data shown at the top, respectively. The data PIs and BN output KPI using the MPV and the EV are shown at the bottom.

KPI using the most probable value (MPV) by (5.22) and the expected value (EV) by (5.21) shows that the CDH reflects a medium risk at most, because the PIs of CDH are the only ones indicating unhealthy conditions among all four types of PIs, which lack supporting evidence from PHA and PCCF. Similarly, Figure 5.12(b) shows a previous false alarm triggered by a sudden rise of PHA in the middle location. However, the PI of PHA is the only indication of an unhealthy condition such that the output MPV and EV are both lower than $j = 4$. The PIs of PCCF in Figure 5.12(c) suffer from the same lack of supporting evidences, although the time-domain PCCF have high amplitudes and the frequency-domain PIs are $j = 3$.

In contrast, Figure 5.13 shows three examples of previous hits that are also confirmed by the BN-based approach with the output MPV indicating a high or extreme risk. Figure 5.13(a) shows that an unhealthy PI of CDS is in itself a sufficient indication because it has and requires no supports as the only indicator in the lateral direction. For the unhealthy PIs of CDH and PHA in Figure 5.13(b) and (c), respectively, they are supported by the unhealthy PIs of PCCF, resulting in high or extreme risks at the corresponding locations. These results also suggest that to confirm whether an on-site verification is necessary, the MPVs should be checked instead of the EVs, which could be smaller than the MPVs due to averaging by probabilities.

Overall, the output of the BN-based approach is effective in reducing the number of potential defects and the false alarm rate. This result is the main merit of the approach that fuses all types of input data into an integrated KPI. Maintenance decisions made based on such a KPI can be more convincing and reliable compared with the current practice.

5.5.3. Comparison with alternative BN structures

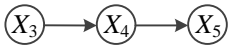
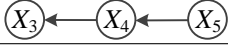
The proposed BN structure is crucial for the performance of the BN-based approach. The directed arcs in the structure establish a representation of the physical relations between the included dynamic data types of the catenary. Among all arcs, the two between variables CDH X_3 , PHA X_4 and PCCF X_5 are of great importance as correlated dynamic responses in the vertical direction. To show the effects of both arcs, two alternative structures between the three variables are applied to the same data for comparison. As presented in Table 5.4, alternative structure 1 cancels the arcs between the three variables, and alternative structure 2 reverses the directions of both arcs. The former ignores the physical relations between variables, whereas the latter reverses them.

The alternative BNs are estimated with the same historical data and applied to the new data. The detection results are given in Table 5.4. Among 132 potential defects from the original maintenance record, all BN structures identify a lower number of potential defects, showing the general effect of combining multiple data types. The proposed structure outputs the least number of potential defects that results in the lowest false alarm rate, and the structure with reverse arcs performs better than the one without any arc. This result is in line with theoretical analysis based on equations from (5.2) to (5.6), where the cause-effect relationships are found between the data of CDH, PHA and PCCF in the same manner. Therefore, it is necessary to not only establish the physical relations through arcs, but also set the arc directions in a physics-based manner considering the characteristics of data.

5.5.4. Tolerance against bad data

In practice, measurement data can be noisy or missing leading to inaccurate detection results. It is important to address these issues when the detection itself is methodologically difficult to achieve. Although the noisy data can be addressed by denoising techniques using on-board filtering devices or pre-processing procedures before data usage, the randomly missing data are not easy to address. The following discusses variations in the BN outputs based on the same inspection data used above.

Table 5.4: Results Comparison with Alternative BN Structures

BN structure	# of potential defects	False alarm rate
Proposed structure in Figure 5.2 	66	0.197
Alternative structure 1 	102	0.529
Alternative structure 2 	81	0.370
Original maintenance record	132	0.583

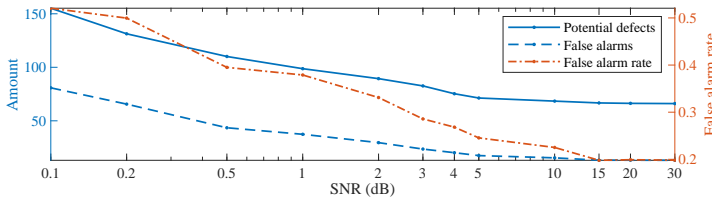


Figure 5.14: Detection results when the SNR of input data changes from 0.1 dB to 30 dB. The left vertical axis show the total amount of potential defects and false alarms while the right one shows the corresponding rate of false alarm.

Noisy data

The inspection data were pre-processed with high-frequency noises filtered out in all types of measurements except for speed. To test the performance of the BN outputs with general noisy input and the degree of noise tolerance, synthetic noises are added to the inspection data used as a noise-free reference. White noises resulting in a signal-to-noise ratio (SNR) ranging from 0.1 dB to 30 dB are added to the CDS, CDH, PHA and PCCF data before performing the data reconstruction. A lower SNR means stronger noises that are more likely to contaminate the detection results.

Figure 5.14 depicts the detection results using the BN-based approach when the input data contain noises. The statistics under a certain SNR are the average results of generating and adding random noises that satisfy the SNR for ten times. It can be observed that when the SNRs are greater than or equal to 15 dB, the results are almost identical to those of the noise-free data that output 66 potential defects and 19.7% false alarm rate. As the SNR decreases, both the amount of potential defects and false alarms increase, leading to increase of the false alarm rate up to 52.1%. Considering that the previous results output by the traditional method have 132 potential defects and a 58.3% false alarm rate, the proposed approach can be acceptable with the false alarm rate limited to below 30% when the SNR is greater than 3 dB. This ability to tolerate noise is due to the percentile-based extraction of PIs, which can mitigate the effects of noises. Nevertheless, it is still advisable to pre-process highly noisy data because there are sophisticated methods to improve signal SNRs from below 10 dB to higher.

Missing data

Missing data occur commonly and randomly during continuous measurements due to glitches in the measurement system. When only a few sampling points are missing in between recorded data, they can be interpolated based on the adjacent recorded data. However, this process introduces errors into the measurement data that can potentially lead to inaccurate detection results. When a temporary failure of a component in the measurement system occurs during inspections, it causes missing data over a much longer duration, a situation that is not suitable for interpolation. For the inference of the proposed BN, the output KPI can still be estimated if one or more types of input data are missing. In practice, it is unlikely that two or more types of data among the speed, CDS, CDH, PHA and PCCF are

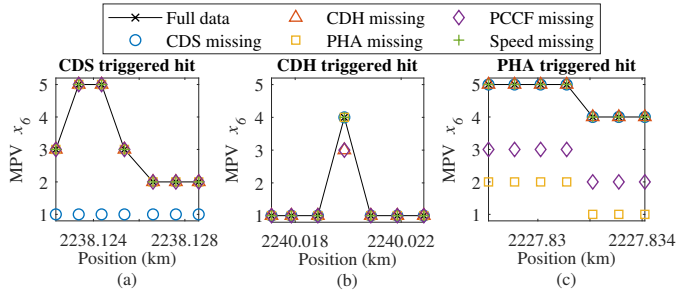


Figure 5.15: The output MPVs of three examples of hits when the data is complete and one type of data is missing. The hits were previously triggered by the (a) CDS, (b) CDH and (c) PHA data, respectively. The markers falling outside of the solid lines are deviated MPVs caused by the missing of corresponding data.

5

missing at the same time because of separately operating sensors and according to historical records. Thus, the performance of the BN-based approach is investigated when one type of missing data are encountered. The missing data are considered to cause the corresponding missing inputs (PIs) for the BN.

a) Short duration of missing data: The randomly missing short-duration data can be neglected unless the event occurs exactly when the pantograph is passes through a defect of the catenary. In such less likely cases, unhealthy PIs from the missing data are absent for the BN input. For the proposed BN, the missed CDS data are unfavorable because they are the only data measured in the lateral direction that indicate a lateral defect. The missing speed, CDH, PHA and PCCF data are comparatively less impactful, because the speed is not directly linked to the SCC, and the other three types of data are complementary to each other leading to the SCC. Concretely, Figure 5.15 depicts the output MPVs when one of the five types of data are missing for the three hits shown in Figure 5.13. Compared with the MPVs from complete data, Figure 5.15(a) shows that when the defect is reflected by the PI of CDS, only the missing CDS data cause the loss of hit, whereas other missing data minimally influence the output MPVs. In the vertical direction, Figure 5.15(b) shows that the missing CDH and PCCF data can falsely reduce the output MPVs, when the defect is reflected by the PI of CDH with the PI of PCCF as the main supporting evidence. The upside is that the unhealthy MPVs are not completely eliminated, as in the case missing CDS, which is the sole source of unhealthy PI in the lateral direction. For the same reason, Figure 5.15(c) shows that when the hit is triggered by the PI of PHA and supported by the PI of PCCF, the loss of PHA and PCCF reduces the MPVs compared with the MPVs from complete data.

b) Long duration of missing data: According to the record of inspection data from the high-speed line studied, this situation has occurred before, i.e., one type of measurement data is almost completely missing due to sudden component failures that could not be instantly fixed on a moving train. It is highly costly to run the inspection again, and thus making use of the incomplete data set is valuable to avoid wasting an inspection run entirely. Using the data shown in Figure 5.11 as an example, detection results based on the BN output when one of the five types

Table 5.5: Detection Results When One Type of Data is Completely Missing

Data	# of potential defects (MPV $x_6 \geq 4$)	# of hits	Hit rate
Complete	66	53	80.3%
Speed missing	66	52	78.8%
CDS missing	61	48	78.7%
CDH missing	59	50	84.7%
PHA missing	61	51	83.6%
PCCF missing	61	50	82.0%

of data is completely missing are obtained. In the case of missing speed, the data partition step (Step 2) in extraction of the BN input must be skipped. Table 5.5 presents the number of potential defects and hits identified by the output MPVs when handling long-duration missing data. It can be observed that when a certain type of data is completely missing, it consequently reduces the number of potential defects due to the loss of unhealthy PIs from that type of data. However, the missing CDH, PHA, or PCCF data do not largely reduce the number of hits, thus resulting in a higher hit rate at the price of overlooking several potential defects. At the same time, the potential defects overlooked by the missing CDS are all hits that are actually missed, leading to the lowest hit rate. The missing speed data minimally influence the results in this case, because the speed variation of the input data set is rather small. It is expected that the missing speed are more impactful when the speed changes frequently during an inspection.

In the undesired events of missing data, the BN-based approach can still estimate the output KPI of SCC, because it partially extracts and preserves the useful information of the incomplete data set to avoid the total waste of recorded data. Although the outputs are not completely satisfactory in terms of hit rate, especially when the CDS data are missing at defective locations, it is still a manageable situation for the proposed approach, considering that occurrences at the exact locations are few.

5.6. Conclusion

This study addresses practical problems in condition monitoring of the catenary in high-speed railway lines, including the underutilization of inspection data and the high false alarm rate in defect detection. A generic data-driven approach for improved catenary condition monitoring is proposed. The approach applies a new BN that fuses key information extracted from multiple types of inspection data into a sole KPI. The BN structure is established based on the physical relations between the data of speed, CDS, CDH, PHA and PCCF, which are all crucial data types for assessing the catenary condition. Tailored PIs that can properly reflect the catenary condition are defined and extracted from the CDS, CDH, PHA and PCCF according to their data characteristics resulting from the pantograph-catenary interaction. Using the four tailored PIs as the input of BN, the KPI that indicates the overall catenary

condition by considering all input PIs is defined as the BN output. In this way, the KPI can reflect all types of catenary defects causing abnormal dynamic responses in the four types of data. Based on the proposed BN, an approach to obtain the KPI for the comprehensive condition assessment of the catenary is presented.

To test the performance of the BN-based approach, the historical inspection data and maintenance records from a section of the China Beijing–Guangzhou high-speed railway line in the past three years are used as an example. Preliminary results show that with the BN-based approach, the BN outputs from new inspection data can significantly reduce the false alarm rate by up to 66.2%, thus increasing the hit rate for defect detection. In addition, the effectiveness of the proposed BN is proven by outperforming the alternative BN structures with the same input. Furthermore, the approach is also feasible when the input data quality is poor by acceptably tolerating noisy data with a SNR higher than 3 dB or one type of data occasionally missing in inspections.

To further develop the proposed approach, four major improvements can be considered. The first improvement is inclusion of additional data types in the BN structure, such as geometrical data and images, such that the BN output is more comprehensive by covering a wider range of PIs of the catenary. The second one is expansion of the BN output into indicators for specific types of defects such that defect classification can be achieved following detection. The third one is application of automatic feature identification and extraction techniques such as deep learning to define PIs that are beneficial for defect classification. The final one is updating of the BN parameters that consider the different degradation stages in the full service life of the catenary, potentially with a dynamic BN. These improvements require notably large amounts of data and information accumulated from a long-term periodic inspection. To implement this approach for a catenary in practice, it is important to first decide on the monitored data types and thus the BN structure, and the selected measurement data and maintenance records of the catenary should be stored in a manner that is easily traceable through geographic locations or distance marks along the rail.

References

- [1] X. Gibert, V. M. Patel, and R. Chellappa, *Deep multitask learning for railway track inspection*, [IEEE Transactions on Intelligent Transportation Systems](#) **18**, 153 (2017).
- [2] M. Molodova, Z. Li, A. Núñez, and R. Dollevoet, *Automatic detection of squats in railway infrastructure*, [IEEE Transactions on Intelligent Transportation Systems](#) **15**, 1980 (Mar. 2014).
- [3] J. S. Lee, S. Choi, S.-S. Kim, C. Park, and Y. G. Kim, *A mixed filtering approach for track condition monitoring using accelerometers on the axle box and bogie*, [IEEE Transactions on Instrumentation and Measurement](#) **61**, 749 (2012).
- [4] S. Kusumi, T. Fukutani, and K. Nezu, *Diagnosis of overhead contact line based on contact force*, [Quarterly Report of RTRI](#) **47**, 39 (2006).
- [5] O. Bruno, A. Landi, M. Papi, and L. Sani, *Phototube sensor for monitoring the quality of current collection on overhead electrified railways*, [Proceedings of the institution of mechanical engineers, part f: Journal of rail and rapid transit](#) **215**, 231 (2001).
- [6] I. Aydin, M. Karakose, and E. Akin, *Anomaly detection using a modified kernel-based tracking in the pantograph–catenary system*, [Expert Systems with Applications](#) **42**, 938 (2015).
- [7] J. Leander, A. Andersson, and R. Karoumi, *Monitoring and enhanced fatigue evaluation of a steel railway bridge*, [Engineering Structures](#) **32**, 854 (2010).
- [8] E. Fridell, M. Ferm, and A. Ekberg, *Emissions of particulate matters from railways—emission factors and condition monitoring*, [Transportation Research Part D: Transport and Environment](#) **15**, 240 (2010).
- [9] M. Givoni, *Development and impact of the modern high-speed train: A review*, [Transport reviews](#) **26**, 593 (2006).
- [10] A. Collina, F. Fossati, M. Papi, and F. Resta, *Impact of overhead line irregularity on current collection and diagnostics based on the measurement of pantograph dynamics*, [Proceedings of the Institution of Mechanical Engineers, Part F: Journal of Rail and Rapid Transit](#) **221**, 547 (2007).
- [11] *Railway applications—current collection systems—technical criteria for the interaction between pantograph and overhead line*, (2012).
- [12] *Overall technical specifications of high-speed railway power supply safety inspection and monitoring system (6c system)*, (2012).
- [13] M. Carnevale and A. Collina, *Processing of collector acceleration data for condition-based monitoring of overhead lines*, [Proceedings of the Institution of Mechanical Engineers, Part F: Journal of Rail and Rapid Transit](#) **230**, 472 (2016).

- [14] D. Zhan, D. Jing, M. Wu, D. Zhang, L. Yu, and T. Chen, *An accurate and efficient vision measurement approach for railway catenary geometry parameters*, *IEEE Transactions on Instrumentation and Measurement* (2018), 10.1109/TIM.2018.2830862.
- [15] P. Boffi, G. Cattaneo, L. Amoriello, A. Barberis, G. Bucca, M. F. Bocciolone, A. Collina, and M. Martinelli, *Optical fiber sensors to measure collector performance in the pantograph-catenary interaction*, *IEEE Sensors Journal* **9**, 635 (2009).
- [16] E. Karakose, M. T. Gencoglu, M. Karakose, I. Aydin, and E. Akin, *A new experimental approach using image processing-based tracking for an efficient fault diagnosis in pantograph–catenary systems*, *IEEE Transactions on Industrial Informatics* **13**, 635 (2017).
- [17] C. J. Cho and H. Ko, *Video-based dynamic stagger measurement of railway overhead power lines using rotation-invariant feature matching*, *IEEE Transactions on Intelligent Transportation Systems* **16**, 1294 (2015).
- [18] S. Bruni, G. Bucca, M. Carnevale, A. Collina, and A. Facchinetti, *Pantograph–catenary interaction: recent achievements and future research challenges*, *International Journal of Rail Transportation* **6**, 57 (2018).
- [19] Z. Liu, Y. Song, Y. Han, H. Wang, J. Zhang, and Z. Han, *Advances of research on high-speed railway catenary*, *Journal of Modern Transportation* **26**, 1 (2018).
- [20] Z. Liu, L. Wang, C. Li, and Z. Han, *A high-precision loose strands diagnosis approach for isoelectric line in high-speed railway*, *IEEE Transactions on Industrial Informatics* **14**, 1067 (2018).
- [21] J. Chen, Z. Liu, H. Wang, A. Núñez, and Z. Han, *Automatic defect detection of fasteners on the catenary support device using deep convolutional neural network*, *IEEE Transactions on Instrumentation and Measurement* **67**, 257 (2018).
- [22] G. Kang, S. Gao, L. Yu, and D. Zhang, *Deep architecture for high-speed railway insulator surface defect detection: Denoising autoencoder with multitask learning*, *IEEE Transactions on Instrumentation and Measurement* (2018), 10.1109/TIM.2018.2868490.
- [23] H. Wang, Z. Liu, Y. Song, X. Lu, Z. Han, J. Zhang, and Y. Wang, *Detection of contact wire irregularities using a quadratic time–frequency representation of the pantograph–catenary contact force*, *IEEE Transactions on Instrumentation and Measurement* **65**, 1385 (2016).
- [24] Z. Liu, H. Wang, R. Dollevoet, Y. Song, A. Núñez, and J. Zhang, *Ensemble emd-based automatic extraction of the catenary structure wavelength from the pantograph–catenary contact force*, *IEEE Transactions on Instrumentation and Measurement* **65**, 2272 (Jun. 2016).

- [25] H. Wang, A. Núñez, Z. Liu, Y. Song, F. Duan, and R. Dollevoet, *Analysis of the evolvement of contact wire wear irregularity in railway catenary based on historical data*, *Vehicle System Dynamics* **56**, 1207 (2018).
- [26] H. Wang, A. Núñez, Z. Liu, and R. Dollevoet, *Entropy-based local irregularity detection for high-speed railway catenaries with frequent inspections*, *IEEE Transactions on Instrumentation and Measurement* **68**, 3536 (2018).
- [27] R. Zhao, R. Yan, Z. Chen, K. Mao, P. Wang, and R. X. Gao, *Deep learning and its applications to machine health monitoring*, *Mechanical Systems and Signal Processing* **115**, 213 (2019).
- [28] S.-D. Wu, C.-W. Wu, T.-Y. Wu, and C.-C. Wang, *Multi-scale analysis based ball bearing defect diagnostics using mahalanobis distance and support vector machine*, *Entropy* **15**, 416 (2013).
- [29] T. W. Rauber, F. de Assis Boldt, and F. M. Varejão, *Heterogeneous feature models and feature selection applied to bearing fault diagnosis*, *IEEE Transactions on Industrial Electronics* **62**, 637 (2015).
- [30] M. Žvokelj, S. Zupan, and I. Prebil, *Multivariate and multiscale monitoring of large-size low-speed bearings using ensemble empirical mode decomposition method combined with principal component analysis*, *Mechanical Systems and Signal Processing* **24**, 1049 (2010).
- [31] A. Jamshidi, S. Hajizadeh, Z. Su, M. Naeimi, A. Núñez, R. Dollevoet, B. De Schutter, and Z. Li, *A decision support approach for condition-based maintenance of rails based on big data analysis*, *Transportation Research Part C: Emerging Technologies* **95**, 185 (2018).
- [32] G. Lederman, S. Chen, J. H. Garrett, J. Kovačević, H. Y. Noh, and J. Bielak, *A data fusion approach for track monitoring from multiple in-service trains*, *Mechanical Systems and Signal Processing* **95**, 363 (2017).
- [33] G. Wang, T. Xu, T. Tang, T. Yuan, and H. Wang, *A bayesian network model for prediction of weather-related failures in railway turnout systems*, *Expert systems with applications* **69**, 247 (2017).
- [34] Z. Yongli, H. Limin, and L. Jinling, *Bayesian networks-based approach for power systems fault diagnosis*, *IEEE Transactions on Power Delivery* **21**, 634 (2006).
- [35] F. Sahin, M. Ç. Yavuz, Z. Arnavut, and Ö. Uluyol, *Fault diagnosis for airplane engines using bayesian networks and distributed particle swarm optimization*, *Parallel Computing* **33**, 124 (2007).
- [36] B. Cai, Y. Liu, Q. Fan, Y. Zhang, Z. Liu, S. Yu, and R. Ji, *Multi-source information fusion based fault diagnosis of ground-source heat pump using bayesian network*, *Applied energy* **114**, 1 (2014).

- [37] N. Friedman, D. Geiger, and M. Goldszmidt, *Bayesian network classifiers*, *Machine learning* **29**, 131 (1997).
- [38] H. Wang, A. Núñez, R. Dollevoet, Z. Liu, and J. Chen, *Intelligent condition monitoring of railway catenary systems: A bayesian network approach*, in *Dynamics of Vehicles on Roads and Tracks Vol 2: Proceedings of the 25th International Symposium on Dynamics of Vehicles on Roads and Tracks (IAVSD 2017), 14-18 August 2017, Rockhampton, Queensland, Australia* (CRC Press, 2017) p. 663.
- [39] T. D. Nielsen and F. V. Jensen, *Bayesian networks and decision graphs* (Springer Science & Business Media, 2009).
- [40] I. Ben-Gal, *Bayesian networks*, *Encyclopedia of statistics in quality and reliability* **1** (2008).
- [41] D. Tobon-Mejia, K. Medjaher, and N. Zerhouni, *Cnc machine tool's wear diagnostic and prognostic by using dynamic bayesian networks*, *Mechanical Systems and Signal Processing* **28**, 167 (2012).
- [42] C. Chen, X. Liu, H.-H. Chen, M. Li, and L. Zhao, *A rear-end collision risk evaluation and control scheme using a bayesian network model*, *IEEE Transactions on Intelligent Transportation Systems* (2018), 10.1109/TITS.2018.2813364.
- [43] S. Sun, C. Zhang, and G. Yu, *A bayesian network approach to traffic flow forecasting*, *IEEE Transactions on Intelligent Transportation Systems* **7**, 124 (2006).
- [44] N. Friedman, *The bayesian structural em algorithm*, in *Proceedings of the Fourteenth conference on Uncertainty in artificial intelligence* (Morgan Kaufmann Publishers Inc., 1998) pp. 129–138.
- [45] C. Andrieu, N. De Freitas, A. Doucet, and M. I. Jordan, *An introduction to mcmc for machine learning*, *Machine learning* **50**, 5 (2003).
- [46] *Railway applications—current collection systems—requirements for and validation of measurements of the dynamic interaction between pantograph and overhead contact line*, (2012).
- [47] *Railway applications—current collection systems—requirements for and validation of measurements of the dynamic interaction between pantograph and overhead contact line*, (2016).
- [48] N. E. Huang, Z. Shen, S. R. Long, M. C. Wu, H. H. Shih, Q. Zheng, N.-C. Yen, C. C. Tung, and H. H. Liu, *The empirical mode decomposition and the hilbert spectrum for nonlinear and non-stationary time series analysis*, *Proceedings of the Royal Society of London. Series A: Mathematical, Physical and Engineering Sciences* **454**, 903 (1998).

6

Conclusions and recommendations

This chapter concludes the scientific and technical implications for society of the research findings in this dissertation.

This dissertation is motivated by challenges in developing data-based approaches to improve the dynamic condition assessment of catenary using condition monitoring data of the main dynamic parameters of catenary, including the pantograph-catenary contact force, the pantograph head acceleration and the dynamic height and stagger of contact wire. The research objectives outlined in Chapter 1 include defining performance indicators (PIs) based on measurement data of the catenary dynamic parameters, developing adaptive approaches to extract the defined PIs from data, acquiring the relationship between the dynamic parameters and the existing and degrading contact wire irregularities, and developing data-based approaches for assessing the dynamic catenary condition. Several research questions are posed to achieve the research objectives. Answers to the questions are elaborated throughout Chapters 2-5, which are summarized in this chapter. Based on the main findings and their implications, future research directions and industrial applications are recommended.

6.1. Conclusions

This section summarizes the main findings answering the six research questions as follows:

1. *What types of PIs based on the measurement data of catenary dynamic parameters are suitable for the condition assessment of catenary?*

In this dissertation, four main dynamic parameters of catenary, namely the pantograph-catenary contact force (Chapter 2 and 5), pantograph head vertical acceleration (Chapter 3 and 5), dynamic contact wire height and stagger (Chapter 5) are considered for defining PIs of catenary. The data-based PIs are respectively defined according to the different dynamic characteristics of the parameters. To best assess the catenary condition, it is found that

- Time-domain PIs based on data statistics, including the maximum, minimum and standard deviation, can directly indicate local defects or irregularities that cause an impact in the pantograph-catenary interaction or the detachment of pantograph-catenary contact. They are suitable for detecting advanced catenary defects that are already affecting the current collection quality.
- Frequency-domain PIs based on the Fourier transform, power spectrum density, wavelet transform, Hilbert-Huang transform and their variants can reflect frequency contents of the parameters and show the normal and abnormal frequency responses in the pantograph-catenary interaction. Compared with time-domain PIs, they can indicate early-stage defects, which have a limited impact on the pantograph-catenary interaction and cannot be reflected by time-domain PIs.
- The pantograph-catenary contact force and pantograph head vertical acceleration generally contain more frequency contents in terms of vibration modes than the dynamic contact wire height and stagger. It is thus preferred to define frequency-domain PIs using the force and acceleration to make use of the

rich frequency contents. This helps to identify the type of defect measured based on the indicative frequency of different defect type.

Both time- and frequency-domain PIs are important for monitoring the degradation of catenary and timely identifying existing defects. A combination of PIs are expected to be employed in practice so that existing defects, regardless of their stages, will not be overlooked. Nevertheless, frequency-domain PIs should be paid more attention as it is preferred to detect defects at an early stage.

2. Which PIs are adaptive to the differences contained in the measurement data of dynamic parameters?

As stated by the last challenge in Chapter 1, both time- and frequency-domain PIs are subject to various differences affecting the amplitude and frequency of measurement data, such as the different catenary structure, pantograph type and train speed. It is thus important to define PIs that are adaptive to the measurement data rather than constantly adjusting the PIs according to the data handled. This makes the PIs more applicable for various catenary structures inspected under different circumstances. In this context, this dissertation proposes the concept of catenary structure wavelength (CSW):

- A CSW is an intrinsic wavelength component contained in the main dynamic parameters of catenary, including the pantograph-catenary contact force (Chapter 2) and the pantograph head vertical acceleration (Chapter 3). It is caused by the periodic variations of contact wire stiffness attributed to the cyclic structure of catenary that must regulate the height of contact wire in every spans and interdropper distances. This wavelength is fixed and determined by the catenary structure itself, which will not change with the pantograph type used or train speed during measurements. For a force or acceleration signal, the sum of such CSWs corresponding to the wavelengths of span and interdropper distance are regarded as an extracted signal of CSWs from the original signal. The residual signal excluding the CSWs from the original signal is regarded as the non-CSW signal.

Based on the CSWs and non-CSW signal that are inherently adaptive to the differences in measurement data, the following PIs inheriting the adaptability are proposed:

- In Chapter 2, the mean and standard deviation of the CSWs of pantograph-catenary contact force are proposed to indicate the condition of the main catenary structural parameters.
- In Chapter 2, the quadratic time-frequency representation of the non-CSW signal of contact force is proposed for detecting the local irregularities of contact wire.
- In Chapter 3, the wavelet packet entropy of the CSWs and non-CSW signal of pantograph head acceleration is proposed. The entropy of CSWs is used for detecting contact wire irregularities with a length longer than 5 m, while the entropy of non-CSW signal is for the short-length local irregularities.

- In Chapter 5, PIs based on the dynamic contact wire height and stagger are defined as condition levels ranking from risk free to extreme risk. The condition levels are decided based on a percentile-based data clustering approach. The measurement data of height or stagger are first divided into different speed levels to eliminate the influence of speed variation during measurements. Then, the data at each speed level is clustered into groups based on the percentile intervals defined to distinguish the data close to and far away from the median value. The groups far away from the median value indicate where excessive contact wire displacement in the vertical and lateral directions happened. Similarly, PIs based on the contact force and acceleration are defined as condition levels clustered using the percentiles of the CSWs and non-CSW signals. These PIs can be employed separately for catenary condition assessment when only one type of data is available. They can also be combined together to form an integrated PI as introduced next.
- In Chapter 5, an integrated PI is proposed combining the PIs extracted from the four types of dynamic parameters. It is defined as the overall level of catenary condition by considering all types of defect that could lead to abnormal PIs of the four types of dynamic parameters. To unify the condition levels of catenary when having different defect types, a new paradigm to convert defect types into a unified overall catenary condition level is proposed to obtain the integrated PI.

It is shown that the proposed PIs are adaptive to the variations of catenary structure, pantograph type and train speed. This is because the PIs are defined based on the CSWs and non-CSW signal that are inherent components of the measurement data changing with the variations. The extraction of CSWs and non-CSW signal is realized by the first data processing approach summarized in the next question.

3. How to adaptively extract the PIs from the measurement data?

The proposed PIs are adaptively extracted by three new data processing approaches summarized as follows:

- The first approach can extract the CSWs and non-CSW signal from both the pantograph-catenary contact force and pantograph head vertical acceleration. The approach is proposed in Chapter 2 and employed in Chapter 3 and 5. It is developed using the empirical mode decomposition [1] or its variants to first decompose the contact force or acceleration signal into several intrinsic mode functions (IMFs). Then, the IMFs are identified as CSWs or non-CSW components. The IMFs having a dominant wavelength within the ranges of [40 m, 70 m] and [4 m, 10 m], which correspond respectively to the span lengths and inter-dropper distances, are considered to be CSWs. Finally, the CSWs and non-CSW signal are obtained by summing the identified CSWs and non-CSW IMFs. The CSWs are the dominant components of the contact force or acceleration reflecting the state of the main catenary structure. In contrast, the non-CSW signal contains the dynamic responses caused by fac-

tors other than the main catenary structure, making it suitable for indicating catenary defects, especially local ones.

- The second approach is proposed for extracting PIs from the measurement data of four types of dynamic parameters in Chapter 5, namely the pantograph-catenary contact force, pantograph head vertical acceleration and dynamic contact wire height and stagger. The historical data applied to this approach require to be measured from the same railway line to eliminate the influence of structural differences. As introduced before, the measurement data are first clustered into groups based on the data percentiles. Then, condition levels are assigned to the clustered data with the data close to the median considering as healthy and those deviated the farthest from the median as extreme risks. In this way, the approach is adaptive for all types measurement data, while historical data containing health and unhealthy samples are included for PI extraction.
- The last approach outputs automatically an integrated PI through the inference of a Bayesian network [2] proposed for catenary condition assessment. The Bayesian network establishes a probabilistic relationship between the PIs extracted from the four types of dynamic parameters and the integrated PI using historical data and on-site verification records. By inputting PIs extracted from new data, the integrated PI can be inferred through the probabilistic relationship, which indicates the catenary condition more accurately and comprehensively owing to the inclusion of multiple data types and on-site verifications performed in the past.

In addition to the performances of adaptive PI extraction, the first approach can still be feasible when the input data is contaminated by measurement noise resulting in a signal-to-noise ratio higher than 5 dB in the cases presented in Chapter 2. Similarly, in the cases presented in Chapter 5, the last approach can tolerate noisy data with a signal-to-noise ratio higher than 3 dB. It can also work acceptably when one type of the input data is intermittently missing, owing to the supplementary PIs provided by the other three types of data.

4. *How is the contact wire irregularity affecting the pantograph-catenary interaction?*

Through analyzing simulation results and measurement data, it is found that the contact wire irregularity has a direct impact on the pantograph-catenary interaction. It is crucial to identify when the impact caused by the irregularity is unacceptable and thus the catenary should be maintained. The following findings can help to define the level of impact using the proposed PIs:

- In Chapter 2, the standard deviation and local maximum of the non-CSW signal of contact force shows that the distributed and local contact wire irregularity can induce impacts in the pantograph-catenary interaction, leading to undesired oscillation of contact force. The contact wire height irregularity with an amplitude of 8 mm can cause considerable increase in the standard deviation.

- In Chapter 2, the quadratic time-frequency representation of the non-CSW signal of contact force shows that the contact wire irregularity having a certain wavelength can induce the dynamic response with the same wavelength in contact force. The energy of time-frequency representation at the induced wavelength is higher when the amplitude of the irregularity is higher. The energy peak is observable before the standard deviation or maximum of contact force could reveal.
- In Chapter 3, using the wavelet packet entropy of the CSWs and non-CSW signal of pantograph head vertical acceleration, it is found that the contact wire irregularity, regardless of its scale in length, can cause repetitive impact to the pantograph, but it may not affect every pantograph passage. This phenomenon indicates that assessment based on a single measurement may be unreliable.
- In Chapter 4, it is found that the wear irregularity of contact wire has certain impact on the pantograph - catenary contact force. Although it can hardly deviate the mean of contact force, it can increase the standard deviation of contact force by 5.7% when the wear irregularity has an average wire thickness loss of about 1.5 mm.
- In Chapter 5, by comparing multiple types of dynamic parameter measured simultaneously, it is found that in some cases the contact wire irregularity only affects the measurement data of one or several dynamic parameters. Thus, it is helpful to combine multiple parameters for catenary condition assessment rather than using only the contact force or acceleration.

6

5. *How is the contact wire irregularity evolving with the effects of pantograph-catenary interaction?*

This question is also investigated through both simulations and measurements. The following findings help to predict the evolvement of contact wire irregularity:

- A catenary with the contact wire irregularity at a certain wavelength tends to deteriorate faster than other parts of the catenary, because the irregularity worsens the pantograph-catenary interaction by inducing vibrations at the same wavelength (Chapter 2, 3 and 5).
- The formation of contact wire wear irregularity is mainly associated with the catenary structure. It is found that the wear irregularity contains structural wavelengths of catenary such as span lengths and inter-dropper distances. Because the catenary structure is fixed, the degree of irregularity at the structural wavelengths will deteriorate over time. Due to the fixing effect at the registration arms, contact wire clamped at or near the registration arms are likely to suffer severe wear (Chapter 4).
- The wear irregularity of contact wire tends to grow and spread toward in the common or dominant running direction of trains in the specific line. It is thus

expected that the wear irregularity at the beginning of a tension (anchoring) section is worse than that at the end of the section (Chapter 4).

6. How to assess the catenary condition using the data-based PIs?

The following approaches are developed for catenary condition assessment using the proposed PIs:

- In Chapter 2, an approach to detect contact wire irregularities using the measurement data of contact force is presented. The quadratic time-frequency representation of the CSWs and non-CSW signal of contact force is employed as the PI. The baselines of PIs are established using simulation data or historical measurement data, so that emerging contact wire irregularities can be recognized by the growing or new energy peaks. The approach can output the wavelength and position of the detected irregularity based on the location and duration of energy peaks in the time-frequency representation.
- In Chapter 3, an approach to detect and verify contact wire irregularities using the measurement of pantograph head vertical acceleration from frequent inspections is proposed. This approach employs the wavelet packet entropy of the CSWs and non-CSW signal of acceleration as the PIs. A moving window strategy is proposed to detect irregularities with different scales in length. When the gradient of entropy is too high, an irregularity is detected and regarded as a potential one. To verify the potential irregularity, the gradient of entropy at the same location is examined for repeatability in the following five inspections. An irregularity is considered as verified only if three out of six inspections show the potential irregularity at the same location. In this way, maintenance resources can be allocated to verified detection results to save cost and time.
- In Chapter 5, a data-driven approach based on the Bayesian network to assess the overall catenary condition is proposed. The approach employs PIs extracted from the four types of dynamic parameters of catenary using percentile-based clustering as the input. It automatically outputs the overall condition level of catenary considered to be an integration of the input PIs. The integrated PI thus could indicate all catenary defects that can lead to abnormal measurement data of the dynamic parameters. It can not only cover a wide range of catenary defects, but also easily apply to practice as the sole PI for catenary.

6.2. Recommendations

6.2.1. Future research

Inspired by the research and conclusions of this dissertation, this section identifies several research directions as extensions or innovations. The aim is to improve the performances of new and existing catenary through research. There are basically two aspects of research recommended for the future:

- Optimizing the structural design of catenary, especially for the catenary of high-speed lines and the speed upgrade of existing catenary.
- Developing diagnostic and prognostic condition assessment approaches for catenary to support the planned and predictive maintenance of catenary.

Concretely, the following research directions can be explored:

1. The structural parameters and design of catenary can be optimized through simulations or hybrid simulations [3, 4] to change the stiffness distribution of contact wire and wave propagation pattern of catenary, and thus find parameters that best fit the pantograph type and operation speed of the targeted railway line.
2. The reliability of catenary under extreme weather conditions is a major concern for some areas. Research to facilitate the anti-wind [5, 6] and anti-icing [7, 8] design of catenary should be considered.
3. The active control of pantograph is a solution to mitigate the vibration of pantograph-catenary interaction [9–11]. The current research challenges include improving the prediction of contact force and the actuation of pantograph. This could potentially enable a higher operation speed, while ensuring a good current collecting quality and mitigating the wear of contact wire and pantograph.
4. The complete definition of catenary defects is still an ongoing process. It includes defining the type, initiation, growth and effect of defects observed in practice. This helps to determine the proper way to monitor the defects and prevent failures.
5. As an extension of this research, the type of catenary defect causing contact wire irregularities can be recognized using the proposed PIs and the identified wavelength of irregularity. To this end, a relationship between the defect type and the indicators should be found and established.
6. Online monitoring methods using sensors to measure, for example, the contact wire vibration whenever a pantograph passes can be developed and implemented to monitor the catenary condition at some critical and vulnerable locations. This also contributes to the observation of catenary degradation over time.
7. Prognostic methods for catenary should be developed using the degradation pattern of catenary observed and extracted from historical data. Although this is a relatively new research area for the catenary, attempts using the fuzzy logic, rough set, Kalman filter and machine learning are expected [12]. This is also an ongoing process as the data collected for catenary are still accumulating to provide a sufficient data source.

8. The rapidly developing big data analytics can also benefit the condition assessment of catenary. The process from PI definition and extraction to defect identification, classification and prediction can be automatically or even autonomously accomplished through data mining and deep learning approaches. When dealing with multiple data sources including not only vibration signals, but also images or videos, 3D signals, infrared signals and ultrasound signals, data fusion techniques can integrate the data sources to assess the catenary condition more accurately and comprehensively.

6.2.2. Future practice

To reduce the life cycle cost of catenary and the number of train service disruptions caused by catenary failures, the ideal maintenance strategy should include more planned and predictive maintenances instead of reactive ones. The following measures are advised for railway industry to achieve the transition of maintenance strategy:

1. To prevent catenary failures, it is necessary to employ periodical inspections to monitor the catenary condition and detect critical defects that could lead to failures. This is an essential prerequisite to apply the proposed approaches in practice.
2. The dynamic parameters of catenary, particularly the pantograph-catenary contact force, are recommended to be measured in inspections. This enables the detection of a wider range of defects compared with the inspection of geometric parameters.
3. Frequency-domain PIs, such as the PIs proposed in this dissertation, are crucial for identifying the type and severity of catenary defects.
4. The measurement frequency for the contact force and pantograph acceleration should be increased to higher than 200 Hz so that the local defects of catenary will not be overlooked in inspections.
5. Instead of using a fixed inspection frequency, the interval between inspections should be adjustable depending on the degradation rate of catenary estimated based on the trend of PIs from previous inspections.
6. The development of diagnostic and prognostic assessment approaches highly relies on information extracted from historical data and maintenance or validation records. It is thus important to format and store the data and records in a manner that can be easily tracked and retrieved.
7. Planned and predictive maintenance decisions for catenary should be made based on a ranking of the criticality or risk of the detected defects. This requires not only a quantification of defect severity using the proposed PIs, but also estimations of the failure probability due to the defect and the consequences of such a failure.

References

- [1] N. E. Huang, Z. Shen, S. R. Long, M. C. Wu, H. H. Shih, Q. Zheng, N.-C. Yen, C. C. Tung, and H. H. Liu, *The empirical mode decomposition and the hilbert spectrum for nonlinear and non-stationary time series analysis*, *Proceedings of the Royal Society of London. Series A: Mathematical, Physical and Engineering Sciences* **454**, 903 (1998).
- [2] T. D. Nielsen and F. V. Jensen, *Bayesian networks and decision graphs* (Springer Science & Business Media, 2009).
- [3] A. Facchinetti and S. Bruni, *Hardware-in-the-loop hybrid simulation of pantograph–catenary interaction*, *Journal of Sound and Vibration* **331**, 2783 (2012).
- [4] W. Zhang, G. Mei, X. Wu, and Z. Shen, *Hybrid simulation of dynamics for the pantograph–catenary system*, *Vehicle System Dynamics* **38**, 393 (2002).
- [5] Y. Song, Z. Liu, H. Wang, J. Zhang, X. Lu, and F. Duan, *Analysis of the galloping behaviour of an electrified railway overhead contact line using the non-linear finite element method*, *Proceedings of the Institution of Mechanical Engineers, Part F: Journal of Rail and Rapid Transit* **232**, 2339 (2018).
- [6] Y. Song, Z. Liu, H. Wang, X. Lu, and J. Zhang, *Nonlinear analysis of wind-induced vibration of high-speed railway catenary and its influence on pantograph–catenary interaction*, *Vehicle System Dynamics* **54**, 723 (2016).
- [7] E. Cinieri and A. Fumi, *Deicing of the contact lines of the high-speed electric railways: Deicing configurations. experimental test results*, *IEEE Transactions on Power Delivery* **29**, 2580 (2014).
- [8] L. Guo, L. Zhou, M. Chen, and W. Huang, *Online catenary anti-icing technique for electric railways employing direct feeding systems*, *IET Generation, Transmission & Distribution* **10**, 1969 (2016).
- [9] T. Wu and M. Brennan, *Active vibration control of a railway pantograph*, *Proceedings of the Institution of Mechanical Engineers, Part F: Journal of Rail and Rapid Transit* **211**, 117 (1997).
- [10] G. Diana, F. Fossati, and F. Resta, *High speed railway: collecting pantographs active control and overhead lines diagnostic solutions*, *Vehicle System Dynamics* **30**, 69 (1998).
- [11] X. Lu, Z. Liu, J. Zhang, H. Wang, Y. Song, and F. Duan, *Prior-information-based finite-frequency H_∞ control for active double pantograph in high-speed railway*, *IEEE Transactions on Vehicular Technology* **66**, 8723 (2017).
- [12] J. Lee, F. Wu, W. Zhao, M. Ghaffari, L. Liao, and D. Siegel, *Prognostics and health management design for rotary machinery systems—reviews, methodology and applications*, *Mechanical systems and signal processing* **42**, 314 (2014).

Acknowledgements 致谢

Pursuing a PhD was a simple decision for me because I did not like the jobs I could find when I was a master student in China. Although I was overall confident along the way, there were moments of doubt and struggle. Luckily, I always have the help and support of my family, friends, and colleagues. Therefore I would like to thank all of you.

It all started in 2014 when I contacted Mr. Cees Timmers for my application of visiting researcher at TU Delft. I would like to thank Prof. Zili Li for arranging an interview with Prof. Rolf Dollevoet and me after he was informed about my application. I was surprised that both Zili and Rolf were coincidentally visiting Southwest Jiaotong University in Chengdu and we could actually do the interview in person. On 29 October 2014, Zili and Rolf interviewed me in the lobby of a hotel that they were staying in. It was my first conversation done in English which lasted from 10 pm to passing midnight, probably because I was talking and reacting slow. Little did I know that Rolf will become my PhD promotor in the future.

I would like to express my sincere gratitude to my promotor, Prof. Rolf Dollevoet. You supported my transition from a visiting researcher to a PhD student under your supervision. You trusted me for finishing my PhD in three years. You guided me to solve practical problems and improve my papers. You offered me a postdoc position so I can continue with my research. I am glad that I did not let you down.

I am indebted to my co-promotor and daily supervisor, Dr. Alfredo Núñez Vicensio. Alfredo, when I first arrived at TU Delft, I sent you an email hoping to talk about big data in railway maintenance. It turned out to be the best decision I made for my PhD. Without you, I would not be the person I am. You know perfectly how and when to stimulate me to proceed and improve in my PhD and future careers. I cannot think of a better supervisor for me other than you. Your heartfelt support, encouragement, and advice are the treasures of my life.

I am deeply grateful for the continuous support I received from my old colleagues at Southwest Jiaotong University. Prof. Zhigang Liu introduced railway research to me and has been supporting my research since 2012. Dr. Zhiwei Han helped me to develop my first simulation model. Dr. Yang Song fought with me through the most difficult stage at the beginning of our pantograph and catenary research. Dr. Xiaobing Lu and Fuchuan Duan are wonderful research collaborators. Thank you all for bringing me research inspirations.

I would like to thank the former and present staff members in our railway engineering section. Prof. Zili Li, thank you for helping me in many administrative matters and your constructive insights about my research. Ellard Groenewegen, thank you for all the fruitful discussions of research and project. You selflessly and carefully translated my dissertation summary into Dutch, which in turn improved my

English summary. Harm Visser, thank you for patiently introducing the Dutch culture and railway to me at the beginning of my PhD. Evert van Veldhuizen, thank you for all the inspiring discussions on catenary research. Jurjen Hendriks, thank you for sharing your valuable knowledge and suggestions about measurement systems, data processing, project, and my Dutch summary. Jacqueline Barnhoorn, thank you for helping me in countless matters that greatly facilitates my work in the past years and now. Sandra Ransdorp, thank you for handling issues with my postdoc position. Dr. Zhiwei Qian, thank you for sharing your interesting and useful knowledge and experiences about life in the Netherlands. Joris, thank you for arranging my office access when I first arrived at TU Delft. It is also my pleasure to work with my colleagues Valeri Markine, Jan Moraal, Chang Ling, Ruud van Bezooijen, Greg Lambert, Dirk Doedens, Ivan Ramirez Fonseca, and Behzad Hajizad.

I am grateful to be accompanied by my fellow PhD candidates and visiting students/scholars on this journey. Dr. Ali Jamshidi, I enjoyed working with you on multi-disciplinary topics and thank you for your recommendations of jobs. Chen Shen, I do hope that our company can become a reality someday. Xiangming Liu, your spontaneous humor and infectious laughter lighten up my work mood. Pan Zhang, thank you for making my life easier by organizing a union of takeaways. My PhD life was colourful and joyful thanks to my kind and warm friends Leilei Miao & Chen Shen & Yirui Shen, Xiao Liang & Qu Hu, Yan Zhou & Zilong Wei, Lin Xiao & Zhen Yang & Jin Yang, Lan Song & Yaqing Shu & Yufeng Shu & Yuyao Shu, Yanyan Sun & Meng Wang & Kaka & Alice, Shaoguang Li, Xiangyun Deng, Anthonie Boogaard, Dongya Ren, Lizuo Xin, Omid Hajizad, Meysam Naeimi, Yuewei Ma, Haoyu Wang, Yang Jin, Wenqiang Liu, Li Wang, Siwarak Unsiwilai, Yunlong Guo, Wenli Jia, Julian He, Bin Zhu, Tao Lu, Fang Ren, Xiubo Liu, Xianmai Chen, Hongqin Liang, Qian Xiao, Xiaoping Wu, Yufei Yuan, Kai Yuan, Pengling Wang, Fei Yan, Ding Luo, Vincent Gong, Yihong Wang, Xinwei Ma, Qinglin Li, ...

People come and go in one's life. Sometimes, they left for very unfortunate reasons. I cherish my memories with my grandfather and my sister. If they were here with me today, I know they would be smiling and happy for me. I will miss them forever.

人生来去匆匆，偶有不幸。我会珍惜与爷爷和姐姐相处的记忆。如果他们还在世，一定会为我感到开心幸福。我会永远想念他们。

My parents gave me a carefree childhood and study life. You are always emotionally and financially supportive of my choices in life. I love you and thank you with all my heart!

我的父母给予了我无忧无虑的童年和学习生活。你们始终在情感和经济上支持我的人生选择。我爱你们，并且衷心的感谢你们！

My wife Yongqiu Zhu, the love of my life. It gives me tremendous strength knowing that no matter what happens in my life, I can always come home to you for comfort. We have been through thick and thin together over the past 11 years. I shall hold you in my hands for decades to come.

Hongrui Wang
November 2019
Delft, The Netherlands

Curriculum Vitæ

Hongrui WANG

11-06-1990

Born in Ya'an, China.

Education

Sep. 2008–Jun. 2012

Bachelor in Electrical Engineering
Southwest Jiaotong University

Sep. 2012–Aug. 2015

Master student in Electrical Engineering
Southwest Jiaotong University

Sep. 2015–Aug. 2016

Visiting researcher in Railway Engineering
Delft University of Technology

Aug. 2016–Aug. 2019

PhD student in Railway Engineering
Delft University of Technology

Employment

Aug. 2019–present

Postdoctoral researcher in Railway Engineering
Delft University of Technology

List of Publications

Dissertation related publications

Journal articles

4. **H. Wang**, A. Núñez, Z. Liu, D. Zhang, R. Dollevoet, *A Bayesian Network Approach for Condition Monitoring of High-Speed Railway Catenaries*, *IEEE Transactions on Intelligent Transportation Systems*, Online (2019).
3. **H. Wang**, Z. Liu, A. Núñez, R. Dollevoet, *Entropy-based local irregularity detection for high-speed railway catenaries with frequent inspections*, *IEEE Transactions on Instrumentation and Measurement* **68**, 3536 (2019).
2. **H. Wang**, A. Núñez, Z. Liu, Y. Song, F. Duan, R. Dollevoet, *Analysis of the evolution of contact wire wear irregularity in railway catenary based on historical data*, *Vehicle System Dynamics* **56**, 1207 (2018).
1. Z. Liu, **H. Wang**, R. Dollevoet, Y. Song, A. Núñez, J. Zhang, *Ensemble EMD-Based automatic extraction of the catenary structure wavelength from the pantograph-catenary contact force*, *IEEE Transactions on Instrumentation and Measurement* **65**, 2272 (2016).

Conference articles

2. **H. Wang**, Z. Liu, A. Núñez, R. Dollevoet, *Identification of the Catenary Structure Wavelength using Pantograph Head Acceleration Measurements*, *2017 IEEE International Instrumentation and Measurement Technology Conference* (2017).
1. **H. Wang**, A. Núñez, R. Dollevoet, Z. Liu, J. Chen, *Intelligent condition monitoring of railway catenary systems: a Bayesian network approach*, *Dynamics of Vehicles on Roads and Tracks Vol 2: Proceedings of the 25th International Symposium on Dynamics of Vehicles on Roads and Tracks* (2017).

Other publications

Journal articles

15. A. Núñez, A. Jamshidi, **H. Wang**, *Pareto-based maintenance decisions for regional railways with uncertain weld conditions using the Hilbert spectrum of axle box acceleration*, *IEEE Transactions on Industrial Informatics* **15**, 1496 (2019).
14. Z. Liu, Y. Song, Y. Han, **H. Wang**, J. Zhang, Z. Han, *Advances of research on high-speed railway catenary*, *Journal of Modern Transportation* **26**, 1 (2018).
13. J. Chen, Z. Liu, **H. Wang**, A. Núñez, Z. Han, *Automatic defect detection of fasteners on the catenary support device using deep convolutional neural network*, *IEEE Transactions on Instrumentation and Measurement* **67**, 257 (2018).

12. Y. Song, Z. Liu, **H. Wang**, J. Zhang, X. Lu, F. Duan, *Analysis of the galloping behaviour of an electrified railway overhead contact line using the non-linear finite element method*, *Proceedings of the Institution of Mechanical Engineers, Part F: Journal of Rail and Rapid Transit* **232**, 2339 (2018).
11. X. Lu, Z. Liu, J. Zhang, **H. Wang**, Y. Song, F. Duan, *Prior information-based finite frequency H_∞ control for active double-pantograph in high-speed railway*, *IEEE Transactions on Vehicular Technology* **66**, 8723 (2017).
10. X. Lu, Z. Liu, Y. Song, **H. Wang**, J. Zhang, Y. Wang, *Estimator-based multi-objective robust control strategy for an active pantograph in high-speed railway*, *Proceedings of the Institution of Mechanical Engineers, Part F: Journal of Rail and Rapid Transit* **232**, 1064 (2017).
9. Y. Song, Z. Liu, H. Ouyang, **H. Wang**, J. Zhang, *Sliding mode control with PD sliding surface for high-speed railway pantograph-catenary contact force under strong stochastic wind field*, *Shock and Vibration, Online* (2017).
8. Y. Song, H. Ouyang, Z. Liu, G. Mei, **H. Wang**, X. Lu, *Active control of contact force for high-speed railway pantograph-catenary based on multi-body pantograph model*, *Mechanism and Machine Theory* **115**, 35 (2017).
7. Y. Song, Z. Liu, F. Duan, X. Lu, **H. Wang**, J. Zhang, *Study on wind-induced vibration behaviour of railway catenary in spatial stochastic wind field based on nonlinear finite element procedure*, *Journal of Vibration and Acoustics-Transactions of The ASME* **140** (2017).
6. K. Huang, Z. Liu, F. Zhu, Y. Cheng, **H. Wang**, Z. Zheng, Y. Wang, *A systematic EMTP impedance modeling scheme aiming at train body in high-speed railway*, *IEEE Transactions on Transportation Electrification* **3**, 272 (2017).
5. **H. Wang**, Z. Liu, Y. Song, X. Lu, Z. Han, J. Zhang, Y. Wang, *Detection of contact wire irregularities using a quadratic time-frequency representation of the pantograph-catenary contact force*, *IEEE Transactions on Instrumentation and Measurement* **65**, 1385 (2016).
4. Y. Wang, Z. Liu, X. Mu, K. Huang, **H. Wang**, S. Gao, *An Extended Habedank' s Equation-Based EMTP Model of Pantograph Arcing Considering Pantograph-Catenary Interactions and Train Speeds*, *IEEE Transactions on Power Delivery* **31**, 1186 (2016).
3. **H. Wang**, Z. Liu, Y. Song, X. Lu, *Ensemble EMD-based signal denoising using modified interval thresholding*, *IET Signal Processing* **11**, 452 (2016).
2. Y. Song, Z. Liu, **H. Wang**, X. Lu, J. Zhang, *Nonlinear analysis of wind-induced vibration of high-speed railway catenary and its influence on pantograph-catenary current collection*, *Vehicle System Dynamics* **54**, 723 (2016).
1. Y. Song, Z. Liu, **H. Wang**, X. Lu, J. Zhang, *Nonlinear modelling of high-speed catenary based on analytical expressions of cable and truss elements*, *Vehicle System Dynamics* **53**, 1455 (2015).

Conference articles

5. W. Liu, Z. Liu, A. Núñez, L. Wang, K. Liu, Y. Lyu, **H. Wang**, *Multi-Objective Performance Evaluation of the Detection of Catenary Support Components Using DCNNs*, [15th IFAC Symposium on Control in Transportation Systems \(2018\)](#).
4. A. Núñez, A. Jamshidi, **H. Wang**, J. Hendriks, I. Ramirez, J. Moraal, R. Dollevoet and Z. Li, *A condition-based maintenance methodology for rails in regional railway networks using evolutionary multiobjective optimization: Case study line Braşov to Zărneşti in Romania*, [2018 IEEE Congress on Evolutionary Computation \(2018\)](#).
3. J. Chen, Z. Liu, **H. Wang**, K. Liu, *High-speed railway catenary components detection using the cascaded convolutional neural networks*, [2017 IEEE International Conference on Imaging Systems and Techniques \(2017\)](#).
2. Y. Song, Z. Liu, **H. Wang**, X. Lu, F. Duan, *Numerical simulation for the vertical vehicle-track-pantograph-catenary coupled system*, [The Third International Conference on Railway Technology: Research, Development and Maintenance \(2016\)](#).
1. X. Lu, Z. Liu, Y. Wang, **H. Wang**, F. Duan, *Robust state estimation for double pantographs with random missing measurements in high-speed railway*, [2016 IEEE International Power Electronics and Motion Control Conference \(2016\)](#).